



UPPSALA
UNIVERSITET

*Digital Comprehensive Summaries of Uppsala Dissertations
from the Faculty of Science and Technology 1759*

Accumulative Charge Separation in Photocatalysis

From Molecules to Nanoparticles

MARIIA PAVLIUK



ACTA
UNIVERSITATIS
UPSALIENSIS
UPPSALA
2019

ISSN 1651-6214
ISBN 978-91-513-0543-1
urn:nbn:se:uu:diva-369930

Dissertation presented at Uppsala University to be publicly examined in Högssalen, Ångströmlaboratoriet, Lägerhyddsvägen 1, Uppsala, Friday, 22 February 2019 at 10:15 for the degree of Doctor of Philosophy. The examination will be conducted in English. Faculty examiner: Professor Gary Brudvig (Yale University).

Abstract

Pavliuk, M. 2019. Accumulative Charge Separation in Photocatalysis: From Molecules to Nanoparticles. *Digital Comprehensive Summaries of Uppsala Dissertations from the Faculty of Science and Technology* 1759. 88 pp. Uppsala: Acta Universitatis Upsaliensis. ISBN 978-91-513-0543-1.

Photochemical energy conversion into solar fuel involves steps of light absorption, charge separation and catalysis. Nature has taught us that the effective accumulation of redox equivalents and charge separation are the key steps in sunlight conversion. The focus of this thesis is to unveil photophysical and photochemical processes that lead to accumulative charge separation. The optimization of electron transfer process will be held by minimization of losses via recombination, and extension of the lifetime of the charge separated state by usage of the electron relay.

The goal is to couple light induced electron transfer process with the multi-electron catalytic process of hydrogen evolution. In this regard, light harvesters (molecules, metal nanostructures) that generate at least two electrons per absorbed photon will be studied. Additionally, semiconductors that generate long-lived charge separated states are utilized to accumulate several redox equivalents necessary for hydrogen evolution.

The hybrid systems produced by the combination of the advantageous properties of molecules, semiconductors, and metal nanoparticles are under the scope of investigation. Metal nanoparticles are advantageous because of their high absorption cross-section. The molecular linkers provide control and flexibility in tuning the connection between the light absorber and the electron relay. Semiconductor nanoparticles offer the desired charge separation properties via prolonging the lifetime sufficiently to perform photocatalysis.

The detailed understanding, investigation and development of the hybrid systems is at the heart of the progress of photochemical solar fuel production.

Keywords: Accumulative charge separation, Electron transfer, Plasmon dynamics, Time-resolved spectroscopy, Photocatalysis.

Mariia Pavliuk, Department of Chemistry - Ångström, Physical Chemistry, Box 523, Uppsala University, SE-75120 Uppsala, Sweden.

© Mariia Pavliuk 2019

ISSN 1651-6214

ISBN 978-91-513-0543-1

urn:nbn:se:uu:diva-369930 (<http://urn.kb.se/resolve?urn=urn:nbn:se:uu:diva-369930>)

This thesis is dedicated to my family

List of Papers

This thesis is based on the following papers, which are referred to in the text by their Roman numerals.

- I **Ultra Long-lived Electron-Hole Separation within Water-Soluble Colloidal ZnO Nanocrystals: Prospective Applications for Solar Energy Production**
Cieślak, A. M.,[#] Pavliuk, M. V.,[#] D'Amario, L.,[#] Abdellah, M.,[#] Sokołowski, K.; Rybinska, U.; Fernandes, D. L. A.; Leszczyński, M.K.; Mamedov, F.; El-Zohry, A.M.; Föhlinger, J.; Budinská, A.; Wolska-Pietkiewicz, M.; Hammarström, L.; Lewiński, J.; Sá, J. *Nano Energy* **2016**, *30*, 187–192.
- II **Hydrogen Evolution with Nanoengineered ZnO Interfaces Decorated by a Beetroot Extract and a Hydrogenase Mimic**
Pavliuk, M.V.; Cieślak, A.M.; Abdellah, M.; Budinská, A.; Pulen, S.; Sokołowski, K.; Fernandes, D.L.A.; Bastos, E.L.; Ott, S.; Hammarström, L.; Edvinsson, T.; Lewiński, J.; Sá, J. *Sustainable Energy & Fuels* **2017**, *1*, 69–73.
- III **Magnetic Manipulation of Spontaneous Emission from Inorganic CsPbBr₃ Perovskites Nanocrystals**
Pavliuk, M. V.; Fernandes, D. L. A.; El-Zohry, A. M.; Abdellah, M.; Nedelcu, G.; Kovalenko, M. V.; Sá, J. *Adv. Optical Mater.* **2016**, *4*, 2004–2008.
- IV **Hydrogen Evolution with CsPbBr₃ Perovskite Nanocrystals under Visible Light in Solution**
Pavliuk, M. V.; Abdellah, M.; Sá, J. *Mater. Today Comm.* **2018**, *16*, 90–96.
- V **Nano-Hybrid Plasmonic Photocatalyst for Hydrogen Production at 20% Efficiency**
Pavliuk, M.V.; Fernandes, A.B.; Abdellah, M.; Fernandes, D.L.A.; Machado, C.O.; Rocha, I.; Hattori, Y.; Paun, C.; Bastos, E.L.; Sá, J. *Sci. Rep.* **2017**, *7*, 8670.

VI Hydrated Electron Generation by Excitation of Localized Surface Plasmons in Copper Nanoparticles

Pavliuk, M. V.,[#] Gutiérrez Álvarez, S.,[#] Hattori, Y.; Messing, M. E.; Czapla-Masztafiak, J.; Szlachetko, J.; Silva, J. L.; Moyses Araujo, C.; Fernandes, D. L. A.; Lu, L.; Kiely, C. J.; Abdellah, M.; Nordlander, P.; Sa, J.

Manuscript submitted

The authors contributed equally

Reprints were made with permission from the respective publishers.

Papers not Included in this Thesis

During my PhD studies, I also contributed to the following papers:

- VII Photoinduced hole transfer from tris(bipyridine)ruthenium dye to a high-valent iron-based water oxidation catalyst**
Shylin, S. I.; Pavliuk, M. V.; D'Amario, L.; Fritsky, I. O.; Berggren, G. *Faraday Discuss.* **2019**, Doi: 10.1039/c8fd00167g.
- VIII Light-Induced Ultrafast Proton-Coupled Electron Transfer Responsible for H₂ Evolution on Silver Plasmonics**
Hattori, Y.; Abdellah, M.; Rocha, I.; Pavliuk, M. V.; Fernandes, D. L. A.; Sá, J.
Mater. Today **2018**, *21*, 590–593.
- IX Efficient Visible Light-Driven Water Oxidation Catalysed by an Iron(IV) Clathrochelate Complex**
Shylin, S. I.; Pavliuk, M. V.; D'Amario, L.; Mamedov, F.; Sá, J.; Berggren, G.; Fritsky, I. O. *Submitted*.
- X N-TiO₂/Cu-TiO₂ Double-Layer Films: Impact of Stacking Order on Photocatalytic Properties**
Garlisi, C.; Szlachetko, J.; Aubry, C.; Fernandes, D.L.A.; Hattori, Y.; Paun, C.; Pavliuk, M. V.; Rajput, N. S.; Lewine, E.; Sá, J.; Palmisano, G.
J. Catal. **2017**, *353*, 116–122.
- XI Controlling Dark Catalysis with Terahertz Light**
Sá, J.; Fernandes, D. L. A.; Pavliuk, M. V.; Szlachetko, J.
Catal. Sci. Technol. **2017**, *7*, 1050–1054.
- XII Direct Determination of Metal Complexes' Interaction with DNA by Atomic Telemetry and Multiscale Molecular Dynamics**
Czapla-Masztafiak, J.; Nogueira, J. J.; Lipiec, E.; Kwiatek, W. M.; Wood, B. R.; Deacon, G. B.; Kayser, Y.; Fernandes, D. L.A.; Pavliuk, M. V.; Szlachetko, J.; González, L.; Sá, J.
J. Phys. Chem. Lett. **2017**, *8*, 805–811.

XIII Novel Photo-Reactor for Fast Screening of Photo-Catalytic Systems

Fernandes, D. L. A.; Budinská, A.; Pavliuk, M. V.; Sá, J.
J. Photoch. Photobio. A **2017**, 36–39.

XIV Conceptual Design of a Nanoleaf for Artificial Photosynthesis

Pavliuk, M. V.; Hattori, Y.; Sá, J.
Interdiscip. J. Chem. **2016**, 1, 47–51.

XV Homogeneous Cobalt/Vanadium Complexes as Precursors for Functionalized Mixed Oxides in Visible-Light-Driven Water Oxidation

Pavliuk, M. V.; Mijangos, E.; Makhankova, V. G.; Kokozay, V. N.; Pullen, S.; Liu, J.; Zhu, J.; Styring, S.; Thapper, A.
ChemSusChem **2016**, 9, 2957–2966.

XVI Green Microfluidic Synthesis of Monodisperse Silver Nanoparticles: Via Genetic Algorithm Optimization

Fernandes, D. L. A.; Paun, C.; Pavliuk, M. V.; Fernandes, A. B.; Bastos, E. L.; Sá, J.
RSC Adv. **2016**, 6, 95693–95697.

XVII Structural Transformation of $\text{Bi}_{1-x/3}\text{V}_{1-x}\text{Mo}_x\text{O}_4$ Solid Solutions for Light-Driven Water Oxidation

Terebilenko, K. V.; Bychkov, K. L.; Baumer, V. N.; Slobodyanik, N. S.; Pavliuk, M. V.; Thapper, A.; Tokmenko, I. I.; Nasieka, I. M.; Strelchuk, V. V.
Dalton Trans. **2016**, 45, 3895–3904.

XVIII Soret Fluorescence Involved in Caryophyllales Plants Ultraviolet Protection

Sá, J.; Pavliuk, M. V.; El-Zohry, A.M.; Fernandes, D. L. A.; Föhlinger, J.; Mukhtar, E. *Sci. Lett. J.* **2016**, 5, 226.

XIX Structural, Magnetic, Thermal and Visible Light-Driven Water Oxidation Studies of Heterometallic Mn/V Complexes

Pavliuk, M. V.; Makhankova, V. G.; Kokozay, V. N.; Omelchenko, I. V.; Jezierska, J.; Thapper, A.; Styring, S.
Polyhedron **2015**, 88, 81–89.

XX A 3D Printed Microliquid Jet with an Adjustable Nozzle Diameter

Fernandes, D. L. A.; Pavliuk, M. V.; Sá, J.
Analyst **2015**, 140, 6234–6238.

Contribution to Papers

My contributions to the papers included in this thesis are as follows:

- I I carried out the spectroscopic characterization of the materials (both steady state and time-resolved studies), contributed to the data analysis and their interpretation, wrote part of the manuscript and prepared figures.
- II I performed photocatalytic studies, contributed to time-resolved spectroscopy studies, data analysis and interpretation, wrote the draft of the manuscript and prepared figures.
- III Performed time-resolved photoluminescence studies, the data analysis and their interpretation, and contributed to writing the manuscript.
- IV Conducted photocatalysis experiments, participated in transient absorption infrared spectroscopy measurements, performed data analysis and interpretation of the results.
- V Design and performance of the experiments, namely photocatalysis, time-resolved absorption spectroscopy studies. I have carried out data analysis and contributed to the discussion of experimental data.
- VI All experimental work was conducted together with a co-supervised master student (except electron microscopy measurements). I actively participated in discussion and data analysis.

Abbreviations

Ag-PVP	Ag nanoparticles decorated with polyvinylpyrrolidone
β -Ala	β -alanine
B	Betanin
B _c	Betanin commercial
B _p	Betanin purified
CB	Conduction band
CW	Continuous wave
DSSC	Dye-sensitized solar cell
FeFe _{cat}	[FeFe(mcbdt)(CO) ₆], mcbdt – 3-carboxybenzene-1,2-dithiolate
FTIR	Fourier transform infrared
GSB	Ground state bleach
HER	Hydrogen evolution reaction
HET	Hot electron transfer
HR-XAS	High-resolution X-Ray absorption spectroscopy
HOMO	Highest occupied molecular orbital
IA	Induced absorption
IRF	Instrument response function
LSPR	Localized surface plasmon resonance
LUMO	Lowest occupied molecular orbital
MV	Methyl viologen dichloride hydrate
NCs	Nanocrystals
OEG-H	2,5,8,11-tetraoxatetradecan-14-oic acid (MeO-EG ₃ -COOH)
p-ABA	<i>p</i> -aminobenzoic acid
PL	Photoluminescence
PRET	Plasmon resonance-energy transfer
RXES	Resonant X-Ray emission spectroscopy
QMS	Quadrupole mass-spectrometer
QY	Quantum yield
SE	Stimulated emission
TAS	Transient absorption spectroscopy
TEA	Triethanolamine
TEM	Transmission electron microscopy
TFA	Trifluoroacetic acid
TIRAS	Transient infrared absorption spectroscopy
TRPL	Time-resolved photoluminescence
VB	Valence band

Contents

1. Introduction.....	15
1.1. Motivation.....	15
1.2. Solar Light Harvesting.....	17
1.3. Importance of Accumulative Charge Separation.....	18
1.4. Architectures for Solar Energy Conversion.....	20
1.5. Aim of this Thesis.....	22
2. Light-Matter Interaction: Fundamentals.....	23
2.1. Molecules.....	23
2.2. Semiconductor Nanoparticles.....	23
2.3. Metal Nanoparticles.....	24
3. Methods.....	27
3.1. Steady-State Spectroscopy.....	27
3.2. Time-Resolved Spectroscopy.....	27
3.2.1 Time-Resolved Absorption.....	28
3.2.2 Time-Resolved Photoluminescence.....	30
3.3. Photocatalysis and Energy Conversion Efficiency.....	31
4. Natural Dye for Solar Energy Conversion.....	33
4.1. Betanin as Promising Photosensitizer.....	33
4.2. Electron Dynamics.....	34
4.3. Summary and Outlook.....	38
5. Towards Ultra Long-Lived Charge Separation with Semiconductors.....	39
5.1. Aim of the Study.....	39
5.2. ZnO Nanocrystals as Electron Relay (Papers I-II).....	40
5.2.1. Sample Characterization.....	40
5.2.2. Time-Resolved Spectroscopy Studies.....	42
5.2.3. Photocatalysis.....	46
5.2.4. Summary and Outlook.....	46
5.3. CsPbBr ₃ Nanocrystals as Light Harvester (Papers III-IV).....	47
5.3.1. Sample Characterization.....	47
5.3.2. Photocatalysis.....	48
5.3.3. Magneto-Photoluminescence Studies.....	49
5.3.4. Summary and Outlook.....	53

6. Light Trapping with Plasmonic Nanoparticles	54
6.1. Aim of the Study.....	54
6.2. Ag Nanoparticles (Paper V)	54
6.2.1. Sample Characterization	56
6.2.2. Electron Dynamics Studies	57
6.2.3. Photocatalysis	59
6.2.4. Summary and Outlook	60
6.3. Cu Nanoparticles (Paper VI)	60
6.3.1. Sample Preparation and Characterization	60
6.3.2. Plasmon Dynamics.....	61
6.3.3. Electron dynamics.....	63
6.3.4. Photocatalysis	65
6.3.5. Summary and Outlook	66
7. Conclusions	67
8. Populärvetenskaplig Sammanfattning (Summary in Swedish).....	70
9. Анотація (Summary in Ukrainian).....	73
10. Acknowledgements.....	75
References.....	78

1. Introduction

1.1. Motivation

Growing consumption and dependence of fossil fuels has influenced our day-to-day lives, the environment, the economy, and has shaken the foundation of peace around the world. Strong interconnection between these areas has become a main trigger towards the search for renewable energy resources. Five key questions arise when moving towards a solution in this regard: why, how, who, when, and what to do?

1) Why? Energy is a vital component of our everyday life. The world's demand for energy will keep growing, providing a strong motivation for research into the development of environmentally clean, alternative energy resources.¹ To sustain the life of 7.2 billion people, we need ~ 18 terawatts (TW) of power. While by 2050, due to the rise in global population and the appearance of new consumers, the energy consumption will need an extra 10 TW of energy.² About 50 % of the global oil reserve has been already consumed, and search for new oil resources as well as new methods for their extraction will not change the amount of oil existing on the planet.³ Before we are put in a deadlock due to the exhaustion of fossil resources, it is worth searching sustainable and affordable (cost-effective) long-term solutions.

The second industrial revolution introduced another blameworthy player, namely greenhouse gas emission due to the burning of carbon based fossil fuels. For more than 800,000 years until 1950, the atmospheric carbon dioxide level had never exceeded 300 ppm. While within the last seventy years, it has increased by 30%, from ~ 300 ppm to ~ 400 ppm,⁴ causing the rise of the global mean surface temperature.⁵ In 2015, 195 countries agreed to cap the overall rise of a maximum global temperature to 2°C compared to the preindustrial levels.⁶ The abrupt changes in temperature and atmospheric pollution in biosphere may have dramatic effects for us.

2) How? The growing energy demand and climate change are major challenges. The solution can be found via (1) the manufacturing of additional nuclear power plants, (2) the development of carbon-neutral technologies, where all CO_2 produced will be trapped,⁷ or (3) usage of renewable energy sources. For gaining 10 TW energy from nuclear power, one will need to construct a 1 GW nuclear power plant every day for at least 5 decades. Since the first nuclear power plant was built in 1954, two major catastrophes con-

cerning nuclear plants occurred in Chernobyl and in Fukushima. If we estimate the probability of a reoccurrence of such an event, in the future, the option of building more nuclear power plants is non-starter. On the other hand, carbon-neutral technologies that are focused on usage of fossil fuels without negative impact on the environment will require secure trapping of gigantic quantities of greenhouse gases and their effective conversion. Thus, the priority is given to renewable energy resources – hydroelectric power, (0.5 TW), wind power (2–4 TW), wave power (2 TW), geothermal power (12 TW) and solar power (120,000 TW) that constantly reach the earth. Among these alternatives, solar power is able to provide sufficient energy to satisfy global needs for a year within one hour.

3) Who? The characteristic feature of the *solar energy* is its wide distribution and abundance. While fossil fuels are mainly locally concentrated, sunlight is a dispersed source of energy. The intermission, dependence on time of the day, geographic location, etc. demands for more effective initiatives for the sunlight harnessing. Instead of the resources being geologically owned by a few hands, e.g. the few corporate entities that control the oil production and distribution, solar power can be harvested and utilized by individuals (Figure 1).



Figure 1. Idea of shared thinking.

Without the ownership of the resource, sharing the energy produced is a stronger likelihood. The “shared thinking” becomes more popular nowadays, and can be found in knowledge sharing (e.g. Wikipedia), book sharing, car sharing, etc. often widely available and free of charge. This is in contrast to the previous century, where power could be described as a pyramid. For Millennials, power is seen within the network of people you have. Instead of being an autonomous unit, a trend from the 1950s, nowadays we would win more by cooperating for the global benefit (the beginning of a third industrial revolution).⁸ Thus, the new energy system needs to be highly distributed and less centralized; renewable energy meets this requirement. That is one of the prerequisites for achieving the Sustainable Society.

4) When? Within the last decade, solar energy conversion to electric power has expanded notably. From being an insignificant electricity distrib-

utor, it has grown up to 2.1 % worldwide and 4 % within Europe in contribution to the electric power.⁹ In 2017, the total installed capacity of photovoltaic reached 400 GW_{peak}. Regional analysis revealed that the fraction of electricity via photovoltaics reached 7 % in Italy, Germany and Greece, but only 0.2 % in Sweden.¹⁰ The direct investment and subsidies to the renewable energy sector enabled its development and proliferation, hence causing a reduction in the production costs and an increase in price-competitiveness in the photovoltaic technology. The foundation has already been laid, and time is ticking; we just need to know what to do?

5) What to do? At present, the energy consumption is mainly based on electricity (one fifth) and fuels (four fifths). In contrast to high efficiency of electrical consumption (e.g. in motors), fuels offer high capacity to long-term storage of energy. Additionally, fuels offer the possibility of production of valuable goods, e.g. plastic and rubber items, synthetic fibers, clothes, anti-septics, fertilizers, etc. We should consider that materials used for generation of renewable energy need to be manufactured from low-cost and “endless” available resources.¹¹ In the long term it is beneficial to invest efforts in both these directions – photovoltaics and solar fuel production.

1.2. Solar Light Harvesting

Harvesting of solar light and subsequent conversion into electrical or chemical forms of energy can be performed by various strategies.¹² I will briefly summarize a few appealing strategies of solar energy conversion.

Utilization of sunlight to produce electricity can be done with photovoltaics that operate on the working principle of a *p-n* junction. Currently, there are four generations of photovoltaic devices. The weak side of the first generation of photovoltaic devices, thick crystalline films (single junction cells) was the high costs of their fabrication and installation. The second generation – the thin films solar cells¹³ – could have facilitated lower prices, while still suffered from efficiency limitations.¹⁴ The third and fourth generation devices (dye-sensitized solar cells,¹⁵ organic solar cells,¹⁶ and multi-junction solar cells,¹⁷ quantum dot solar cells,¹⁸ perovskite solar cells,¹⁹ plasmonic solar cells²⁰) showed the potential to overcome the Shockley–Queisser limit, thus offering higher efficiencies at lower cost.²¹

The second approach includes the direct conversion of sunlight into chemical fuel, so-called solar fuel. It is more convenient to convert energy in the form of a chemical fuel as it offers high storage capacities.²² The key steps of photochemical conversion include light absorption, charge separation and catalysis for conversion of the substrate into the valuable chemicals. Appealing and plentiful substrates that can be transformed into fuel are, for example water and carbon dioxide. Photochemical water splitting can be divided into two half reactions of hydrogen evolution and oxygen evolution. Electronic

structure alignment of materials utilized for water splitting plays a crucial role. Notably, for the two electron, two proton process, namely the hydrogen evolution reaction (HER), the used materials must be able to provide a more negative potential than 0 V vs NHE (normal hydrogen electrode) at pH = 0. While for the four electron four proton process, namely the oxygen evolution reaction, the provided potential must be more positive than 1.23 V vs NHE at pH = 0.

1.3. Importance of Accumulative Charge Separation

Nature has evolved a way for solar energy conversion via photosynthesis by transforming water and carbon dioxide to oxygen and carbohydrates. Light excitation of chlorophyll molecules ($^*P_{680}$) in Photosystem II induce charge separation via an electron transport chain.²³ The energy of electrons that pass through the electron transport chain is used to pump protons from the stroma to the thylakoid membrane. The concentration gradient that is created is used to power ATP synthase. The oxidative holes are then used for the generation of oxygen with the help of the Mn_4O_5Ca cluster, while low potential electrons are driven towards Photosystem I, where they are reenergized and further used to reduce $NADP^+$ to NADPH. Then NADPH and ATP are used for CO_2 fixation to produce sugars in the Calvin cycle.

The efficacy of electron transport in natural photosynthesis systems lies in the rapid shuttling of electrons from the central chlorophyll by the intermediate acceptors and donors. Thus, for effective photochemical water splitting it is essential to efficiently transport photogenerated charge carriers (e^- and h^+) to the desired destination.²⁴

Previously established donor|photosensitizer|acceptor (D|P|A) systems have been designed for charge separation that are based on single electron events.²⁵⁻²⁶ Use of such D|P|A systems will be problematic when multiple redox equivalents are needed, such as in catalysis. In order to close the catalytic cycle, multiple charge carriers need to be accumulated with sequential single photon absorption processes for straightforward solar fuel generation – further denoted as accumulative charge separation.²⁷

It may be possible to achieve accumulative charge separation by modifying the components of well-established D|P|A systems:

1. *Photosensitizer.* Usage of stable light absorbers (with a long excited state lifetime as well as a large extinction coefficient) capable of directly/sequentially generating more than one electron per photon absorbed is a key goal. (a) In case of molecular light harvesters that could transfer two electrons, preferences are given to the molecules, where the potential for the second oxidation or reduction step is not that different from that of the first step; this will minimize energy losses. For instance, this can be achieved by coupling proton transfer to electron transfer steps. (b) With semiconductors as

light absorbers, one needs to focus on increasing the range of wavelengths absorbed in the visible part of the solar spectrum and have favorable band gap energies for the catalytic reaction. (c) Metal nanoparticles (NPs) are able to directly generate multiple charge carriers upon photon absorption by the interband excitation and plasmon resonance of nanostructures.²⁸ In ref. 28 multielectron generation has been quantitatively estimated in the presence of hole scavengers under various excitation conditions, where laser power and excitation wavelength were tuned.

2. *Donor, acceptor.* In some cases, to prolong the lifetime of short-lived charges from the photosensitizer one will need to add an electron relay that will be utilized for the charge storage of the redox equivalents required for the further photocatalytic process. Various compounds and semiconductors can be used for electron relays. For more efficient electron transfer to the semiconductor the following properties are desirable: (a) high surface area for enhanced loading of the sensitizer; (b) favorable conduction band (CB) and valence band (VB) edges for the desired reaction; (c) high electron mobility;²⁹ (d) inert activity towards reaction medium; (e) low toxicity and high abundance.

Combination of the above stated guidelines could further promote accumulative charge separation, if one takes into account the following aspects:

1. *Kinetics of the redox processes.* The rate of the charge recombination must be suppressed, to allow accumulated charges be utilized in the catalytic reaction.³⁰⁻³² (a) For molecular systems, the redox potentials of components (e.g. donor, bridge/photosensitizer, acceptor) must be chosen with great care to ensure the flow of electrons proceeds in the desired direction, while minimizing the rate of undesired recombination processes. For example, one must ensure that newly formed products of charge separation will not interact with each other so that they promote reverse reactions. (b) For semiconductors and metal NPs, charge recombination can be suppressed by a guided control of morphology, crystallinity, size, origin of precursors and synthetic methods.

2. *Chemical binding within light harvesting D|P|A system.* Here, the challenge is to create a linked D|P|A system, where linking promotes forward charge transfer only in one way towards catalysts, while limiting the back electron transfer. Very often, the length of the linker and its charge transfer functions will play a crucial role. Linking of all components can be applied in several ways. First, one can synthesize interconnected systems; however, such a strategy can involve intense synthetic work and generally lead to low yields. Second, components, like sensitizer|catalyst can be coadsorbed on the surface of a semiconductor.³³ In this case, one assumes that coadsorbed components have functional groups to promote both efficient charge transfer and prevent desorption, functioning under the conditions suitable for photocatalysis.³⁴⁻³⁵ Finally, a linker with bifunctional groups can be added to interconnect the system components, where these components must have available surface area to allow linking.

Solar fuel devices should be capable of converting sunlight into fuel directly, without the necessity of an intermediate component, e.g. a photovoltaic. Where the development of a complete solar fuel device is desired, it is acceptable to compartmentalize or deconstruct the system for a deeper understanding of how to further improve and develop the system. Moreover, it eliminates the necessity of the separation of the formed products, where oxygen may act as an unwanted electron acceptor.

This thesis focuses primarily on hydrogen evolution, while progress on water oxidation is discussed in papers VII,³⁶ XV³⁷ and XIX,³⁸ which are not included in this thesis. Key aspects and strategies applied towards accumulative charge separation will be discussed in more detail (*vide infra*).

1.4. Architectures for Solar Energy Conversion

Three means of harvesting solar light energy towards the production of solar fuel, e.g. hydrogen, will be presented: (1) Molecular assembly model; (2) Photocatalysis facilitated with semiconductor nanostructures towards hydrogen production; and (3) Plasmonic nanostructures for solar fuel production. Recent developments and limitations within above-mentioned strategies will be highlighted.

1. Molecular assembly model. Molecular assemblies are mainly composed of components that function as antenna, electron donor and electron acceptor.³⁹⁻⁴⁰ These components can be both connected or remain unconnected, *i.e.* covalent or non-covalent. Methyl viologen (MV^{2+}) is a known two-electron acceptor, which is capable of generating a long-lived charge separated state in pair with $[Ru(bpy)_3]^{2+}$ as photosensitizer. A close proximity between the MV^{2+} and the sensitizer, via covalent bonding, results in enhancement of undesired back-electron transfer, thus precluding utilization of this dyad for the generation of solar fuels.⁴¹ In contrast, covalent linking of $[Ru(bpy)_3]^{2+}$ and MV^{2+} via a carbon chain has promoted generation of a long-lived charge separated states.⁴² Photosensitizer-cobaloxime assemblies with covalent bonding via a bridge, also resulted in higher turnover yields,⁴³⁻⁴⁵ with some exceptions,⁴⁶ suggesting the key role of (a) proper linker that was applied, (b) the kinetics of electron transfer,⁴⁷ (c) redox properties of its components. Light induced generation of double reduced acceptor (PDI^{2-}) was the first evidence of accumulative electron transfer.⁴⁸ There were many examples of the accumulation of either electrons⁴⁹⁻⁵⁰ or holes,⁵¹ while no examples for accumulation of both of them within the same molecular assembly. The weak stability of such linked dyads and triads predominantly caused their fast decomposition and low activity in HER in the presence of sacrificial electron donor.⁵² Obstacles that precluded utilization of molecular assembly systems towards accumulative charge separation are clarified in ref 53, 54.

2. *Photocatalysis facilitated with semiconductor nanostructures.* Many semiconductors (oxides, nitrides, chalcogenides, etc.)⁵⁵ with suitable CB edge positions have been extensively studied for H₂ evolution, notably TiO₂, ZnO, Nb₂O₅,⁵⁶ PbWO₄,⁵⁷ CdS,² BiVO₄, Cu₂O etc. In 1972, Honda and Fujishima demonstrated for the first time the photolysis of water with TiO₂ semiconductor in electrochemical cell under UV illumination.⁵⁸ Most semiconductors suffered from low absorption of the visible light. To promote visible light absorption, Z-scheme photocatalytic systems inspired by natural photosynthesis were developed.⁵⁹ In case of TiO₂, the red shifting of the band gaps edges was achieved by co-doping, with both metal and non-metal impurities.⁶⁰⁻⁶¹ However, co-dopants can generate new problems by acting as electron-hole recombination centers.⁶² Changes in morphology instead, can improve both light harvesting properties, and charge separation inside the material.⁶³ The created disorder within surface layers of TiO₂ has promoted charge separation and localization thus, resulting in increased amounts of photogenerated hydrogen.⁶⁴ Electron mobility within the semiconductor is another factor to be considered, for effective charge separation, notably ZnO offers orders of magnitude higher electron mobility, in comparison with TiO₂.⁶⁵

Utilization of visible light was achieved by sensitization of dyes onto the high surface area semiconductors in the early 1980's by Grätzel and co-workers.⁶⁶ Since then this field has expanded tremendously.⁶⁷⁻⁶⁹ The first example of accumulative charge separation was proven with the help of time-resolved spectroscopy for the hybrid, molecular/semiconductor system (OTA/Ru/TiO₂) analogous to dye-sensitized solar cells (DSSCs), with no need for external sacrificial agents.³¹ The rapid electron injection into the CB of the semiconductor and further slow recombination were considered as the key factors for the generation of the double charge-separated state.^{32, 70}

3. *Solar fuel production with plasmonic nanostructures.* Generation of hot electrons and hot holes in plasmonic nanostructures is performed by the resonant excitation of surface plasmons.⁷¹ The electron dynamics of the photo-generated charges is orders of magnitude faster (100s of fs) than kinetics of photochemical reactions (ms – s), where these charges may be utilized. Thus, the following strategies are usually applied for harvesting solar light energy:

(a) *Bimetallic systems.* There is limited number of purely plasmonic systems for the direct solar fuel production. Majima and co-workers reported two systems for efficient hydrogen evolution performance, namely Pt-modified Au nanorods,⁷² and Pt-Au triangular nanoprisms (Au-TNPs).⁷³ Morphology control of Pt-edged Au-TNPs enabled controlled charge separation towards corners and edges of triangular nanoprisms coated with Pt, where Au had strong electric fields. In contrast, then Au-TNPs were covered with randomly distributed Pt NPs, recombination dominated over forward electron transfer.

(b) *Metal | Adsorbate systems.* Hot electrons that come from metal nanoparticles may accumulatively deposit their energy in the electron accepting orbitals of an adsorbate via a set of forward/backward electron transfer events, thus prolonging the lifetime of photogenerated charges (has been actively used in surface-enhanced Raman spectroscopy).⁷⁴ Theoretical calculations predicted that Au NPs might directly initiate water splitting due to overlap of oscillating electron density of these NPs with the electron-accepting orbitals of water.⁷⁵

(c) *Metal | Semiconductor systems.* Here, harvesting of sunlight is triggered by the injection of hot electrons (with sufficient energy to overcome the Schottky barrier) into the CB of the semiconductor. An autonomous photosynthetic device composed of light harvester (Au nanorods), electron relay (TiO_2), and both H_2 evolution catalyst (Pt) and O_2 evolution catalyst (Co-containing water oxidation catalyst) has been developed by Moskovits and co-workers.⁷⁶ The Z-scheme system (black phosphorous|Au| $\text{La}_2\text{Ti}_2\text{O}_7$) was able to both efficiently separate photogenerated charges and utilize them for hydrogen production.⁷⁷ Furthermore, enhanced electron-hole separation was achieved by the morphology control,⁷⁸ size control,⁷⁹ addition of electron sink layers,⁸⁰ and utilization of intrinsic electronic heterogeneity of semiconductors.⁸¹ Suppression of the charge recombination pathway also enabled accumulation of hot electrons in the semiconductors conduction band.⁸²

1.5. Aim of this Thesis

The focus of this thesis is to unveil photophysical and photochemical processes that lead to accumulative charge separation. The goal is to couple light induced electron transfer process with multi-electron catalytic process of hydrogen evolution. In this regard, light harvesters (molecules, metal nanostructures) capable to direct generation of at least two electrons per absorbed photon were studied. Additionally, semiconductors capable of generating long-lived charge separated states were utilized for accumulation of several redox equivalents necessary for hydrogen evolution.

2. Light-Matter interaction: Fundamentals

2.1. Molecules

Light may interact with matter on an atomic scale, provided the energy of its photons matches the energy level difference between atomic or molecular states (Bohr's basic principle of spectroscopy): $\Delta E (E_2 - E_1) = \hbar\omega$, where ω is the radiation angular frequency. Light with low energy photons (radio, microwave, infrared) can induce excitation into the translational, rotational and vibrational degrees of freedom of the matter, while ultraviolet and visible light can trigger electronic transitions. Under infrared illumination, the transitions between vibrational states will be induced, where for observing infrared spectra a dipole moment additionally needs to change. UV or visible light absorption by a molecule causes an electronic transition, commonly from the highest occupied molecular orbital (HOMO) to the lowest occupied molecular orbital (LUMO). The strength of the corresponding absorption band will be defined by the transition dipole moment.

Relaxation from the excited state in molecules occurs in solution via a set of radiative (fluorescence $S_1 \rightarrow S_0$ and phosphorescence $T_1 \rightarrow S_0$) and/or non-radiative processes (internal conversion, intersystem crossing, thermalization). Before the electronic relaxation processes, the excess vibrational energy is dissipated to the surrounding solvent with relaxation to the lowest vibrational level within S_1 .

Besides absorption, light can be scattered by the matter both elastically and inelastically. Inelastic scattering is the basis for Raman spectroscopy, where a change in polarizability needs to be fulfilled.

2.2. Semiconductor nanoparticles

In the simple approximation according to the band structure theory, semiconductors are composed of bands (closely spaced energy levels that are formed from the combined atomic and molecular orbitals) with a band gap less than 4.5 eV (range not covered by any energy level). Under thermal equilibrium, the probability of finding electrons in the valence band is determined by the Fermi-Dirac distribution:

$$p(E) = \frac{1}{\left(e^{\frac{E-E_F}{kT}} + 1\right)},$$

where E is the specific energy within the VB, k is the Boltzmann constant, T is the temperature, and E_F is the Fermi level (the energy at which there is a 50% probability of finding an electron).

Once the semiconductor material is exposed to light with photons of energy higher than the band gap, light absorption will trigger the generation of excitons. Only some of them will break apart to form electron-hole pair: an electron in the conduction band and a hole in the valence band.

The semiconductors are classified as direct and indirect band gap semiconductors based on how their bands are aligned with respect to the momentum. For the direct band gap semiconductor, the lowest energy state above the band gap and the highest energy state beneath the band gap remain aligned within the energy-momentum space. However, k -vectors are different for the indirect band gap semiconductor. Thus, the direct and indirect band gap semiconductors have different mechanisms of generating the charges after an excitation event.⁸³

Electrons in the conduction band have finite lifetimes, thus the relaxation of the system via recombination with the hole in the valence band will occur via emission of a photon (photoluminescence) and/or non-radiatively. Similarly to the light absorption event, during the radiative recombination the conservation of energy and crystal momentum need to be fulfilled. Thus, the emission of the photon from the band edge is allowed for a direct band gap semiconductor and is forbidden for an indirect band gap semiconductor. Much slower recombination may be observed in indirect band gap semiconductors due to the involvement of the phonon that carries momentum.

2.3. Metal Nanoparticles

Prior the generation of charge carriers, the photons need to be absorbed by the metal NPs, where the probability of the absorption event is proportional to the square of the local electric field inside the metal.²⁰ Light absorption may be further enhanced by exciting the metal nanoparticles at the resonant frequency of the free electron gas (Figure 2a), resulting in the amplification of its localized oscillations, a process also known as localized surface plasmon resonance (LSPR). Under illumination, the excitation of the plasmon induces a displacement of the electron density and redirects the light towards and into the nanoparticle. The dielectric permittivity of the metal will reflect the ability of the metal nanostructures to exhibit LSPRs.

The optical properties, (e.g. absorption/scattering events) of spherical metal NPs can be described through the Mie Theory, which is essentially the solution of Maxwell's equation with specific boundary conditions.

$$\sigma_{scat} = \frac{128\pi^5 a^6}{3\lambda^4} \left(\frac{\epsilon_{metal} - \epsilon_{medium}}{\epsilon_{metal} - 2\epsilon_{medium}} \right)^2,$$

where a – radius of spherical NPs, λ –the wavelength of the incident light, and $\varepsilon_{\text{metal}}$ and $\varepsilon_{\text{medium}}$ – are the dielectric permittivity for the metal and medium.

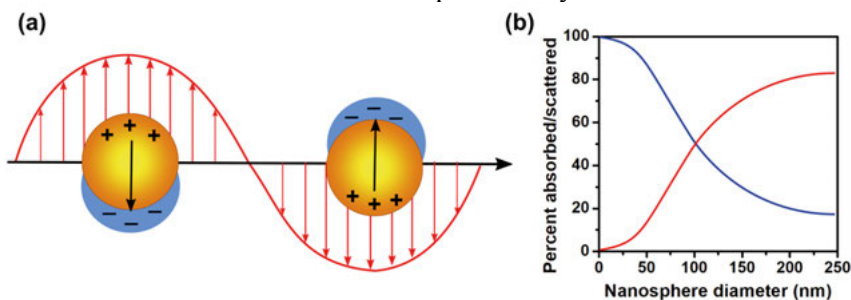


Figure 2. (a) Localized surface plasmon on a metal nanosphere. (b) Dependence of the amount of light that is absorbed (blue line)/scattered (red line) on the particle diameter (reproduced from ref. 69).

There are several key factors that will influence the amount of light absorbed/scattered. The first factor is the size of metal nanoparticles (Figure 2b). For example, Au nanoparticles of 90 nm, have an equal probability between the absorption and scattering event. However, once their size exceeds 90 nm, scattering will dominate over absorption, and vice versa. Second is the shape/geometry of nanoparticles that may enhance the polarizability at the edges/spikes of the nanostructure. The third factor is the composition of the material, where for instance Ag will have higher scattering efficiency than Au due to lower Ohmic losses. The fourth factor is the permittivity of the medium around metal nanoparticle. Tuning the size, shape, composition and medium origin for metal nanostructures enables the utilization of plasmonic nanoparticles via different strategies.

Plasmon resonance is damped radiatively or non-radiatively, where both of these pathways may be utilized in solar devices (Figure 3).

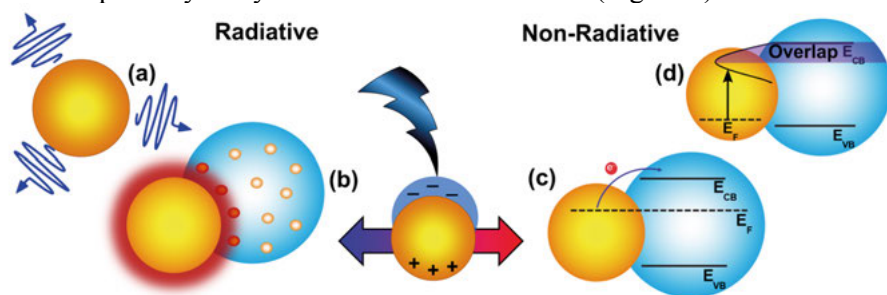


Figure 3. Two paths for the plasmon resonance damping: radiative (a) far-field scattering – scattering of incident light from the metal NP hundreds nanometers away with further reabsorption of this light by sensitizers.⁸⁴⁻⁸⁶ (b) near-field enhancement – focusing of incident light on the metal NP with further enhancement of local electromagnetic fields in close proximity.⁸⁷ Non-Radiative (c) hot-electron transfer (described below). (d) plasmon resonance-energy transfer is similar to Förster resonance energy transfer, where the LSPR dipole is utilized instead of a fluorescent donor molecule.

Hot electron transfer (HET) is a purely quantum mechanical phenomenon, when damping of the plasmon resonance occurs via the generation of hot electron-hole pairs within 1–100 fs. These charge carriers are called hot if their energies are higher than those generated under thermal equilibrium. In contrast to radiative effects of plasmon resonance damping, hot electron transfer allow utilization of photons with energy below the band gap of the semiconductor.

Several theoretical models have been proposed to clarify the mechanism of hot carrier generation. The distribution of the carriers' energies was found to depend on the electronic band structure of metal NPs.⁸⁸⁻⁸⁹ It was shown that some metals (Au, Cu) produce holes with higher (hotter) energies than that for electrons, while others (Ag, Al) generate equally energetically hot electrons and holes.

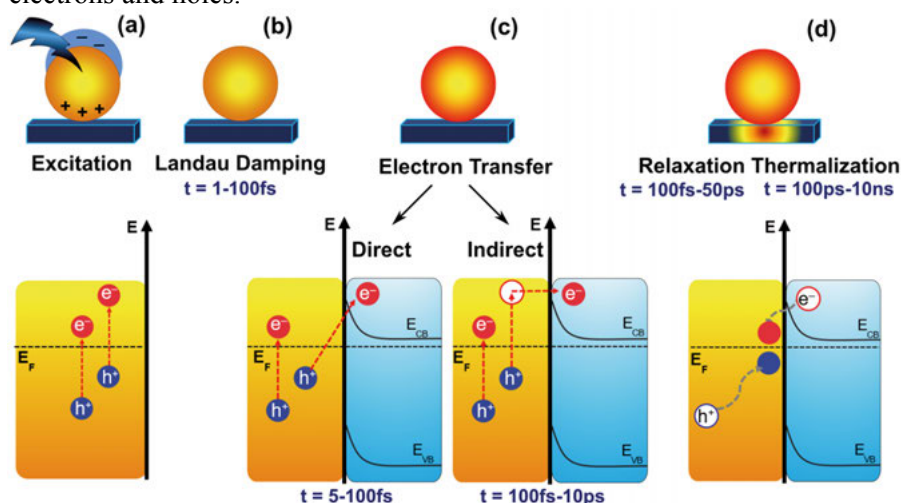


Figure 4. (a) Excitation of LSPR and generation of hot electron and hot holes pairs. (b) Plasmon resonance is damped radiatively / non-radiatively (c) Two mechanism of hot electrons transfer, namely direct and indirect electron transfers. At the interface of metal NP and semiconductor the Schottky barrier is created. (d) Relaxation of hot carriers (electron-electron scattering, electron-phonon scattering, and phonon-phonon scattering), and thermal dissipation to the surrounding.

At the interface of a NP (yellow sphere, Figure 4a) and semiconductor a Schottky barrier will be created, allowing only hot electrons with higher energies than this barrier to be injected into the semiconductor.⁹⁰⁻⁹¹ Electron may be transferred via two mechanisms, namely direct and indirect electron transfer (Figure 4c).⁹²⁻⁹³ The Schottky barrier helps delaying back electron transfer by trapping those electrons that got sufficient energy to be transferred.⁹⁴ Initially hot charge carriers in a non-thermal distribution quickly thermalize obeying Fermi-Dirac distribution via several processes (Figure 4),⁹⁵ namely electron-electron scattering (100 fs–1 ps), followed by electron-phonon scattering (1 ps–5 ps) and phonon-phonon scattering (>50 ps).⁹⁶ The heat is then dissipated to the surrounding (100 ps–10 ns).⁹⁷

3. Methods

This section will present the main governing principles that stand behind the techniques used in the framework of the dissertation. Herein, I will discuss the basics of the performed measurements and calculations.

3.1. Steady-State Spectroscopy

Processes under constant illumination and observations are called steady-state processes. These processes can be regarded as an average of the time-resolved events over the intensity decay of the sample after a single excitation, where our detection tools are often too slow to detect the ultrafast-triggered changes of the sample.⁹⁸ Absorption of light is instantaneous ($\approx 10^{-15}$ s), meaning that during transitions between states, nuclei do not have enough time for significant displacements (Franck-Condon principle). According to Beer-Lambert law, the intensity of electromagnetic radiation that travels through a layer of matter with the thickness (l) and concentration (c) changes from initial (I_0) to a certain transmitted value (I_t) as follows: $I_t = I_0 \cdot e^{-kcl}$. With the help of the spectrophotometer one can determine I_0 and I_t and calculate the absorption: $A = -\log_{10}(T) = -\log_{10}(I_t/I_0) = \log_{10}(I_0/I_t) = \varepsilon cl$, where T is the transmittance and ε is the wavelength dependent molar extinction coefficient ($\varepsilon = k/2.303$).

Once the sample is excited, it can relax via a set of radiative or non-radiative processes that were discussed in detail in chapter 2. The amount of emitted photons relative to the number of absorbed photons (quantum yields, QYs) of the light harvesters were estimated by comparison with quantum yield of standard fluorophores.⁹⁸

3.2. Time-Resolved Spectroscopy

In contrast to steady-state measurements, where we investigate averaged events in a sample upon continuous illumination, the time-resolved spectroscopy provides the ability to resolve physicochemical events collectively induced by light in real time. Time-resolved processes can be studied once matter interacts with a pulse of light, the width of which is shorter

than the decay time of the process under investigation. To detect the ultra-fast events (the main scope of this thesis) initiated by light absorption, high-speed detection systems with sophisticated electronics and optics are required. Thus, as tools I use laser-based systems – transient absorption (TAS, TIRAS) and transient photoluminescence (TRPL) spectroscopy methods.

The kinetic processes induced by excitation and charge transfer events were in the focus of this thesis. Desired kinetic traces were extracted from the time-resolved data by plotting the intensities of the signal (absorption, emission changes) at specified wavelengths and their decay over time. Further analysis was done with a home-written Matlab code by fitting kinetic traces as sum of single exponential decays $I(t) = \sum_{i=1}^n \alpha_i \exp(-t/\tau_i)$, where α_i stands for the amplitudes of the components at $t=0$. In some cases, e.g. paper I, there was a need of using a stretched exponential function. Lifetimes were extracted by global and single wavelength fitting procedures. During photoluminescence studies I assumed that the excited-state population decayed as $dn(t)/dt = (\Gamma + k_{nr})n(t)$, where Γ and k_{nr} were the corresponding radiative and nonradiative rate constants. Additional corrections for chirp (wavelength dependent factor of overlap between pump and probe) and cross-phase modulation artifact (pump and probe non-linear interaction) were performed in case of transient absorption data.

3.2.1 Time-Resolved Absorption

Time-resolved absorption spectroscopy methods are pump-probe techniques. Here, the kinetics of the involved processes can be measured by the applied change of the time delays between the pump (monochromatic excitation of the sample) and the probe pulses (measuring the pump-induced sample alterations, Figure 5).

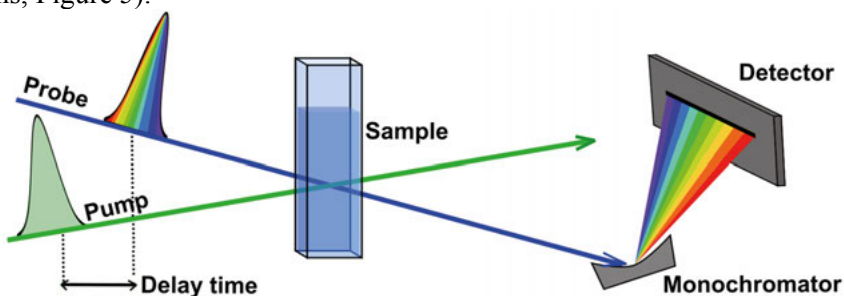


Figure 5. Scheme for pump-probe measurement.

I have used either UV-Vis light (polychromatic laser pulse) or mid-IR light as the sources of probe light to promote either electronic or vibrational excitations (Figure 6) within the sample. The first method is further denoted as the transient absorption spectroscopy (TAS), while the second one as transient infrared absorption spectroscopy (TIRAS). For our setups, delay of either

pump (in TIRAS) or probe light (in TAS) to obtain the kinetic data, was done by sending them through an optical delay line. Here the path length was changed, but direction and position of the beam remain unchanged.

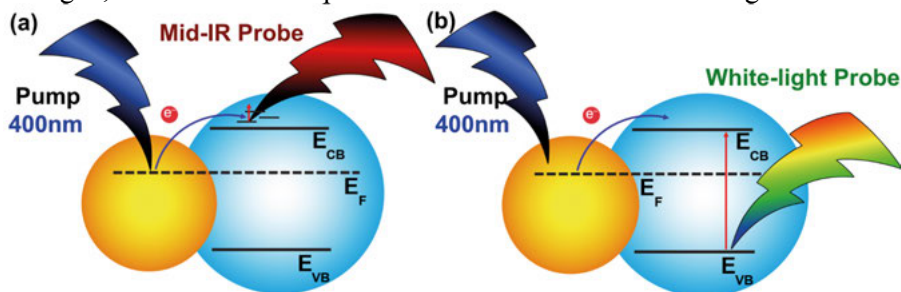


Figure 6. Example of ultrafast transient absorption spectroscopy design with 400 nm pump light, and (a) probe in mid-infrared region for monitoring vibrational transitions and (b) white-light probe for monitoring electronic transitions.

During excitation, only a small fraction of the sample is excited. To account for contribution from unexcited species, it is common to subtract the unpumped sample spectrum (before excitation) from the pumped spectrum (after sample excitation). The resulted difference spectrum can originate from one or several of the following effects: (a) induced absorption (IA), (b) ground-state bleach (GSB) and (c) stimulated emission (SE). IA arises as a positive feature from the newly formed species upon excitation, while GSB appears as a negative feature in the spectrum due to the decrease of ground state population by the formation of the excited state population. SE is seen as a negative signal due to emission of a photon in the same direction as a probe pulse that targeted this molecule, hence the detector will see more light than was sent in.

In semiconductors and nanoparticles TIRAS is seen as a sensitive tool to probe free carriers in the conduction and/or valence band. In case of difference spectrum for nanoparticles after the excitation of plasmon absorption band, it will contain features of overall plasmon dynamics, namely electron-electron, electron-phonon and phonon-phonon scattering (see chapter 2.3).

The fs laser setup has three main components for the generation of ultra-short pulses – a seed laser, a pump laser and an amplifier. In the seed laser the mode-locked 800 nm pulses are generated, which are then temporally stretched from fs to ns and then subsequently amplified using the pump laser in the Ti:Sapphire amplifier, and subsequently compressed again. The generated beam is split by a beam splitter into two fractions – first fraction is used to create the desired excitation wavelength either in an optical parametric amplifier (TOPAS) or by using a doubling crystal (for the generation of 400 nm light), while the second one is used for the generation of the desired probe light (UV-Vis or mid-IR light). The difference spectrum is generated by measuring the absorbance with and without excitation (pump) with the

help of the chopper, which blocks every other pulse. The more detail specifications of the used instruments can be found in experimental sections of the manuscripts.

3.2.2 Time-Resolved Photoluminescence

Ultrafast photoluminescence events were studied with the help of a streak-camera. Among advantages of using this technique was the ability to simultaneously resolve emission signals in energy, intensity, and time. After sample excitation with a monochromatic femtosecond laser pulse, the emitted photons reach the photocathode and are converted to electrons in quantities proportional to the intensity of the light. The electrons are subsequently passed through a voltage sweep where they are deflected vertically and in different angles before entering the micro-channel plate. Here electrons are multiplied and sent to a phosphor screen. On the phosphor screen, multiplied electrons are converted to light to produce a phosphor image. The optical pulse that reached the phosphor screen first is set in the uppermost position, while all others are set beneath in order. Here, brightness of the phosphor image will be proportional to the intensity of corresponding optical pulse, while the location on the phosphor image will provide time-space information. Finally, high-sensitive camera reads the overall time-wavelength-intensity resolved data (Figure 7).

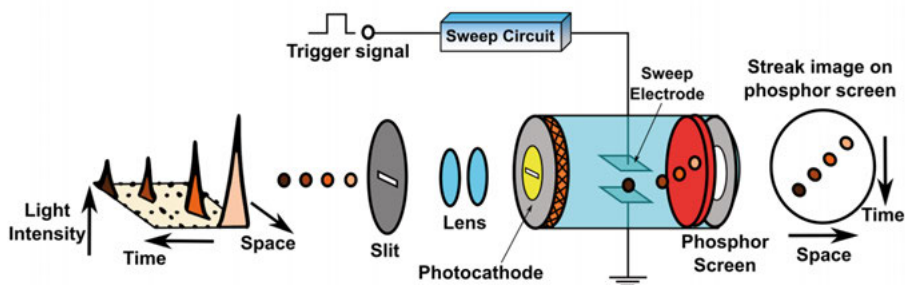


Figure 7. Operating principle of the streak camera tube.

Some of the samples showed long lifetimes (>2 ns), which were out of the detection range. Consequently, their emission was analyzed with flash photolysis nanosecond setup.

To overcome the problem of sample damage due to prolonged excitation, the samples were circulated in a microliquid jet, which provides the constant stream of fresh, undamaged sample.⁹⁹

3.3 Photocatalysis and Energy Conversion Efficiency

Photocatalytic studies were performed using a photoreactor connected to both a quadrupole mass spectrometer (QMS) and a UV-Vis spectrometer with a fiber optic cable.¹⁰⁰ The general scheme of the photoreactor is depicted in Figure 8. The sample was placed inside a 4 ml quartz cuvette and illuminated with the monochromatic continuous wave (CW) laser light, which was focused on the sample by a mirror. Continuous stirring provided homogeneous distribution of the sample inside the cell. Perpendicularly to the CW laser, UV-Vis fiber optic cables were connected for simultaneous detection of the spectral changes during photocatalysis. Produced gaseous products were extracted from the solution with the help of an inert carrier gas (argon). The mass-flow controller regulated the flow of Ar to be 16 mL/min. Afterwards, the photo-reactor gaseous exhaust was connected directly to the transmission quadrupole mass-analyzer (QMS) via a heated capillary.

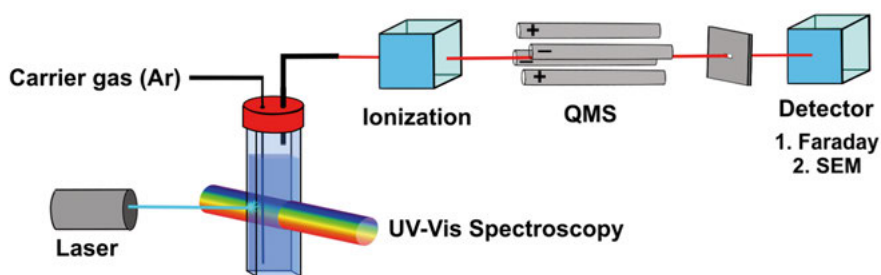


Figure 8. Operating principle of photo-reactor.

The QMS is composed of four parallel metal rods with electrically interconnected opposing pairs. By varying the applied voltage, QMS scans through a range of m/z values and transmits the ions with certain mass to charge ratio. Here “ z ” is the number of elementary charges of the ion. Finally, transmitted ions reach one of the available detectors: a Faraday cup detector or a secondary electron multiplier. The Faraday detector is made of a conductive metal cup designed to catch charged particles in vacuum. The amount of charges carried by the ions can be determined from the electrical charge generated during bombarding of the Faraday cup. It is accurate ($K = 10^{-4} \text{ A/hPa}$),¹⁰¹ but is less sensitive than the secondary electron multiplier detector. The secondary electron multiplier is more suitable for detection of small ion currents ($K = 10 \text{ A/hPa}$). Here the initial signal is amplified as the ions strike a sheet of metal known as a dynode. In this case generated multiple secondary electrons will strike nearby dynodes between which a positive voltage is applied, and promote generation of even higher amounts of secondary electrons.

For H_2 evolution reactions, both secondary electron multiplier and Faraday detectors were calibrated with the reference gas: 7.5% H_2 in Ar. The production flow rate (mL/min) of hydrogen was calculated from the ideal gas law.

The efficiency is a key measure for defining conversion of solar light into chemical fuel. The predicted theoretical efficiency is slightly above 30 %.¹⁴ Solar-to-hydrogen efficiency (η_{STH}) is generally defined as hydrogen energy output from solar energy input.¹⁰² As during photocatalysis I used monochromatic irradiation of a selected light absorber, the efficiency was calculated as photon-to-hydrogen quantum yield (η_{PTH}). At first, I determined the energy of photons, from the laser wavelength used: $E_{\text{photon}} = h \cdot c / \lambda$. Afterwards I determined how many of those photons were absorbed by our system within the course of photocatalysis by subtracting the non-absorbed photons from the total number of photons incident on the sample. Finally, photon-to-hydrogen quantum yield was calculated as:

$$\eta_{\text{PTH}} = \frac{2N_{\text{H}_2}}{N_{\text{hv}}} \times 100 \%$$

The amount of photogenerated H_2 molecules per time unit was determined from the production flow rate (mL/min).

4. Natural Dye for Solar Energy Conversion

This chapter will introduce the application of a natural dye capable of generating two electrons per photon absorbed, and the possibility to extract photo-generated charges with the help of a molecular electron relay.

4.1. Betanin as Promising Photosensitizer

The allure in using betanin, a natural dye, as the light absorber lies in its ability to inject two electrons upon one photon absorption.¹⁰³ As presented in chapter 1.3, there are several ways to achieve accumulation of multiple redox equivalents necessary for H₂ formation. Among them, there is the possibility of direct generation of multiple carriers upon one photon absorption. In 2008, McHale *et.al.*¹⁰⁴ reported the first utilization of betanin in DSSCs with incident photon-to-current conversion efficiencies over 100 % (data were corrected for unavoidable reflection and absorption losses). Moser and coworkers suggested that upon one photon absorption betanin undergoes simultaneous injection of two-electrons, leading to a doubly oxidized product. The enzymatic oxidation of betanin proved also to proceed through the formation of doubly oxidized product, 2-decarboxy-2,3-dehydrobetanin; similar to that formed upon photon absorption.¹⁰⁵ Lastly, the slope of the electrochemical potential for betanin oxidation -0.034 ± 0.003 V/pH under pH dependence studies suggested a two-electron one-proton oxidation.¹⁰³

In general, natural dyes,¹⁰⁶⁻¹⁰⁷ such as betalains, with high absorption coefficients in the visible region, are promising materials for solar light utilization. They can be used as replacement of highly expensive noble metal-based dyes and other materials harmful to the environment. Betalains can be found in beetroot *Beta vulgaris*; flowers, fruits, leaves, stems, roots etc., as pigments in plants of the order *Caryophyllales*. The betalain dye family is composed of yellow-orange (betaxantines) and red-violet (betacyanins) dyes with absorptions in the range of 340–520 nm and 350–650 nm, respectively. Betanin, used in this thesis is a Schiff base adduct composed of betalamic acid and cyclo-DOPA 5-O-glucoside. Although efficiency of betalains DSSCs has been found to be low (<1 %),¹⁰⁴ there are ongoing studies for improving it.^{108,109} For example, an increase in photovoltaic conversion effi-

ciencies was achieved during the purification of the plant extracts. The reports strengthen the prospect of using these types of dyes in DSSCs offering both biocompatibility and sustainability.

The main drawback in betanin systems relates to the short lifetime of the excited state as the result of the efficient $S_1 \rightarrow S_0$ internal conversion.¹¹⁰ Inter-system crossing $S_1 \rightarrow T_1$, typically observed for ruthenium dyes, has not been observed for betanin. This appears to preclude the use of betanin for the production of solar fuels. N,N'-dimethyl-4,4'-bipyridinium (also known as methyl viologen, MV^{2+}) is well-known for its long-lived reduction products ($MV^{\cdot+}$ and MV^0), and therefore, its ability to act as an electron relay between the light absorber and the proton reduction catalyst.¹¹¹ Here I studied the possibility of extraction of electrons photogenerated by betanin, through the addition of MV^{2+} as the electron relay.

4.2. Electron Dynamics

The photovoltaic efficiencies of betanin based DSSCs are dependent on the purity of the extracted samples. Thus, it was decided to compare properties of the two materials. First – betanin purchased from Sigma Aldrich (B_c), second – betanin extracted and purified from commercial beetroots by the procedures listed in ref. 112 (B_p , e.g. gel permeation chromatography and reversed-phase high-performance liquid chromatography).

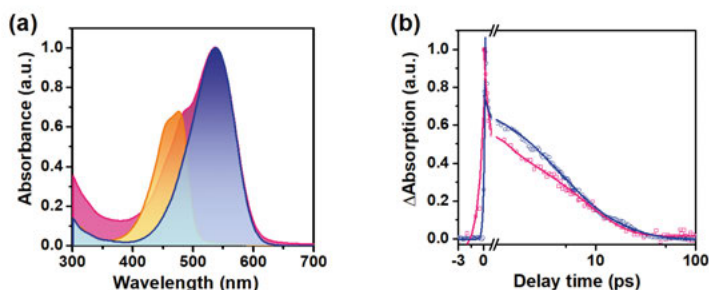


Figure 9. (a) Normalized absorption spectra of commercial (B_c , purple line) and purified (B_p , dark blue) betanin. Orange curve represents absorption spectrum of betalamic acid. (b) Kinetic traces extracted from femtosecond transient UV-Vis absorption spectra at 450 nm for B_c and B_p .

The absorption spectra of two betanin samples (purchased and purified) are presented in Figure 9a. The spectrum of commercial betanin has two pronounced bands centered closely at 478 nm and 536 nm. Earlier, Bastos *et.al.* showed that betaxantines and betanin isomers (betanin, isobetanin, neobet-anin) contributed to 478 nm and 536 nm bands, respectively. In contrast to B_c , the spectrum of purified betanin, B_p (blue curve) showed one Gaussian-shape like band with absorption maximum at 536 nm. Here, RP-HPLC analysis enabled separation of two optical isomers (betanin and isobetanin). This

was possible due to a longer retention time of isobetanin, and due to its stronger interaction with nonpolar stationary phase.¹¹³ NMR studies proved that purified betanin was composed of only one isomer – betanin.

The lifetimes of electronically excited betanin samples (B_c and B_p) were estimated and compared with the help of ultrafast transient spectroscopy ($\lambda_{exc} = 532$ nm, Figure 9b). In both cases transient spectra were characterized by a positive transient absorption band with maximum at ≈ 450 nm (IA), and two negative bands corresponding to GSB (530 nm) and stimulated emission (≈ 650 -750 nm). Figure 9b shows the femtosecond transient absorption (TA) kinetic traces extracted at 455 nm. Signals were fitted with biexponential decay resulting in 607 fs (61 %) and 7.7 ps (39 %) for commercial betanin, and 297 fs (43 %) and 6.8 ps (57 %) for purified betanin (Table 1). Although, similar lifetimes were found for the short-lived S_1 states, betanin purification resulted in a reduction of the contribution from the fast time component fraction by 1.5 times. Furthermore, the obtained lifetimes of the electronically excited species were too short for utilization by the catalyst, making an electron relay a necessity.

Table 1. Results of biexponential fitting of femtosecond transient data for B_c , B_p , $B_c|MV^{2+}$ and $B_p|MV^{2+}$.

	450nm		510nm		680nm	
Sample	τ_1 (A_1)	τ_2 (A_2)	τ_1 (A_1)	τ_2 (A_2)	τ_1 (A_1)	τ_2 (A_2)
B_c	0.61 (61 %)	7.7 (39 %)	0.55 (25 %)	8.9 (75 %)	0.84 (31 %)	8.3 (69 %)
B_p	0.3 (43 %)	6.9 (57 %)	0.4 (10 %)	8.1 (90 %)	0.1 (19 %)	5.2 (81 %)
$B_c MV$	0.50 (85 %)	7.0 (15 %)	0.37 (58 %)	6.57 (42 %)	0.08 (96 %)	5.2 (4 %)
$B_p MV$	0.35 (42 %)	6.6 (58 %)	0.41 (15 %)	7.7 (85 %)	0.08 (58 %)	6.47 (42 %)

τ_1 and τ_2 are the fast and slow components of the decay with respective amplitudes A_1 , A_2

Previous DFT calculations showed that betanin photoexcitation resulted in a shift of electron density from HOMO (-5.2 eV vs vacuum energy level) to LUMO (-3.1 eV),¹¹⁴ providing a significant driving force for the electron to be further injected to MV^{2+} . Moreover, the ability of MV^{2+} to harvest two electrons by forming relatively long-lived species made it a possible electron relay.

Evidence of betanin capability to generate two electrons per photon absorbed was gained during pH dependent electrochemistry studies (Figure 10, Table 2). Cyclic voltammograms of the $B_p|MV^{2+}$ system were recorded at pH 3.5, 4.5, 5.5, and 8. The data for the redox processes in the $B_p|MV^{2+}$ system are compiled in Table 2. The currents I_p for betanin, MV^{2+} and $B_p|MV^{2+}$ mixture were linearly dependent on $v^{1/2}$ (where v is scan rate in $V \cdot s^{-1}$) that indicates a diffusion-controlled process. As the pH decreased from 8 to 5.5, a shift of 60 mV/pH was detected, which can be rationalized by a $1e^-$ oxidation. However, at the lower pH range from 5.5 to 3.5 the redox potential of B_p

shifted negatively by 30 mV/pH most likely due to a two-electron, one-proton oxidation. The reversibility of the process was decreasing as the pH decreased, which may be explained by the protonation of the reduced species at low pH. The cyclic voltammograms for the mixture of betanin and methyl viologen ($B_p|MV^{2+}$) at pH = 4.5 (Figure 10b) showed that the first reduction wave (E_{pc}^1) has shifted by 30 mV towards less cathodic potentials and a second reduction peak (E_{pc}^2) has shifted by 20 mV to higher negative potentials in respect to pH = 3.5. In contrast to B_p and MV^{2+} , the first reduction wave at pH = 4.5 was of almost twice the intensity, when both betanin and methyl viologen were present ($B_p|MV^{2+}$).

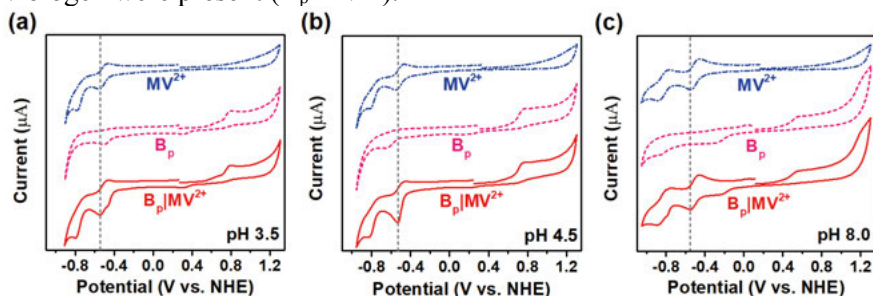


Figure 10. Cyclic voltammograms for B_p (pink, dashed line), MV^{2+} (blue, dot-dashed line), and $B_p|MV^{2+}$ (red, solid line) at pH = 3.5 (a), 4.5 (b), and 8 (c).

Table 2. Estimated redox potentials for B_c , B_p , $B_c|MV^{2+}$ and $B_p|MV^{2+}$ at pH 3.5–8.

	pH = 3.5				pH = 4.5				pH = 8			
Sample	E_{pa}^1	E_{pa}^2	E_{pc}^1	E_{pc}^2	E_{pa}^1	E_{pa}^2	E_{pc}^1	E_{pc}^2	E_{pa}^1	E_{pa}^2	E_{pc}^1	E_{pc}^2
B_p	0.68	0.79	-0.5		0.64	0.76			-	0.58		
MV			-0.55	-0.78			-0.55	-0.81			-0.55	-0.87
$B_p MV$	0.68	0.79	-0.55	-0.8	0.64	0.76	-0.52	-0.83	-	0.58	-0.55	-0.89

Up to now most of the research was focused on application of betanin in DSSCs. However, there were no reports for the betanin application in direct solar fuel generation (e.g. hydrogen). Within our work H_2 evolution studies were performed with the help of a flow photoreactor with mass-spectrometry detection of released gaseous products. A photocatalytic system based on purified betanin turned out to be photocatalytically inactive. As for commercial betanin, it was found that amounts of evolved H_2 were batch-dependent. Various amount of H_2 were detected for B_c , while showing no hydrogen evolved in some of them. Thus, giving an idea that additives in commercial betanin (maltodextrin, ascorbic acid, and citric acid) play a crucial role in hydrogen evolution reaction. We have performed several photocatalytic tests adding sequentially and/or simultaneously maltodextrin, ascorbic acid, and citric acid to the purified betanin sample. However, no hydrogen was generated, thus suggesting that other impurities than maltodextrin, ascorbic acid, and citric acid, are responsible for photocatalytic activity of commercial betanin.

To understand the electron dynamics in the $B|MV^{2+}$ system, ultrafast transient measurements were performed for $B_p|MV^{2+}$ and $B_c|MV^{2+}$. Figure 11 represents kinetic traces extracted at 455 nm for both betanin samples after the addition of methyl viologen (Table 1). Surprisingly, no effect of MV^{2+} on the excited state lifetime was observed for purified betanin B_p , but the addition of MV^{2+} to commercial betanin B_c , resulted in a doubling of the contribution of the fast time component. Moser *et.al.* observed a similar signal and assigned it to the electron injection from excited betanin into the electron relay (TiO_2). Considering this and the initially short lifetime of betanin, we could suggest that the electrons transfer from photoexcited betanin B_p to MV^{2+} is carried out via a charge transfer complex.

The possibility of the formation of a complex between betanin and methyl viologen was studied with using UV-Vis spectroscopy measurements and DFT calculations. During the UV-Vis titration of the $B_c|MV^{2+}$ mixture, no evidence of the formation of a charge transfer complex was observed. Moreover, theoretical calculations predicted very low interaction between betanin and methyl viologen cations and rather a dynamic equilibrium between betanin and MV^{2+} species in water solution.

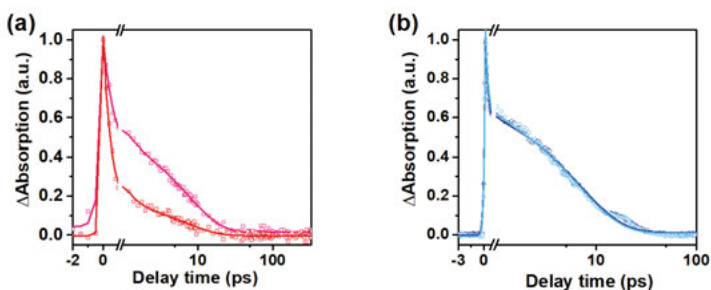


Figure 11. Kinetic traces extracted for (a) B_c (purple), $B_c|MV^{2+}$ (red) and (b) B_p (dark blue), $B_p|MV^{2+}$ (light blue) from femtosecond transient UV-Vis absorption spectra at 450 nm upon excitation at 532 nm.

Despite the observed increase in the fast component fraction, transient absorption spectra of $B_p|MV^{2+}$ and $B_c|MV^{2+}$ had no characteristic signatures of MV^{2+} reduction products – MV^{+} and MV^0 , suggesting that electron transfer to methyl viologen did not occur, and the increase of the fast component fraction in case of B_c has other reason. Moreover, interpretation of the electron dynamics became even more complicated due to an overlap of the excited state absorption of betanin with its predicted doubly oxidized product. All these indicate that other processes beside the electron transfer from betanin to methyl viologen is the reason for the increase of the fast component fraction. The direct effect of MV^{2+} on the excited state of commercial betanin could be, for example, due to its interaction with the additives present in commercial betanin – maltodextrin, ascorbic acid, citric acid – as well as isobet-

anin/neobetanin isomers and betaxantines, but not with betanin itself. However, these studies were out of the scope of this thesis, as the desired extraction of short-lived electrons by methyl viologen did not occur.

4.3. Summary and Outlook

In this chapter, I investigated the possibility of harvesting two electrons photogenerated upon betanin excitation. First, I observed that betanin purification results in favorable decrease of the fast time component fraction in TAS. The possible generation of double reduced product was gained from electrochemistry studies, where the 30 mV/pH shift of E_{pa}^2 for the B|MV²⁺ mixture was detected. Ultrafast transient spectroscopy studies revealed that addition of MV²⁺ did not affect the overall electron dynamics in the system with purified betanin B_p, as was observed for commercial betanin B_c. The increase of the fast time component extracted at 450 nm for B_c|MV²⁺ was similarly observed by Moser *et.al.* for the B|TiO₂ system, and assigned to electron injection into the electron relay (methyl viologen in our case). The absence of detectable long-lived species MV^{•+} and MV⁰ made the further interpretation of an electron accumulation by MV²⁺ inconceivable. Moreover, the understanding of the underlying processes became even more puzzling due to the overlap of excited state absorption of betanin with its photogenerated intermediates. H₂ evolution studies showed no hydrogen production. Taking all into account, the results of charge harvesting for B_c|MV²⁺ system were ambiguous.

The direct bond between betanin and methyl viologen could have promoted electron transfer from the short-lived photoexcited state of betanin to the electron relay. However, the absence of charge transfer complex precluded that. Thus, for further studies we would require an addition of electron relay able to bind directly to betanin. Previously several groups showed possibility to harvest short-lived photogenerated charges by anchoring betanin on a semiconductor surface. The most studied semiconductor for betanin-based DSSCs was TiO₂. Our idea is that a semiconductor with higher electron mobility than TiO₂ can improve harvesting of photogenerated charges and lead to direct generation of the solar fuel, namely H₂ evolution (see chapter 5.2).

5. Towards Ultra Long-Lived Charge Separation with Semiconductors

5.1. Aim of the Study

In this chapter, I will present the application of semiconductors, both as electron relays for prolonging charge separation and as direct light absorbers in the visible region, for possible hydrogen generation.

To start with, I will discuss the possibility to extract and harvest short-lived photogenerated charges by direct anchoring of betanin to a semiconductor. Previously, in chapter 1.4, I have introduced the general requirements for the semiconductors for solar light harvesting. TiO_2 and ZnO are amongst the most commonly used n-type semiconductors due to their beneficial position of the CB edge in respect to the H_2 evolution redox potential, and the low-cost, non-toxicity, and the abundance of these materials. In contrast to TiO_2 , ZnO has low stability in particular in aqueous conditions. In the dye sensitized solar cells (DSSC) field, TiO_2 could not reach efficiencies higher than 3% for betanin-based system.¹⁰⁹ ZnO has orders of magnitude higher electron mobility making it a promising candidate for application in the betanin solar cells. The work presented in this thesis is based on unique properties of water-soluble and stable ZnO nanocrystals (NCs) towards accumulative charge separation in the system with betanin as a light harvester.

Secondly, I will introduce a perovskite semiconductor, CsPbBr_3 , as a direct light absorber in the visible region. In the last years lead-halide perovskite materials became a topic of intense research due to their high power conversion efficiencies in solar cells.^{115,116} The main advantages of using lead-halide perovskites were based on their exceptional optoelectronic properties (tunable absorption, long carrier lifetime,¹¹⁷ and both high electron and hole mobility).¹¹⁸ In this chapter, I will use light harvesting properties of CsPbBr_3 for hydrogen production with Ru nanoparticles supported on TiO_2 . The electron dynamics upon light absorption and strategies to eliminate undesired non-radiative recombination will be in focus.¹¹⁵ Furthermore, the effect of magnetic field on photoluminescence properties of CsPbBr_3 will be discussed, as it has been suggested that it could improve the quantum efficiency.

5.2. ZnO Nanocrystals as Electron Relay (Papers I-II)

5.2.1. Sample Characterization

Earlier in chapter 4 it was shown that the molecular electron relay – methyl viologen – cannot directly harvest short-lived photogenerated charges from betanin, most likely due to the absence of direct contact with dye. In this chapter, hydrogen generation was studied for the linked system, which had three main constituents: light-harvester, electron relay, and H_2 evolving catalyst (Figure 12). The first component in this scheme is betanin (B); the light harvester that upon excitation with light is capable of promoting an electron from the HOMO to LUMO level with further injection of electrons into the CB of the semiconductor. The second component is a direct band gap semiconductor ZnO (electron relay), which would store injected from betanin to ZnO CB electrons for long enough time. Third component, the FeFe-hydrogenase mimic catalyst (the third component)¹¹⁹⁻¹²³ would use the electrons from the ZnO CB to produce hydrogen via proton reduction.

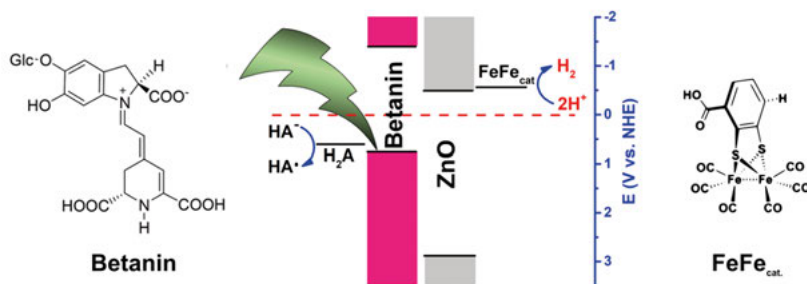


Figure 12. Energetic diagram for B/ZnO-OEG/FeFe_{Cat} for H_2 fuel production.

Betanin (B) was previously characterized in chapter 4, and [FeFe(mcbdt)(CO)₆], further denoted as FeFe_{Cat}, was studied in detail in ref 124 and 125. Thus, here I will focus on the characterization of the ZnO semiconductor. Both physical and chemical properties of ZnO are strongly dependent on the crystallinity, size, morphology,¹²⁶ doping impurities,¹²⁷ ligand surrounding, origin of the precursor and synthetic method.¹²⁸⁻¹³¹ For example, it was shown that the most used sol-gel method often led to formation of nonuniform inorganic core-organic shell interfaces.¹³² Liquid phase ZnO precursors often demand organic additives and thus, subsequent high thermal treating temperatures, which could lead to an active surface diminishment.¹³³ Moreover, bare ZnO often suffers from low stability in both neutral and alkaline media.¹³⁴ Thus, reproducible synthetic procedures for high-quality ZnO are in demand.¹³⁵ Here, ZnO nanocrystals were synthesized by an organometallic approach.¹³⁶ These nanocrystals were decorated with 2,5,8,11-tetraoxatetradecan-14-oic ligand (Zn-OEG), and had a hydrodynamic diameter of 9 nm (Figure 13a).

Synthesized ZnO NCs showed the absorption centered at 373 nm, which is characteristic for ZnO (Figure 13b). The band gap of 3.33 eV was determined from a Tauc plot.^{137,138} Band gap excitation of ZnO-OEG resulted in generation of two emission bands centered at 404 and 560 nm with low and high intensities respectively. Based on literature data, the emission with lower intensity was assigned to recombination of shallow trap electrons (0.26 eV below CB) with VB holes.¹³⁹ The second emission was more pronounced with a quantum yield of 19.8 %, ¹⁴⁰ and originated from electrons trapped 0.26 eV below CB with deep trap holes located at 0.86 eV above the VB edge.¹⁴¹

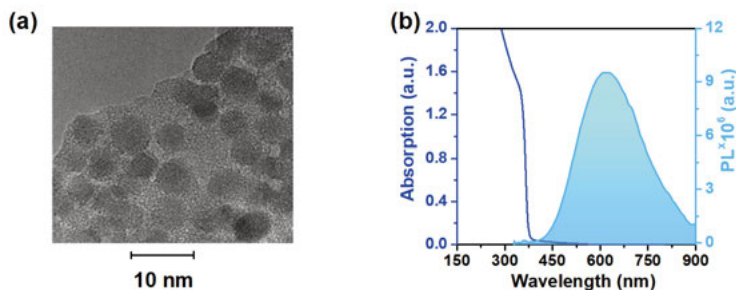


Figure 13. (a) High resolution TEM of ZnO-OEG NCs; (b) UV/Vis absorption and photoluminescence ($\lambda_{exc.} = 355$ nm) of ZnO-OEG NCs in aqueous solution.

The ZnO NC's surface was covered with OEG ligand ≈ 20 %, thus leaving space for the co-absorption of a natural dye and a catalyst via the -COOH anchoring groups. UV-Vis spectroscopy and DLS showed that ZnO nanocrystals were most stable under pH = 3–9, while betanin was stable under pH = 3–5. Thus, further anchoring studies were performed at pH 3–5.

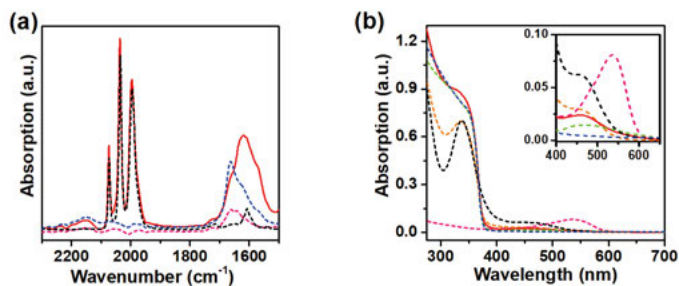


Figure 14. (a) FTIR spectra of betanin (purple), FeFeCat (black), ZnO-OEG NCs (blue), and mixture of all three B|ZnO-OEG| FeFeCat (red) in DMSO; (b) Steady-state absorption spectra of ZnO-OEG NCs (blue), B (purple), FeFeCat (black), B|ZnO-OEG (green), ZnO-OEG| FeFeCat (orange); and mixture B|ZnO-OEG| FeFeCat NCs (red).

The coordination of betanin and the $[\text{FeFe}(\text{mcbdt})(\text{CO})_6]$ catalyst was monitored with the help of UV-Vis and FTIR spectroscopy (Figure 14a). The UV-Vis spectrum of the B|ZnO-OEG| FeFeCat system had characteristic blue-shifted bands of betanin and $[\text{FeFe}(\text{mcbdt})(\text{CO})_6]$ (Figure 14b). Based on extinction coefficients and on the intensities of the corresponding bands, the

ratio between co-absorbed betanin and $[\text{FeFe}(\text{mcbdt})(\text{CO})_6]$ was estimated to be $\approx 1:1$. The edge of ZnO absorption remained unchanged, suggesting that no additional trap states were created. Fourier transformed infrared (FTIR) spectrum after anchoring of the catalyst to ZnO NCs decorated with co-absorbed betanin, resulted in the appearance of three additional characteristic ν_{CO} vibrations from the ligand surrounding of $[\text{FeFe}(\text{mcbdt})(\text{CO})_6]$. An additional increase of the hydrodynamic diameter was observed by DLS upon anchoring of dye and catalyst to ZnO NCs. The crystallinity of ZnO was not affected during the above stated surface modifications.

5.2.2. Time-Resolved Spectroscopy Studies

Electron dynamics in the designed linked system was analyzed with the help of time-resolved spectroscopy tools. The energy diagram of the B|ZnO-OEG| FeFe_{Cat} system shows that the electron transfer from the photoexcited betanin to catalyst will occur with an electron transfer driving force of 0.86 eV.

I investigated the process of electron injection from the anchored betanin to the conduction band of ZnO-OEG with the help of ultrafast transient absorption spectroscopy. The sample was excited at 532 nm, and probed not in the UV-Vis region as for B|MV sample in chapter 4, but instead probed in the mid-infrared range. The mid-infrared probe range was chosen due to its sensitivity to electrons in the CB of the semiconductor. The pump of 532 nm enabled selective excitation of the dye only. The energy of this light was not sufficient to directly excite ZnO NCs, thus no signal was observed for bare ZnO (Figure 15a, blue). For betanin anchored to ZnO the excitation resulted in broad mid-IR absorption, which did not decay within the experimental delay time (≈ 5 ns). A broad mid-IR absorption signal detected for B|ZnO-OEG appeared due to the free charge carriers within the CB of the semiconductor. In contrast to the B|MV sample, where we could not extract electrons by methyl viologen, the exploitation of the ZnO semiconductor enabled charge extraction from the photoexcited betanin. Corresponding kinetic traces for B|ZnO-OEG at 1897 cm^{-1} are presented in Figure 15. The rising edge was fitted with two components of 1.3 and 14.0 ps, which was longer than the instrument response function (our IRF = 200 fs). These time constants were assigned to the electron injection from betanin to ZnO-OEG. The lifetime of the electrons in the ZnO NCs CB, after injection from betanin, was determined by ns TAS (i.e. flash photolysis), with mid-IR probing after 532 nm excitation. The kinetic trace extracted at 2050 cm^{-1} was fitted as a sum of two exponentials with the lifetimes of 1.5 μs (84 %) and 20.6 μs (16 %), plus a more long-lived component ($>100\text{ }\mu\text{s}$). In the inset of Figure 15b, one can see that injected electrons remain in the CB of ZnO-OEG up to one second. In such a way, anchoring of betanin to ZnO NCs resulted in two positive outcomes. First, it allowed us to extract electrons from the short-lived excited

state. Second, it increased the charge separated state lifetime to the $\sim\mu\text{s}$ -s range, which was sufficiently long to perform photocatalysis.

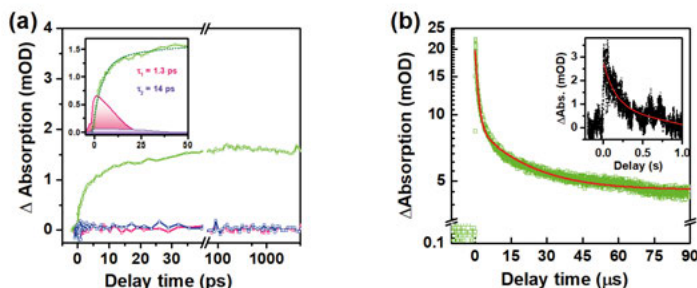


Figure 15. (a) Kinetics of betanin (pink), ZnO-OEG (blue), and B/ZnO-OEG (green) extracted at 1897 cm^{-1} from TIRAS spectra collected from 1850 to 2200 cm^{-1} in DMSO. Rising edge fittings for B/ZnO-OEG are depicted in the insert (IRF = ca. 200 fs); (b) Kinetics of B/ZnO-OEG extracted at 2050 cm^{-1} from ns TIRAS spectra collected from 1850 to 2200 cm^{-1} ($\lambda_{\text{exc.}} = 532\text{ nm}$) in DMSO.

Nevertheless, prior to the analysis of electron dynamics with the catalyst, I decided to answer the question “Was ZnO-OEG directly responsible for the prolongation of the charges lifetime?” To answer the question I performed similar experiments on bare ZnO-OEG upon band gap excitation (355 nm). The ZnO-OEG showed two emission bands centered at 404 and 560 nm . The kinetics of these radiative events was studied with the help of a streak camera. The lower intensity emission (at 404 nm) decayed within 25 ps (Figure 16a). Based on literature data this emission was assigned to the recombination of trapped electrons with valence holes. The more pronounced emission at 560 nm showed a much longer lifetime, which could not be analyzed with the help of the streak-camera due to its short delay line (max. 2 ns). Thus, it was decided to follow the emission decay with the flash photolysis setup (Figure 16b). The obtained data were fitted as a sum of a single exponential (67% , $\tau_1 = 34\text{ ns}$) and a modified stretched exponential (33% , $\tau_1 = 2.2\text{ }\mu\text{s}$, $\beta = 0.56$). Here β value, estimated from the second stretched exponential function (Kolrausch–Williams–Watts function)¹⁴² is characteristic for nanocrystalline samples.¹⁴³ It is fascinating, that the observed radiative lifetimes for ZnO NCs, were drastically longer than those normally obtained for other ZnO - OEG samples ($\sim\text{ps}$ -ns).¹⁴⁴⁻¹⁴⁶

The ultra-long lifetime observed in bare ZnO-OEG NCs upon band gap excitation suggests the presence of a charge stabilization mechanism, and there are a number of possibilities. First, excited electrons can be trapped below the CB, thus leading to an increase in the lifetime of the system. Second – holes can be trapped, e.g. on an OEG shell, thus prolonging the time necessary for the electron to find a hole prior to recombination. Third, there is a combination of the two previously mentioned scenarios. To unveil the stabilization mechanism we have used a combination of EPR spectroscopy, and ns TAS with a probe in mid-IR range. EPR measurements did not reveal the

formation of a persistent radical species, thus suggesting that charge carriers were localized neither in the OEG shell, nor in the inorganic core. Nanosecond TAS data were compared for two samples - bare ZnO-OEG NCs and B|ZnO-OEG. This was performed to compare the relative lifetimes of the CB electrons when having either holes on the ZnO (ZnO-OEG, $\lambda_{\text{exc.}} = 355$ nm), or on the betanin (B|ZnO-OEG, $\lambda_{\text{exc.}} = 532$ nm). The kinetic trace extracted at 2050 cm^{-1} for ZnO-OEG, resulted in lifetimes of $1.2\text{ }\mu\text{s}$ (91%) and $15.1\text{ }\mu\text{s}$ (9 %) that were similar to those extracted for B|ZnO-OEG (Figure 16c). This proves the irrelevance of the origin of the electrons (direct band gap excitation or betanin excitation) as they are injected into the CB, and where the resulting holes reside. The overall lifetime will be unaffected. Thus, the most logical explanation is that upon electron injection into ZnO CB (ZnO-OEG system), the hole was trapped in the OEG ligands on the ZnO nanocrystals, and most likely delocalized there.

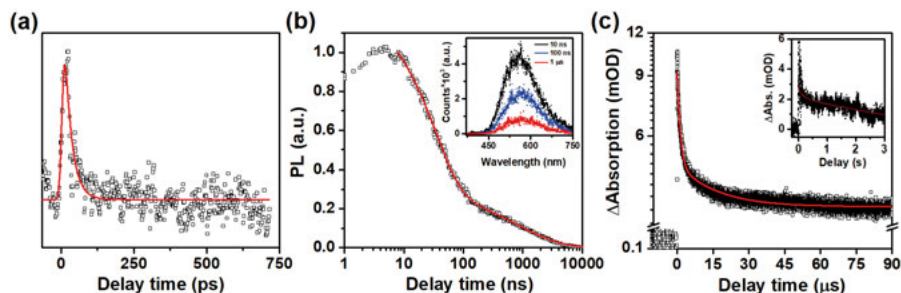


Figure 16. (a) Kinetics of ZnO-OEG NCs extracted at 404 nm with streak camera time-resolved fluorescence ($\lambda_{\text{exc.}} = 320$ nm) in aqueous solution; (b) Kinetics of ZnO-OEG NCs extracted at 560 nm from ns time-resolved fluorescence ($\lambda_{\text{exc.}} = 355$ nm) in aqueous solution, and selected spectra at different times in insert; (c) Kinetics of ZnO-OEG NCs extracted at 2050 cm^{-1} from ns TIRAS spectra collected from 1850 to 2200 cm^{-1} ($\lambda_{\text{exc.}} = 355$ nm) in DMSO.

Finally, once the catalyst was added, the complete B|ZnO-OEG|FeFe_{Cat} system was characterized with the help of ultrafast transient mid-infrared absorption spectroscopy. Upon betanin excitation ($\lambda_{\text{exc.}} = 532$ nm) the kinetics of electron injection into the ZnO conduction band remain unchanged. However, the electron dynamics inside ZnO CB changed drastically. An abrupt decay of the broad IR absorption signal was observed for the complete system, in contrast to that without the molecular catalyst. This meant that direct anchoring of [FeFe(mcbdt)(CO)₆] on a surface of ZnO NCs, promoted electron transfer from semiconductor conduction band to the catalyst. The corresponding kinetic traces extracted at 1897 cm^{-1} are presented on Figure 17a.

As our catalyst had characteristic ν_{CO} vibrations it was decided to further monitor its reduction upon electron transfer from ZnO CB, by nanosecond flash-quench measurements with detection in the metal-carbonyl region.

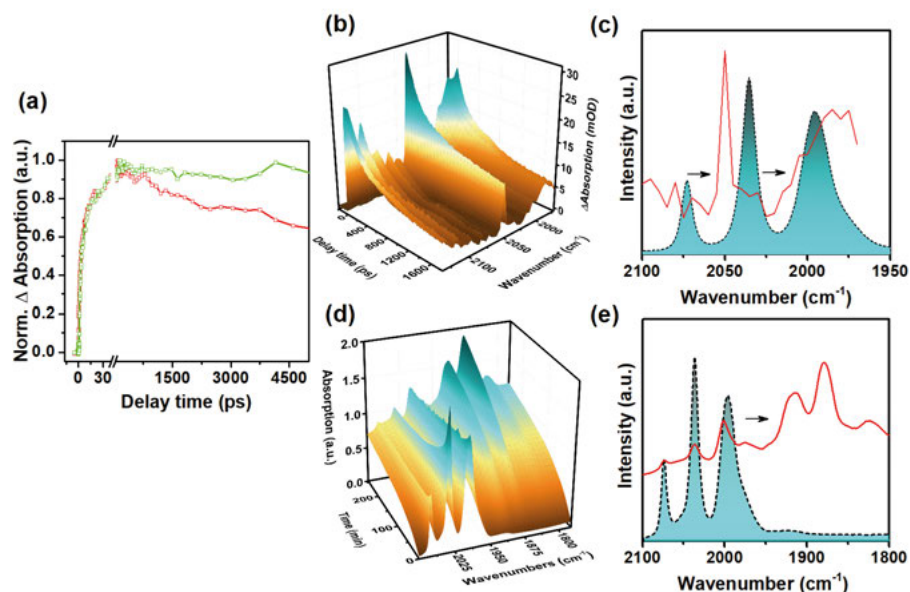


Figure 17. (a) Kinetics for B/ZnO-OEG (green), and B/ZnO-OEG/FeFeCat (red) at 1897 cm^{-1} extracted from fs TIRAS spectra collected from 1850–2200 cm^{-1} at $\lambda_{\text{exc.}} = 530$ nm in DMSO; (b) 3D surface plot of the ns TIRAS data for of B/ZnO-OEG/FeFeCat, and (c) FTIR spectra of [FeFe(mcbdt)(CO)₆] before (black) and 400 ns (red) after illumination ($\lambda_{\text{exc.}} = 530$ nm in DMSO) (d) 3D surface plot of TIRAS data for B/ZnO-OEG/FeFeCat and (e) FTIR spectra of B/ZnO-OEG/FeFeCat before (black) and 4 h (red) after illumination ($\lambda_{\text{exc.}} = 530$ nm in DMSO).

These studies were based on sensitivity of ν_{CO} vibrations to the electron density on the metal center of the catalyst. The resulted difference spectra after excitation of the B/ZnO-OEG/FeFeCat sample included the formation of two red shifted peaks (25–50 cm^{-1}), with the rise of the background that covered the bleaches of three initial $\nu_{\text{C-O}}$ peaks (Figure. 17b). The background rise appeared throughout the entire detection range due to the broad mid-IR absorption of free electrons injected from photoexcited betanin into the CB of ZnO-OEG. Based on literature data and DFT calculations two formed red-shifted peaks (25–50 cm^{-1}) were assigned to a singly reduced catalyst (Figure 17c).^{147,148} The parent catalyst complex [FeFe(bdt)(CO)₆], where bdt = benzenedithiolate, and its reduction products were characterized in detail, revealing the red shift of ν_{CO} peaks by 45–65 cm^{-1} . The doubly reduced [FeFe(mcbdt)(CO)₆]²⁻ species were detected upon further extension of probed region and time delay from ns to real time acquisition (spectra measured every 5 min, Figure 17d). A detected red shift (~ 120 –160 cm^{-1}) of initial ν_{CO} vibrations was in good agreement with the shift (~ 130 cm^{-1}) detected for the doubly reduced species obtained by spectroelectrochemical reduction of the parent [FeFe(bdt)(CO)₆] complex (Figure 17e).

5.2.3. Photocatalysis

Time-resolved spectroscopy studies revealed that combination of the electron relay semiconductor (ZnO-OEG NCs) and betanin enabled charge harvesting by electron injection from photoexcited betanin into the conduction band of ZnO-OEG NCs. Furthermore, electrons are driven to the anchored catalyst, thus reducing it. Last question to be answered was if one could utilize electrons for H₂ generation with the help of [FeFe(mcbdt)(CO)₆]. To answer this question we have ran the photocatalytic tests for the B|ZnO-OEG|FeFe_{Cat} system in a flow photoreactor upon CW illumination at 532 nm. After 4h 976 μ mol of hydrogen was evolved (Figure 18). No drastic change in intensity of initial ν_{CO} vibrations was observed in FTIR spectrum after catalysis. In contrast, the unlinked catalyst described in ref. 149 was degrading under similar photocatalytic conditions.

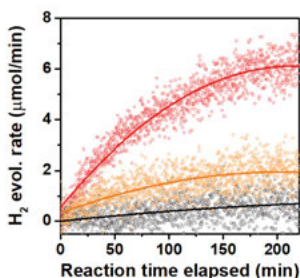


Figure 18. Time course of H₂ evolution photocatalysed by [FeFe(mcbdt)(CO)₆] (black), Zn-OEG|FeFe_{Cat} (orange), and B|ZnO-OEG|FeFe_{Cat} (red).

5.2.4. Summary and Outlook

In conclusion, unique properties of ZnO-OEG as an electron relay inside the linked system, B|ZnO-OEG|FeFe_{Cat}, lead to several positive outcomes. The fact that the ZnO-OEG surface is not fully covered allowed anchoring of the betanin and catalyst (~1:1) that promoted charge transfer. On the other hand, ZnO-OEG NCs allowed extraction of electrons from the short-lived excited state S₁ of betanin. In addition, hole stabilization within the OEG shell of ZnO nanocrystals caused drastic slowing down of charge recombination. Finally, the generation of long lived electrons inside the CB of ZnO-OEG allowed the biomimetic noble metal-free catalyst, [FeFe(mcbdt)(CO)₆], to reduce protons to evolve hydrogen.

The next step, after H₂ evolution studies in solution is the development of a complete dye sensitized solar fuel device based on the unique properties of ZnO-OEG described above in the text. In order to harvest more of the visible part of the solar spectrum, we may need to modify the band gap energies of the semiconductor.

5.3. CsPbBr₃ Nanocrystals as Light Harvester (Papers III-IV)

5.3.1. Sample Characterization

A short while ago, lead halide perovskites became promising materials in the field of solar cells, with efficiencies that increased abruptly from ~3 % to ≥ 20 % in just seven years.¹⁵⁰ These materials possess favorable features for solar light harvesting, e.g. absorption in the entire visible spectral range with strong optical absorption coefficients, long lifetime of charge carriers, and both high electron and hole mobility. However, stability,¹⁵¹ toxicity,¹⁵² and complexity still remain a challenge for application of the perovskite solar cells, even though in recent years many efforts have been done to circumvent the mentioned problems. Hagfeldt *et.al.* predicted that reduction of non-radiative recombination would lead to highest possible V_{OC} , fill factors, and over-all higher performance of perovskite solar cells.¹¹⁵

Fully inorganic perovskites with the general formula of CsPbX₃ (X = Cl, Br, I) have narrow emission linewidths (12-40 nm) with high photoluminescence quantum yields (~90 %) and relatively long radiative lifetimes (1–29 ns), thus making these materials a target for solar light harvesting. The absorption in the entire UV-Vis range (410-700 nm) is achieved by tuning band gap energies via a halide exchange mechanism in the colloidal nanocrystal solution. High defect-tolerance of these materials with no undesired mid-gap trap states stand for the narrow emission linewidths of CsPbX₃.¹⁵³

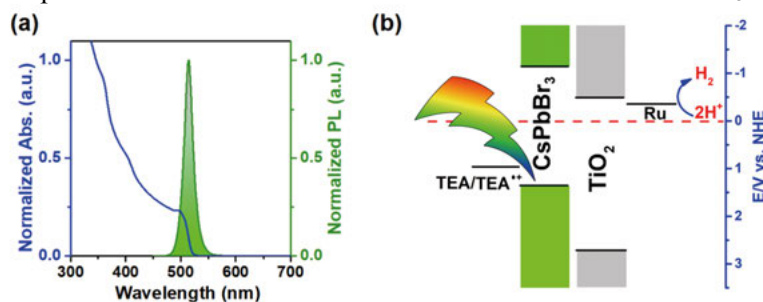


Figure 19. (a) CsPbBr₃ absorption (blue) and emission spectra (green); (b) energy diagram for the CsPbBr₃/TiO₂/Ru system with relevant CB, VB edge positions as well as redox potentials of used components.

In this chapter, a direct band gap semiconductor, CsPbBr₃, will be utilized as the light harvester that possesses favorable CB edge position for hydrogen evolution. Earlier studies on CsPbBr₃¹⁵⁴ revealed that these nanocrystals have an absorption characteristic for semiconductors (~510 nm) with a narrow emission upon band gap excitation centered at 515 nm (Figure 19a). Ru nanoparticles supported on TiO₂ served as hydrogen evolution catalyst in our investigated system with triethanolamine (TEA) as sacrificial electron donor. The energy diagram for this photocatalytic system is depicted in Figure 19b.

It is worth mentioning that the components in this system were not linked and all processes relied on collisions.

5.3.2. Photocatalysis

Perovskites suffer from low stability, thus suggesting that the photocatalytic conditions must be optimized with additional care. Ligand desorption, oxidation,¹⁵⁵ sensitivity to light, moisture, impurities, etc. are just a few factors that generally cause instability of perovskite samples.

Many instability problems can be omitted under controlled photocatalytic conditions. For instance, it was recently shown that CsPbBr₃ nanocrystals integrated into silica-alumina monoliths remained their stability under regulated diffusion of water into toluene.¹⁵⁶ Direct generation of hydrogen with CsPbBr₃/TiO₂/Ru system required a sacrificial electron and proton donor. As sacrificial electron donor triethylamine (TEA) was chosen, while as sacrificial proton donor was used trifluoroacetic acid (TFA). Therefore, it was decided to perform stability control measurements to determine the conditions favorable for performance of perovskite samples.

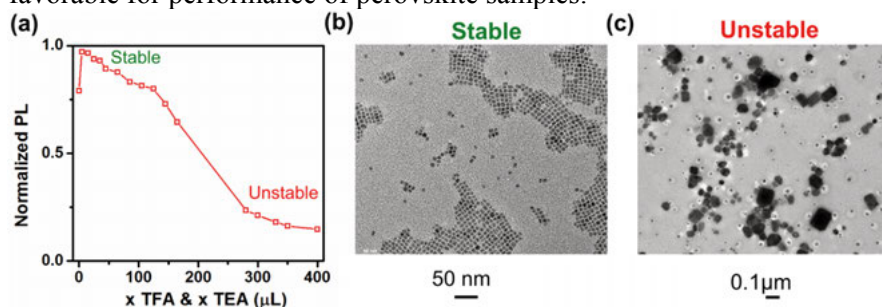


Figure 20. (a) The intensity of the photoluminescence signal of CsPbBr₃ (3 mg/mL) upon addition of various amounts (X = volume in μL) of TEA (1 M) and TFA (1 M); (b, c) Transmission electron microscopy micrographs of the CsPbBr₃ nanocrystals after the addition of 100 μL (b) and 300 μL (c) of TEA, TFA in DMSO.

Figure 20 depicts the influence of triethylamine and trifluoroacetic acid on the intensity of the photoluminescence signal of CsPbBr₃. As seen from the titration curve, the perovskite sample are stable, once the volumes of TEA (1M), TFA (1M) do not exceed 100 μL of each. This is further monitored on the TEM micrographs for CsPbBr₃ obtained in two different regions of TEA, TFA concentrations – $<100 \mu\text{L}$ (stable region) and $\geq 300 \mu\text{L}$ (unstable region). Under stable conditions crystallinity and cubic shape of CsPbBr₃ was unaffected. However, the crystallinity the distortion and the change of shape, suggested surface leaching under the unstable conditions. The data analysis suggested further usage of sacrificial electron and proton donor in quantities not exceeding 100 μL (30 mM) during photocatalysis.

The photocatalytic experiments were carried out upon monochromatic excitation (445 nm) of CsPbBr₃ in the presence of Ru nanoparticles supported

on TiO_2 , TEA and TFA as sacrificial electron and proton donors respectively. Figure 21a shows hydrogen evolution curves detected with QMS. The complete system ($\text{CsPbBr}_3/\text{TiO}_2/\text{Ru}$) was found to evolve hydrogen in the presence of TEA, and TFA, while control systems $\text{CsPbBr}_3/\text{TiO}_2$ and TiO_2/Ru turned to be inactive. In 50 min the rate of hydrogen production reached its maximum ($\sim 160 \mu\text{mol} \cdot \text{min}^{-1} \cdot \text{g}_{\text{cat}}^{-1}$) for the $\text{CsPbBr}_3/\text{TiO}_2/\text{Ru}$ system. In these experiments, QMS was detecting produced hydrogen extracted from the headspace by a carrier gas (Ar) as flow in real time, and not as accumulated quantities of product over time. The photon-to-hydrogen quantum yield (η_{PTH}) of this experiment was determined from the conversion of measured photon flux absorbed by the system and amount of hydrogen generated over certain time. Estimated yield, η_{PTH} , was $0.4 \pm 0.1\%$.

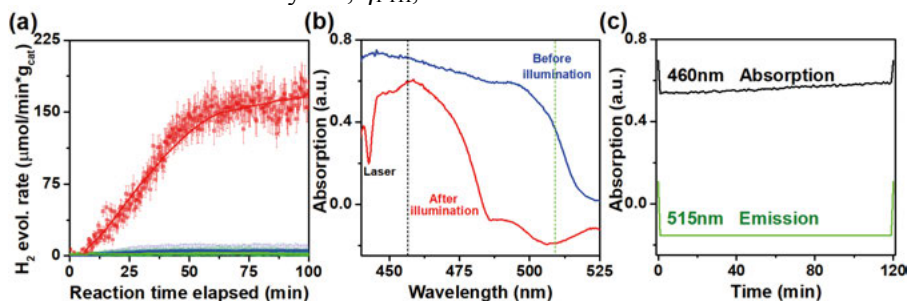


Figure 21. (a) The rate of hydrogen evolution per amount of used catalyst upon excitation with a 445 nm laser for TiO_2/Ru (green), $\text{CsPbBr}_3/\text{TiO}_2$ (blue), $\text{CsPbBr}_3/\text{TiO}_2/\text{Ru}$ (red); (b) Absorbance spectra of photocatalytic reaction mixture before (blue) and during laser excitation (red), where (c) depicts absorption intensities extracted during photocatalysis at 460 nm (black) and 515 nm (green) accordingly.

Simultaneously with hydrogen evolution studies, the optical absorption of the reaction mixture was monitored by UV-Vis spectroscopy (Figure 21b). Prior to photoexcitation the absorption spectrum was predominated by the absorption of CsPbBr_3 semiconductor (blue curve). As soon as the laser was switched on, a negative signal appeared, assigned to the emission of photo-excited CsPbBr_3 nanocrystals. As seen from the graph, the intensity of this negative signal was unchanged through the entire photocatalytic experiment, suggesting that perovskite nanocrystals did not degrade during photocatalysis. After switching off the illumination, the complete system ($\text{CsPbBr}_3/\text{TiO}_2/\text{Ru}$) had no pronounced signs of degradation (Figure 21c).

5.3.3. Magneto-Photoluminescence Studies

It was decided to perform time resolved electron dynamics studies within CsPbBr_3 to understand the low performance of this material in HER and study the possibility to improve it. High non-radiative recombination was recognized as a key factor of low performance in solar cells. Zhang *et.al.* revealed

that photoluminescence of parent organic-inorganic perovskites, $\text{CH}_3\text{NH}_3\text{PbI}_3$, was affected by the magnetic field.¹⁵⁷ Exposure to a magnetic field does not affect optical absorption simply, but decreases the amount of antiparallel spin states, which overall resulted in the reduction of lead halide perovskite photoluminescence. The observed decrease of the PL signal in the magnetic field correlated with the desired increase of observed photocurrent, suggesting directly that both electron-hole recombination and dissociation were spin-dependent processes.¹⁵⁸ In this chapter, we have decided to investigate the effect of the magnetic field on photoluminescence properties of fully inorganic perovskites.

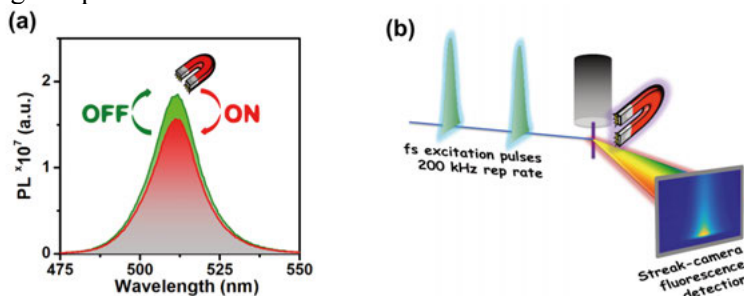


Figure 22. (a) Steady-state emission spectra of CsPbBr_3 with and without applied magnetic field (0.5 T) at 0 °C. (b) Scheme of magnetophotoluminescence measurements for CsPbBr_3 delivered by microliquid jet under excitation with femtosecond laser pulses with streak camera detection

Under steady-state conditions, we observed 10-15% decrease of PL intensity for CsPbBr_3 at 0°C in the magnetic field of 500 mT (Figure 22a). Generally, this may be caused by a decrease in a concentration of emitters or an increase of their radiation rate.¹⁵⁹ In order to understand the origin of this magnetophotoluminescence effect, we have performed a set of time-resolved measurements including TRPL and TIRAS.

Time-resolved magneto-photoluminescence studies were performed with the help of a streak camera that enabled both fine resolutions in time and energy. A magnetic field was applied using an electromagnet with a remote control (50 mT). A microliquid jet provided (Figure 22b) constant delivery of fresh cooled sample (0 °C), preventing overexcitation and damage of the CsPbBr_3 sample.⁹⁹ No additional sacrificial agents were used during time-resolved studies. Figure 23 (a, c) display two contour maps obtained for CsPbBr_3 with and without the applied magnetic field.

Table 3. Lifetimes extracted from magnetophotoluminescence measurements.

Power (mW·cm ⁻²)	Magnet OFF		Magnet ON	
	Fast decay (ps)	Slow decay (ps)	Fast decay (ps)	Slow decay (ps)
198	138±9 (55 %)	1038±65 (45 %)	104±6 (63 %)	959±55 (37 %)
305	138±8 (55 %)	1031±31 (45 %)	100±4 (64 %)	886±25 (36 %)
450	131±95 (57 %)	1000±34 (43 %)	101±5 (65 %)	892±23 (35 %)

At the first glance, it is clear that both line broadening and faster kinetics were observed in the magnetic field (Figure 23 b,d). The extracted kinetic traces at the emission maximum (515 nm) were fitted with a biexponential function giving two lifetime components – ~ 100 ps (fast), and ~ 1000 ps (slow). The resulted lifetime values are compiled in Table 3 as averaged values of a series of eight consecutive Magnet “ON/OFF” cycles.

As low photoexcitation intensity may preclude the observation of magneto-photoluminescence effect,¹⁵⁸ the measurements were performed under three different laser fluencies $\sim 200, 300, 450$ mW/cm². In all cases, the magnetic field caused two outcomes: it diminished both radiative recombination lifetimes, and increased the contribution of the fast component fraction (Table 3). The magnetic field primarily affects the distribution of both anti-parallel and parallel spin states of excitons, increasing the fraction of electron and holes with parallel spin states. Accordingly, the observed increase of the fast component fraction with the applied magnetic field corresponds to a formation of charges with parallel spin states. It was previously observed that the magnetic field ($B = 0\text{--}4\text{T}$)^{160,161} caused the broadening of the FWHM of the PL signal due to strong spin-orbital coupling in combination with crystal-line distortion inside CsPbBr₃ nanocrystals, which further caused splitting between singlet and triplet states (Rashba effect).

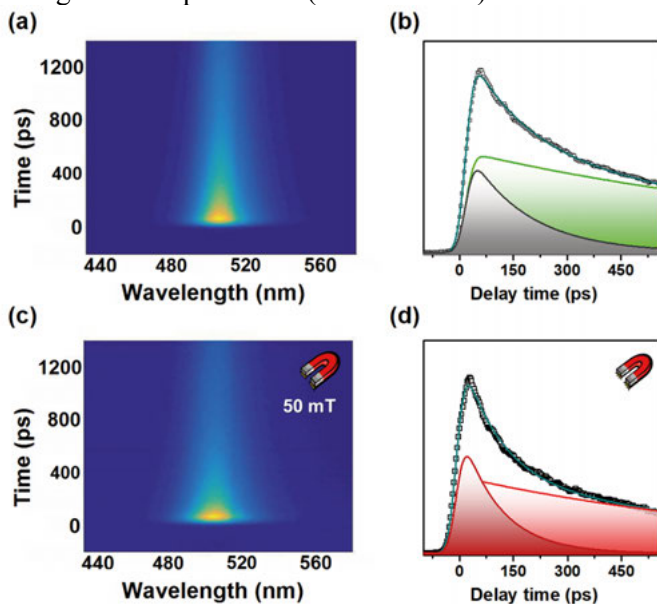


Figure 23. Contour plots of TRPL without (a) and with (c) applied magnetic field (50 mT); The kinetic traces extracted at the emission maximum (515 nm) without (b) and with (d) applied magnetic field (50 mT).

Taking all into account, the response of the CsPbBr₃ NCs to the magnetic field indicated that the observed decrease of photoluminescence was caused by faster recombination of electrons and holes with parallel spin states, which

fraction has increased in the magnetic field, rather than a decrease of emitters as suggested by Zhang *et.al.* Due to faster recombination of electron and holes in the magnetic field, as well as increase of the portion of fast decaying electrons, its application was found to be disadvantageous tool effecting charge separation. Hence, further studies were performed without magnetic field.

Time-resolved photoluminescence measurements have provided us with information about the radiative processes observed for CsPbBr₃. In order to understand the overall electron dynamics upon light absorption, it was decided to perform transient mid-infrared absorption spectroscopy studies, where the mid-infrared probe is sensitive to free electrons in the CB. The kinetic trace was extracted at 1851 cm⁻¹ from the TIRAS data upon band gap excitation of CsPbBr₃ (Figure 24a). The decay was fitted with three components – 21 ps (32 %), 121 ps (44 %), and 970 ps (24 %). The lifetime of the two slower component is similar to the lifetime determined from TRPL measurements (for radiative processes). However, the fast 21 ps component was not previously observed in TRPL, and appeared most likely due to nonradiative processes (note Q.Y. = 80 %). The rising edge was fitted with a monoexponential function resulting in a lifetime of 268 fs. This was assigned to the time required to break apart the electron-hole pair and inject the electron into the conduction band of semiconductor.

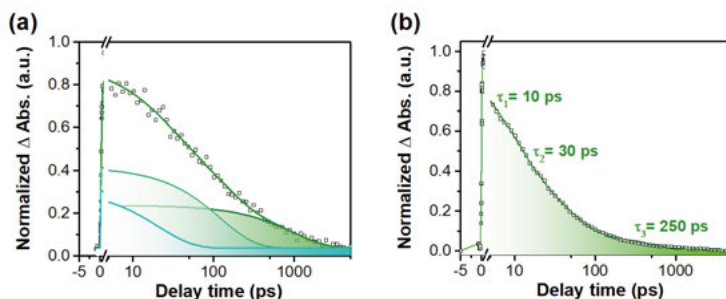


Figure 24. The kinetic trace extracted from TIRAS measurements at 1851 cm⁻¹ for CsPbBr₃ (a), and at 2000 cm⁻¹ for CsPbBr₃/TiO₂/Ru (b) upon excitation at 400 nm.

Ultrafast transient mid-infrared absorption spectroscopy was also used to monitor the electron transfer from photoexcited CsPbBr₃ to the ruthenium catalyst supported on TiO₂. Figure 24b depicts the kinetic trace extracted at 2000 cm⁻¹ for systems CsPbBr₃/TiO₂/Ru. Rising edge was fitted with a monoexponential function with the lifetime of 250 fs, similar to the bare CsPbBr₃ sample. Once the ruthenium catalyst was supported onto the TiO₂, faster recombination of photogenerated charges was detected for the decay part. The decay was fitted with an exponential function with three components. The slowest component decreased from 450 ps (for CsPbBr₃/TiO₂) to 250 ps (CsPbBr₃/TiO₂/Ru), which was assigned to electron transfer from CsPbBr₃ to the Ru NPs catalyst.

5.3.4. Summary and Outlook

Finally, we conclude that the CsPbBr₃/TiO₂/Ru system is able to generate hydrogen with $\eta_{\text{PTH}} = 0.4 \pm 0.1\%$, in the presence of controlled quantities of sacrificial electron and proton donors.

Upon laser excitation, CsPbBr₃ absorbs light and generates excitons that further dissociate to electron-hole pairs. TIRAS studies revealed that photo-generated electrons in the CB of CsPbBr₃ might be then extracted by the ruthenium nanoparticles present in the colloidal solution of CsPbBr₃/TiO₂/Ru system with the ulterior transfer to the ruthenium catalyst that converted protons to hydrogen. The sacrificial quenching of the holes in the VB left after electrons extraction from CsPbBr₃ was performed by triethylamine.

The effect of magnetic field on non-radiative recombination was studied with the help of time-resolved photoluminescence. Under the magnetic field the population of antiparallel states was suppressed, while the population of parallel states increased, causing faster recombination and overall decrease of the photoluminescence signal; hence, leading to the undesirable increase in non-radiative recombination. This suggests that other strategies than application of the magnetic field need to be applied to prolong the charge separated state lifetime and decrease non-radiative recombination. Moreover, it is preferable to use environmental-friendly and non-heavy metal semiconductors as visible light harvesters.

6. Light Trapping with Plasmonic Nanoparticles

6.1. Aim of the Study

This chapter is dedicated to light harvesting with coinage metals (Ag, Cu) nanoparticles that exhibit LSPR in the entire visible region.¹⁶² Tuning their shape and size modifies the metals nanoparticles optical properties. In contrast to molecular dyes, nanoparticles possess five orders of magnitude higher absorption cross-section.¹⁶³ The most advantageous feature of metal nanoparticles is the ability to excite more than one electron per photon per particle. In contrast to semiconductor photocatalysts, which reaction rates and quantum efficiencies tend to decline upon increased light intensity (or temperature), the plasmonic photocatalysts showed indeed better reaction rates at higher photon fluxes enabling quantification and extraction of multiple redox equivalents.¹⁶⁴ As Au nanoparticles have been studied extensively, low-cost Ag and Cu nanoparticles with unique properties attracts our attention.

Both Cu and Ag nanoparticles have high electrical and thermal conductivity, as well as large extinction cross-sections. On the one side, Ag NPs possess the strongest surface plasmon resonance (highest quality factor) in the wider range of wavelengths (300–1200 nm),¹⁶⁵ while Cu NPs possess relatively strong LSPR mainly at higher wavelengths.¹⁶⁶ On the other hand, Cu is the cheapest among coinage metals. Theoretical calculations predicted that Ag nanoparticles are capable of generating hot electrons and hot holes with approximately equal energy distribution, while Cu nanoparticles tend to generate hot holes with 1-2 eV higher energy in magnitude in reference to the Fermi level than the corresponding photogenerated electrons.¹⁶⁷⁻¹⁶⁸ Both light absorbers (Ag NPs and Cu NPs) were investigated in catalytic hydrogen evolution.

6.2. Ag Nanoparticles (Paper V)

6.2.1. Sample Characterization

There are two main groups of methods for the synthesis of metal nanoparticles, namely top-down and bottom-up procedures. The latter require three main components: a metal precursor, reducing agent, and capping agent. The

functions of all these components are described in detail in ref. 165. In chapter 2.3 we presented that size, shape and composition of the nanoparticles strongly dictate the mechanism of light harvesting, whereas for efficient generation of hot electron-hole pairs with energies above the Schottky barrier many factors need to be considered (e.g size <50 nm).⁹⁵ In order to have a high control over the synthesis, it was decided to prepare silver nanoparticles in an automated microfluidic reactor. At first, the metal precursor (AgNO_3) and dual-function betanin (acted as capping and reducing agent), were properly mixed in the micromixer chip. Afterwards, the mixture was injected into a microfluidic reactor under controlled reaction conditions (pH, T). The optimization of the synthetic procedure, as well as control over physical properties of produced nanoparticles (absorption and size distribution) were performed with the help of a genetic algorithm.¹⁶⁹ Finally, spherical silver nanoparticles with the absorption maximum at $\lambda = 405$ nm and narrow size distribution (28-30 nm) were synthesized (Figure 25).

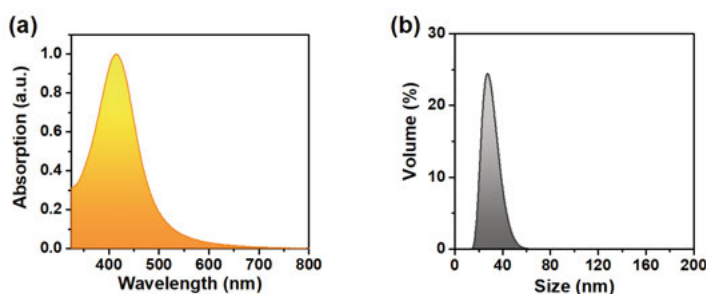


Figure 25. (a) Absorption spectrum and (b) Particle size distribution derived from dynamic light scattering data for Ag nanoparticles.

The characteristic advantage of silver nanoparticles – strong LSPR in a wide range of wavelengths – does however create some obstacles to its use,¹⁶⁵ namely it produces short-lived photogenerated hot electrons. In this case, addition of an electron relay should be used to prolong the lifetime of electrons.

As shown previously in chapters 4 and 5, the electronic coupling between light absorber and electron relay is also essential, thus it was decided to promote electron transfer from Ag NPs to TiO_2 (electron relay) via an addition of molecular linker – *p*-aminobenzoic acid (p-ABA), which connects the two parts and shuttles electrons between them.

Anchoring of p-ABA to the surface of Ag NPs was monitored by the combination of IR and Raman spectroscopy. Even though the interpretation was intricate due to the complicity of the capping agent around Ag NPs, addition of the p-ABA to the solution of Ag NPs lead to the appearance of a peak from the anchored secondary amine band ($\sim 1605 \text{ cm}^{-1}$), and an extra broad peak from the aromatic ring.

6.2.2. Electron Dynamics Studies

To start with, silver nanoparticles were excited at the LSPR maximum ~ 405 nm. The mechanism of electron transfer via a linker to the CB of a semiconductor was studied with TIRAS with the probe in the mid-infrared range. Excitation of AgNPs/p-ABA/TiO₂ induces a broad absorption within the entire measured IR range, ascribed to the injection of hot electrons to the CB of TiO₂. The rising edge of the kinetic trace extracted at 2081 cm⁻¹, was fitted with a single exponential growth function with the lifetime of ~ 600 fs. This corresponds to time required for the hot electrons to be injected via the conjugated linker to TiO₂. The decay of the kinetic trace at 2081 cm⁻¹ was fitted as a sum of two exponential decay functions with 5 ps (93%, fast) and 80 ps (7%, slow) components (Figure 26a). After 5 ns (delay line) more than 30% of the intensity of initial signal was preserved, suggesting that electrons in the conduction band of TiO₂ may be further utilized in the catalytic hydrogen evolution reaction. For a reference measurement, the linker (p-ABA) was removed, however the electron injection could still be observed in the AgNPs/TiO₂ system. This can be a result of Ag NPs anchoring via the carboxylic groups of the capping agent (betanin and the derivatives of its basic hydrolysis during manufacturing) to the semiconductor. The kinetic trace extracted at 2081 cm⁻¹ for AgNPs/TiO₂ revealed that the injection time was unaffected. At the same time, the decay was fitted with 9 ps (82 %) and 0.6 ns (18 %) components.

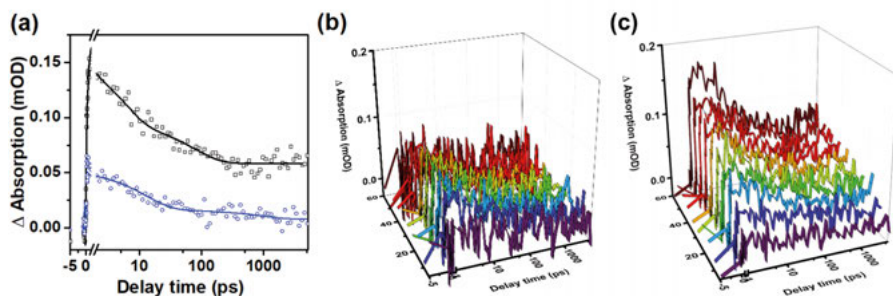


Figure 26. (a) Kinetics extracted from TIRAS data at 2081 cm⁻¹ for AgNPs/p-ABA/TiO₂ (black) and AgNPs/TiO₂ (blue). (b-c) Evolution of the kinetic trace extracted at 2081 cm⁻¹ for AgNPs/TiO₂ (b) and AgNPs/p-ABA/TiO₂ (c).

The intensity of the signal for the AgNPs/p-ABA/TiO₂ system was three times higher than that for AgNPs/TiO₂, demonstrating that a more effective electron transfer occurred in the presence of p-ABA. Much faster dynamics after the addition of the linker revealed that it promoted both undesired back-electron transfer in parallel to desired forward electron transfer. The analysis of TIRAS data revealed that the intensity of the signal for the AgNPs/TiO₂ system without linker remained unchanged over 60 min (Figure 26b). In con-

trast, addition of the p-ABA linker leads to a progressive increase of the signal intensity until it reaches a plateau in about 90 min, assigned to self-assembling of the linked AgNPs|p-ABA/TiO₂ system (Figure 26c).

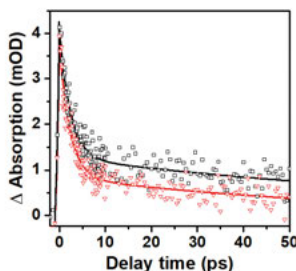


Figure 27. Kinetic trace extracted from TAS data at 795 nm for AgNPs|p-ABA/TiO₂ (black) and AgNPs|p-ABA/TiO₂/Ru (red).

Finally, once harvesting of hot electrons was achieved with the TiO₂ connected via molecular linker to Ag NPs, it was decided to study the possibility of further electron transfer towards a hydrogen evolution catalyst. Ultrafast transient absorption spectroscopy was performed for two systems - AgNPs|p-ABA/TiO₂ and AgNPs|p-ABA/TiO₂/Ru (Figure 27). After the excitation of the samples at the LSPR maximum ($\lambda_{\text{exc.}} = 405 \text{ nm}$), the kinetic traces were extracted at 795 nm.¹⁷⁰ The rising edge was fitted with single exponential function with a lifetime of $\sim 800 \text{ fs}$. This is about 200 fs slower than the rising edge determined from TIRAS data, suggesting that the electrons injected into the TiO₂ CB are filling surface traps states. The decay part of the kinetic trace at 795 nm was fitted with the biexponential decay function. The corresponding lifetimes for AgNPs|p-ABA/TiO₂ were similar to those determined from TAS – 2.6 ps (65 %) and 92 ps (35 %). Addition of Ru NPs caused faster recombination of the signal that was monitored by the increase of contribution of a fast component fraction by 10 % and decrease of the longer component fraction. The obtained lifetimes for the AgNPs|p-ABA/TiO₂/Ru were accordingly 2.6 ps (75 %) and 67 ps (25 %). All of these suggest that photogenerated hot electrons can be both transferred via a molecular linker to the semiconductor and be further driven towards the hydrogen evolution catalyst.

6.2.3. Photocatalysis

Charges extracted from the assembled system AgNPs|p-ABA/TiO₂/Ru after excitation were studied in both hydrogen evolution reaction and methylene blue oxidation. The energetic scheme of this process is depicted in Figure 28. Note that no extra sacrificial electron donor was used in this system, as the idea was to utilize hot holes created by the LSPR excitation of Ag NPs in the reversible oxidation of methylene blue that is a known water contaminant.

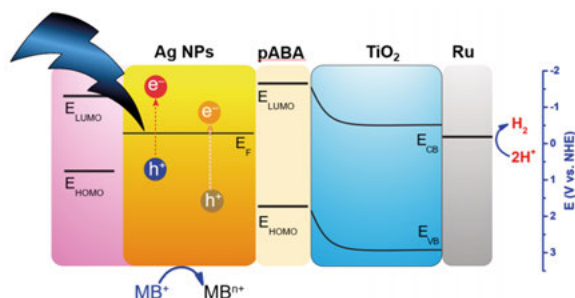


Figure 28. Energy diagram for H₂ evolution with AgNPs/p-ABA/TiO₂/Ru system.

Firstly, the HER was examined, where photocatalytic tests were performed in a flow photoreactor with mass spectrometry detection of gaseous products, and the obtained data are depicted in Figure 29. Addition of the molecular linker (p-ABA) to AgNPs/TiO₂/Ru resulted in increase of both rate and quantity of generated hydrogen. This agrees well with the TAS data, where we observed more efficient electron transfer from photoexcited Ag NPs to the semiconductor once they were linked by p-ABA. At the same time, AgNPs/Ru without an electron relay were unable to generate H₂. Moreover, no hydrogen was detected for the AgNPs/p-ABA/TiO₂, p-ABA/TiO₂/Ru systems, indicating that all components are necessary to make the functioning system.

Additionally, the AgNPs/p-ABA/TiO₂/Ru system was studied in the reaction of the methylene blue oxidation with the help of UV-Vis spectroscopy in parallel to HER studies (Figure 29b). The more abrupt decrease of the methylene blue signal assigned to its oxidation, was detected for the system where the light absorber and electron relay were connected by the molecular linker. Once the Ru NPs deposited on TiO₂ were removed from the system AgNPs/p-ABA no methylene blue oxidation was detected, indicating that only once hot electrons are extracted, hot holes may be used in oxidation reaction. Otherwise, the recombination of hot electron with hot holes becomes more efficient.

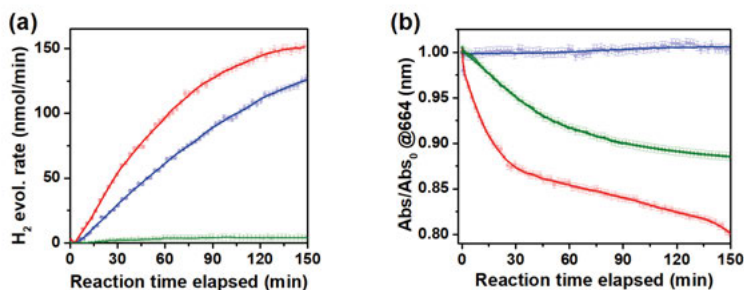


Figure 29. Hydrogen evolution (a) and methylene blue oxidation data (b) for AgNPs/p-ABA/TiO₂/Ru (red), AgNPs/TiO₂/Ru (blue) and Ag-PVP NPs/p-ABA/TiO₂/Ru (green).

The role of the capping agent around Ag NPs was also investigated by making the particles via the classic polyol method, which resulted in Ag NPs decorated with polyvinylpyrrolidone (Ag-PVP). The Ag-PVP NPs had similar properties (size, shape and optical absorption). The activity of these nanoparticles was studied in the HER and methylene blue oxidation reactions respectively. H₂ evolution curves revealed that Ag-PVP NPs|p-ABA|TiO₂|Ru system generated significantly less hydrogen, indicating that the capping agent played a crucial role. A similar effect was detected in the reaction of the methylene blue oxidation. During photocatalysis with Ag NPs decorated with betanin derivatives, we observed the emission characteristic for products of betanin exposed to basic hydrolysis (e.g., betalamic acid). The estimated lifetime of this emission was 15.8 ps as determined from time-resolved photoluminescence studies. All of this suggests that upon extraction of hot electrons from the Ag NPs, the capping agent (betanin) around its surface donates electrons to fill the hole left behind, thus prolonging the lifetime of the charge separated state by keeping charges even further apart.¹⁷¹ The photon-to-hydrogen quantum yield of the AgNPs|p-ABA|TiO₂|Ru was estimated from the absorbed photon flux that was converted into hydrogen. The resulting η_{PTH} was 19.9%.

6.2.4. Summary and Outlook

To conclude we have developed a nano-hybrid system for hydrogen evolution Ag nanoparticles (decorated by natural pigment) connected via a molecular linker to the semiconductor with co-deposited Ru nanoparticles. The overall photon-to-hydrogen quantum yield reached ~20%. Using ultrafast time-resolved spectroscopy techniques, we have monitored the electron dynamics from the injection of photogenerated hot electrons into TiO₂ until their further transfer towards the ruthenium catalyst. Addition of the molecular linker promoted electron transfer from Ag towards TiO₂ consequently leading to an accumulation of charges on the surface of the semiconductor and further efficient hydrogen evolution. Without the molecular linker, the electron transfer was still observed from Ag to TiO₂, most likely via the capping agent (betanin) that had available anchoring groups. Even though longer lifetimes of the charge separated state was observed for the system without linker, the overall hydrogen evolution was less efficient. The capping agent was found to play a crucial role in charge stabilization. The polyvinylpyrrolidone around the Ag nanoparticles was not involved in charge transfer, thus leading to a low photocatalytic activity. The capping agent betanin reacts with the holes created after the photoexcitation of the silver particle, and causes the photogenerated charges to separate. Moreover, the used approach of assembling the nano-hybrid components, opens the ability to tune the system easily by varying linkers, plasmonic light absorbers, semiconductors and catalysts, thus reaching desired photocatalytic properties.

6.3. Cu Nanoparticles (Paper VI)

6.3.1. Sample Preparation and Characterization

Copper nanoparticles were synthesized in a microfluidic reactor via chemical reduction of the precursor (CuSO_4) by a sodium ascorbate/ascorbic acid (5/95%) solution. For controlled growth of the Cu NPs branched polyethyleneimine was used as a capping agent. The resulting nanoparticles had an absorption maximum centered at 390 nm (Figure 30a). Dynamic light scattering measurements revealed that the mean size of synthesized nanoparticles was ~ 2 nm (Figure 30b).

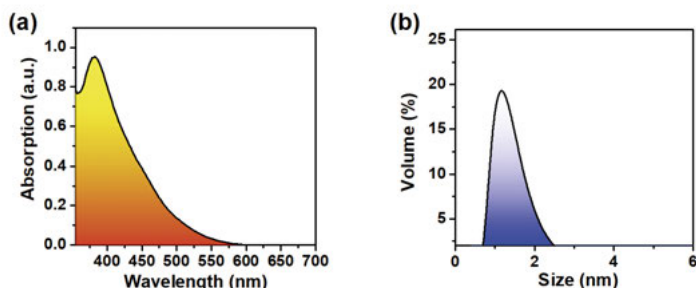


Figure 30. UV-Vis spectrum (a) and DLS volume distribution (b) for Cu NPs.

The major problem during synthesis of Cu NPs might have appeared due to their low oxidation resistivity. To determine the oxidation state of Cu NPs we have used high-resolution X-ray absorption spectroscopy (HR-XAS), and have compared the corresponding pre-edges that depicted the unoccupied states above the Fermi level in Cu ($[\text{Ar}] 4s^1 3d^{10}$) because of sd -hybridization. As seen from the HR-XAS spectra (Figure 31a), the pre-edge for Cu NPs (black) does not match that for the CuO (i.e. Cu^{2+}), however it was not conclusive to distinguish between Cu^0 and Cu^+ .

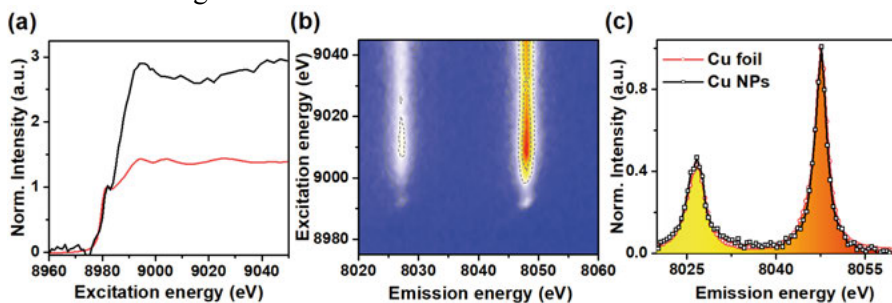


Figure 31. (a) HR-XAS spectra normalized to the pre-edge for Cu NPs (black) and Cu foil (red). (b) RXES for Cu NPs and (c) extracted HR-XES spectra for Cu NPs (black) and Cu foil (red).

To differentiate these two species we performed simultaneously the resonant X-ray emission spectroscopy (RXES, Figure 31b). A 0.13 eV shift in the K_{α} -XES emission peak in respect to the metallic foil is expected if the sample

contains Cu^+ (Cu_2O).¹⁷² Since the measurement of $\text{K}\alpha$ -XES emission for the Cu NPs did not show a shift in respect to the metallic foil (Figure 31c), it was concluded that particles are indeed in the metallic state Cu^0 .

6.3.2. Plasmon dynamics

Before exploring electron harvesting from Cu nanoparticles by the hydrogen evolution catalyst, it was decided to understand the kinetics of the plasmon generated upon laser excitation at the LSPR maximum of the electron gas inside Cu NPs. Pump-probe ultrafast transient absorption spectroscopy was used (pump = 395nm, probe in 350–750 nm), and the corresponding 2D contour map obtained for Cu NPs is depicted in Figure 32a.

The absorption of photons at the LSPR maximum leads to the excitation of the electron gas. The induced electron-electron scattering events generate a non-Fermi distribution of electrons (internal thermalization),¹⁷³ and cause spectral broadening,¹⁷⁴ thus resulting in one negative and two positive absorption signals in the difference spectrum.¹⁷⁵ A negative signal – ground state bleach (GSB) – appeared at the LSPR maximum due to the decrease of the ground state population as the system is excited. As just mentioned, it was expected to detect two positive features in the difference spectrum (induced absorption, IA) from both sides of the GSB signal. However, due to the limitations of the probe (350–750 nm), the positive signal of IA was clearly observed only to the red side from the detected GSB centered at 480 nm.

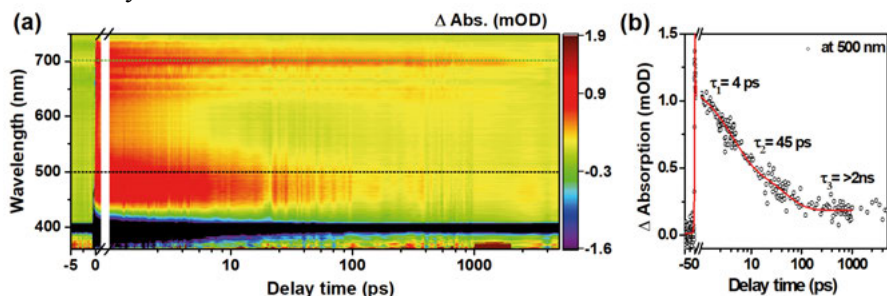


Figure 32. (a) 2D color map of TAS data for Cu NPs upon plasmon excitation at 398nm and (b) extracted kinetic trace at 500nm.

The kinetic trace extracted at 500 nm was fitted as a sum of three exponential decay functions (Figure 32b). As discussed in the chapter 2.3, the excitation of the electrons induced a set of relaxation events, i.e. electron-electron scattering, electron phonon scattering, and phonon-phonon scattering. Two short-lived components with lifetimes of 4 and 45 ps were assigned to electron-phonon scattering and phonon-phonon relaxation respectively, while the one long-lived component (>2 ns) occurred due to phonon-solvent relaxation. The rising edge was fitted as a single exponential function (400 fs), and was

ascribed to the time the system takes to thermalize the hot electrons after several electron-electron collision events.¹⁷⁶

6.3.3. Electron dynamics

The short lifetime of the hot electrons makes the electron relay a necessity. As in case of Ag NPs, TiO₂ was used as the electron relay. The connection between Cu NPs and TiO₂ was established with the help of two ligands, β -Alanine (β -Ala) or *p*-aminobenzoic acid. The linkers ensure that the components are in close proximity, and provide different electron transport capabilities, namely conjugated linker *p*-ABA promotes electron transfer between donor-acceptor components, while β -Ala does not due to its insulating character, though tunneling should not be discarded.

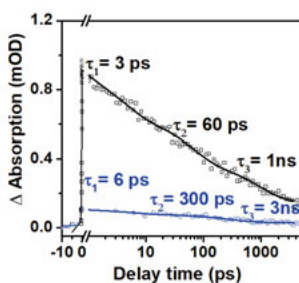


Figure 33. The kinetic traces extracted from TIRAS data at 1950 cm⁻¹ for CuNPs/p-ABA/TiO₂ (black) and CuNPs/β-Ala/TiO₂ (blue).

The electron transfer dynamics from photoexcited Cu NPs to TiO₂ via two linkers was monitored with the help of TIRAS with a probe in the mid-infrared range. Figure 33 depicts kinetic curves extracted at 1950 cm⁻¹ for three systems: TiO₂, CuNPs/β-Ala/TiO₂ and CuNPs/p-ABA/TiO₂. No electron injection to the CB of TiO₂ was detected upon photoexcitation of bare TiO₂. However, for both CuNPs/β-Ala/TiO₂ and CuNPs/p-ABA/TiO₂, excitation of the Cu NPs LSPR lead to electron injection from Cu NPs to the CB of TiO₂ (as seen from the rising edge component ~350 fs). As expected, the conjugated ligand, *p*-ABA, have resulted in much more efficient electron transfer to the semiconductor, as the signal intensity was about ten times higher than that for CuNPs/β-Ala/TiO₂. The kinetic trace for the CuNPs/p-ABA/TiO₂ was fitted with three exponential decay functions (lifetimes: 3 ps, 60 ps and 1 ns). The unconjugated linker, β -alanine, does not provide as good electron coupling as *p*-aminobenzoic acid and simply increases the proximity between CuNPs and TiO₂. Thus, a lower intensity signal was detected for the CuNPs/β-Ala/TiO₂ system. This signal was fitted with a three exponential decay function resulting in the lifetimes: 6 ps, 300 ps, and ~3 ns respectively.

There are two main mechanisms that enable electron transfer from metallic nanoparticles through the linker to the semiconductor, namely direct or

indirect electron transfer. Once the metallic nanoparticle and the semiconductor are in close contact, direct electron transfer was reported to occur within 5–100 fs, while for the indirect transfer 100 fs–10 ps are generally required (see chapter 2.3). We cannot directly distinguish between direct and indirect electron transfer here due to the limitation of our detection system (instrument response function ~ 200 fs), however, the observed times support the idea of an indirect electron transfer mechanism. The faster electron injection for the system interconnected via p-ABA was foreseen due to the promoted electronic coupling between Cu NPs and TiO_2 , while β -Ala just reduces the distance between both parts. However, the fact that electrons were also detected on the sample with β -alanine suggests that other electron transfer mechanism is possible and present.

Before discussing the alternative mechanism, it is worthwhile to estimate the minimum energy that the electron must have to be transferred. At the interface of the metal nanoparticle and the semiconductor the Schottky barrier will be created. The performed DFT calculations revealed that a distance < 3 Å between Cu NPs and TiO_2 , results in the formation of the interface with the profile of an ohmic contact, i.e. there is no formation of Schottky barrier. However, once the distance increases to 3.2 Å, a reasonable Shottky barrier is built (0.69 eV), and once it increases to 4.2 Å, the Schottky barrier of 0.88 eV is formed. In case of β -alanine (~ 4 –5 Å) the observed electron injection from Cu NPs to the conduction band of TiO_2 indicates that hot electrons possess sufficient energy (> 0.88 eV) to overcome the Schottky barrier.

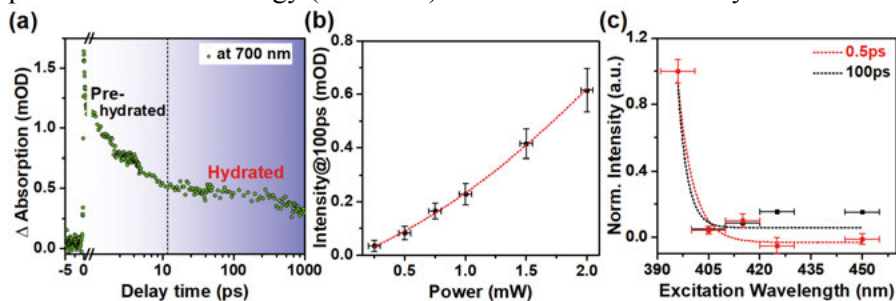


Figure 34. (a) The kinetic trace extracted at 700 nm from TAS data for bare Cu NPs (green). (b) Power dependence of signal intensity (determined at 100ps) of extracted hydrated electrons. (c) Dependence of normalized intensity signal versus excitation wavelength ($\lambda_{\text{exc.}} = 395$ –450 nm) extracted at 700 nm for two regimes: prehydrated and hydrated electrons determined at 0.5 ps and hydrated electrons determined at 100ps.

Small Ag NPs have been shown to be able to generate prehydrated electrons.¹⁷⁷ The prehydrated electron is the state prior to the formation of solvated electrons (hydrated electrons), which are short-lived on the metallic surface ($\lambda_{\text{abs.}} = 650$ –720 nm, they decay completely within 50–70 ps). Careful examination of the 2D map of the TAS data for the bare Cu NPs (Figure 32)

revealed a similar absorption band assigned to prehydrated electrons after excitation of the sample at the LSPR maximum. The extracted kinetic trace at 700 nm for Cu NPs was fitted with biexponential decay functions, showing two regimes with fast component (3 ps, $\sim 70\%$), and slow component ($\sim 30\%$) that did not decay within the measured delay line of 5 ns. The first regime was ascribed to generation of prehydrated electrons, while the long lived signal is related to the fully solvated electrons (hydrated electrons, Figure 34a). The binding energy of hydrated electrons is 3.7 eV that is 1 eV higher than the Fermi energy for the Cu NPs. Having this in mind and the energy of the electron injection determined by DFT calculations, one may suggest that it is plausible that electron transfer from Cu NPs into the conduction band of the TiO₂ semiconductor occurs via hydrated electrons.

Plasmonic nanoparticles are known for their ability to generate multiple energetic electrons per photon absorbed. This was tested upon tuning the power of excitation ($\lambda = 395$ nm) from 0.25–2 W for bare Cu NPs. The non-linear behavior of the signal intensity at 700 nm was observed for the hydrated electrons (Figure 34b) suggesting that Cu NPs are indeed capable of generating multiple energetic electrons. Moreover, excitation wavelength dependent studies revealed ($\lambda_{\text{exc.}} = 395\text{--}450$ nm) that only excitation at the LSPR maximum leads to the formation of both pre-hydrated and long-lived hydrated electrons. The corresponding data extracted in two different regimes for pre-hydrated electrons (0.5 ps) and hydrated electrons (100 ps) is presented in Figure 34c.

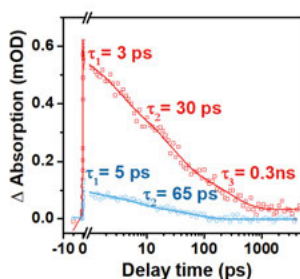


Figure 35. The kinetic traces extracted from TIRAS data for CuNPs/p-ABA/TiO₂/Ru (red), CuNPs/β-Ala/TiO₂/Ru (light blue).

Finally, it was decided to investigate the electron dynamics from TiO₂ to Ru NPs deposited on its surface for both systems: CuNPs/β-Ala/TiO₂/Ru and CuNPs/p-ABA/TiO₂/Ru. Figure 35 depicts the kinetic traces extracted at 1950 cm⁻¹ from TIRAS data with the mid-infrared probe. In both cases, CuNPs/β-Ala/TiO₂/Ru and CuNPs/p-ABA/TiO₂/Ru showed faster dynamics in the presence of a hydrogen evolution catalyst. This indicates that electrons stored in the conduction band of TiO₂ could be harvested by Ru NPs. Detailed

analysis of the decay curves for both systems revealed that components interconnected by β -alanine demonstrated more efficient withdrawal of electrons from the CB of TiO_2 .

6.3.4. Photocatalysis

The two system, $\text{CuNPs}|\beta\text{-Ala}|\text{TiO}_2|\text{Ru}$ and $\text{CuNPs}|\text{p-ABA}|\text{TiO}_2|\text{Ru}$ were tested in the HER reaction with the help of photoreactor connected to mass spectrometer for analysis of the formed gaseous products (Figure 36).

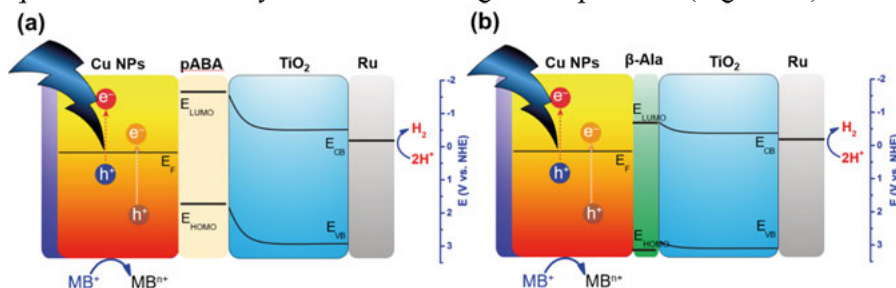


Figure 36. Energy diagrams for two hydrogen evolution systems $\text{CuNPs}|\text{p-ABA}|\text{TiO}_2|\text{Ru}$ and $\text{CuNPs}|\beta\text{-Ala}|\text{TiO}_2|\text{Ru}$.

The photogenerated electrons were supposed to be driven to the Ru NPs to produce hydrogen, while the reactive holes remaining in the Cu NPs were supposed to oxidize the methylene blue. A theoretical model deduced from DFT calculations predicted that photogenerated hot holes in Cu NPs should have higher energies in magnitude than that for hot electrons in respect to the Fermi level. The process of methylene blue oxidation was monitored by the UV-Vis spectroscopy in parallel to the detection of H_2 .

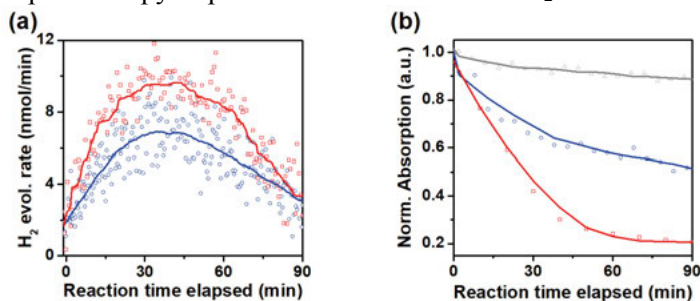


Figure 37. H_2 evolution (a) and methylene blue oxidation data (b) measured upon excitation of Cu NPs at 400 nm for $\text{CuNPs}|\text{p-ABA}|\text{TiO}_2|\text{Ru}$ (red), $\text{CuNPs}|\beta\text{-Ala}|\text{TiO}_2|\text{Ru}$ (blue) and blank (light grey).

Figure 37 depicts hydrogen evolution curves for both $\text{CuNPs}|\beta\text{-Ala}|\text{TiO}_2|\text{Ru}$ and $\text{CuNPs}|\text{p-ABA}|\text{TiO}_2|\text{Ru}$. The excitation of the Cu NPs' LSPR by a 400 nm laser resulted in a directed flow of electrons towards the hydrogen evolution catalyst. In parallel to the TIRAS data, ten times more efficient

electron injection to TiO_2 was detected for CuNPs|p-ABA|TiO_2 , where more efficient hydrogen generation was detected for the system interconnected by p-ABA. However, reasonable amounts of hydrogen were generated for the system interconnected by β -alanine, most likely due to more efficient electron extraction by the Ru catalyst in $\text{CuNPs|}\beta\text{-Ala|TiO}_2\text{|Ru}$ system, than for $\text{CuNPs|p-ABA|TiO}_2\text{|Ru}$.

Alongside to hydrogen evolution, the decrease of methylene blue absorption peak at 665 nm was monitored by the UV-Vis spectroscopy. Thus, the reactive holes left behind after excitation of Cu NPs had sufficient energy to oxidize the methylene blue. A reference system without Cu NPs or proton reduction catalyst did not produce any hydrogen, and minimal changes to the methylene blue absorption was detected (Figure 37b).

6.3.5. Summary and Outlook

Cu nanoparticles (2 nm) decorated with polyethylenamine have been synthesized in the microfluidic reactor. Even though copper nanoparticles usually tend to oxidize easily, it was shown that the oxidation state of the copper nanoparticles was zero by high-resolution X-ray absorption spectroscopy and the resonant X-ray emission spectroscopy. Relaxation of the photoexcited plasmon upon light absorption by Cu NPs was studied using ultrafast transient absorption spectroscopy. For prolonging the lifetime of photogenerated charges, Cu NPs were connected to the semiconductor via either β -alanine or *p*-aminobenzoic acid. In both cases, electron injection into TiO_2 leads to the accumulation of electrons in the conduction band of semiconductor that was monitored by TIRAS. *p*-aminobenzoic acid provided better conductivity between Cu NPs and TiO_2 that enhanced signal intensity ten times in respect to a system interconnected by β -alanine. Theoretical calculations revealed that hot electrons that overcame the Schottky barrier for the $\text{CuNPs|}\beta\text{-Ala|TiO}_2$ system should have at least 0.88 eV energy. We suggested that the mechanism of electron transfer from Cu NPs to TiO_2 via β -alanine occurred via the hydrated electrons that were generated only if Cu NPs were excited at the LSPR maximum. The addition of Ru nanoparticles leads to removal of electrons from the conduction band of the semiconductor towards the catalyst. In the end, the hydrogen evolution was observed for two nano-hybrid systems $\text{CuNPs|}\beta\text{-Ala|TiO}_2\text{|Ru}$ and $\text{CuNPs|p-ABA|TiO}_2\text{|Ru}$. Hot holes left after the extraction of hot electrons towards the hydrogen evolution catalyst upon light absorption participated in oxidation of methylene blue.

7. Conclusions

A substantial motivation behind renewable energy research and development is the ever-growing world's demand for energy, which is seen as a vital component of our everyday life. Additionally, climate change effects driven by the emission of greenhouse gases associated to the fossil fuels burning has risen to prominence over the last decades. Solar energy is widely available and abundant (power that is constantly reaching the earth 120,000 TW), making it a clear frontrunner in the energy sector. Moreover, the solar power energy offers a new concept for building a sustainable society, where each of us contributes to its production. Many countries worldwide are already applying technologies for sunlight conversion to electricity. Currently the development of the renewable energy sector seeks investments, where subsidies allow this branch to be price-competitive. Long-term solution of the energy crisis requires flexible technologies capable of manufacturing not only electricity, but also fuels from endless, low-cost resources, e.g. water. Chemical fuels offer the possibility to manufacture valuable belongings.

Photochemical energy conversion into a solar fuel includes light absorption, charge separation and catalytic process. Nature has taught us that effective accumulation and charge separation are the key steps in sunlight conversion. **In chapter 1.3**, I presented the main factors that may lead to accumulative charge separation, enhancing the overall transformation of light to fuel. Among the discussed factors are the ability to accumulate electrons, which are generated upon one photon absorption, the ability to generate a long-lived charge separated states, the fast rates of forward reaction and the slow rates of side reactions as well as the ability to accumulate several redox equivalents before catalysis.

In chapter 4, I investigated the light harvesting with a natural dye capable of generating two electrons upon one photon absorption, and the possibility of extraction of those electrons by the molecular electron relay. The purification of the natural dye betanin caused the encouraging decrease of the fast component fraction. However, it was impossible to extract electrons from the short-lived excited state of betanin by the methylviologen. In addition, the formation of a doubly reduced product was hindered by the overlap with the excited state absorption of betanin, and the only evidence of its possible formation was gained from the electrochemistry studies of the B1MV system (30 mV/pH shift of E_{pa}^2). All in all no hydrogen evolution was detected for the system with the purified betanin sample as a light harvester.

In Chapter 5, I discussed the extraction of electrons from the short-lived excited state of betanin into the CB of the semiconductor by anchoring the betanin to the surface of ZnO-OEG. Unique properties of ZnO-OEG has enabled harvesting of electrons from betanin, leading to the generation of a long-lived charge separated state and extending the lifetime of electrons inside the CB of the semiconductor to $\sim \mu\text{s}$ -s time range. Linking of the FeFe-hydrogenase active site mimic catalyst, namely $[\text{FeFe}(\text{mcbdt})(\text{CO})_6]$, allowed further extraction of accumulated electrons from the CB of ZnO-OEG for the reduction of protons to hydrogen. The hydrogen evolution studies revealed that in 4 h $\sim 980 \mu\text{mol}$ of hydrogen was evolved.

In the second part of chapter 5, I have exchanged the light absorber betanin by the semiconductor itself capable of the visible light harvesting, namely CsPbBr_3 . Additionally, I have exchanged the molecular catalyst to the ruthenium nanoparticles supported on TiO_2 . The developed system turned to be capable of hydrogen evolution with the photon-to-hydrogen quantum yield of 0.4 %. I also tried to suppress the non-radiative recombination by applying the magnetic field. In return, the magnetic field caused undesired faster radiative recombination and overall decrease of photoluminescence, thus suggesting that other strategies should be used for the better performance of the system. In addition, usage of the environmental-friendly and non-heavy metal semiconductors is beneficial.

In chapter 6, I decided to use coinage metal nanoparticles as the light harvesters, which in contrast to semiconductors are capable of direct generation of multiple electrons per photon absorbed. The developed procedures for synthesis of the nanoparticles in the microfluidic reactor provided the control over preparation and properties of produced nanoparticles.

The Ag NPs has the strongest surface plasmon resonances in the wide range of wavelength upon light absorption that has the ability to generate hot electrons and hot holes with equal energy distribution. This feature of Ag NPs was used for utilization of hot electrons in proton reduction, and utilization of hot holes in the methylene blue oxidation. The electron dynamics from the process of injection of photogenerated charges into the CB of TiO_2 until the process of electron transfer towards catalyst were studied in detail. The molecular linker between the light harvester and the semiconductor was shown to promote the electron transfer and lead to higher efficiencies of hydrogen evolution compared to the unconnected system. Additional charge stabilization was achieved due to the capping agent around the Ag NPs. A photon-to-hydrogen quantum yield of ca. $\sim 20 \%$ was reached.

In the second part of chapter 6, I have exchanged the Ag NPs by Cu NPs that have the ability to generate hot holes with energies that are $\sim 1\text{--}2 \text{ eV}$ higher than the energy of corresponding electrons. The oxidation state of the metallic Cu NPs was determined with the help of HR-XAS and RXES. The dynamics of the plasmon relaxation was studied in detail. Two molecular

linkers were used to connect the light harvester (Cu NPs) and the semiconductor (TiO_2), namely β -alanine or p-aminobenzoic acid. The conjugated linker, p-ABA, has caused more efficient electron transfer from the excited Cu NPs into the CB of the semiconductor. The other linker, β -Ala, has brought metal nanoparticles and semiconductor in close proximity to one another, allowing hot electrons with at least 0.88 eV energy to overcome the Schottky barrier. The mechanism of electron transfer for the $\text{CuNPs}|\beta\text{-Ala}|\text{TiO}_2|\text{Ru}$ was proposed to occur via the generation of hydrated electrons. The deviation from linearity of the power dependence studies suggested that Cu NPs are indeed capable of multiple-electrons generation. Comparison of the photocatalytic studies revealed that the $\text{CuNPs}|\text{p-ABA}|\text{TiO}_2|\text{Ru}$ system is more efficient in both proton reduction and methylene blue oxidation than the $\text{CuNPs}|\beta\text{-Ala}|\text{TiO}_2|\text{Ru}$ system.

Analysis of photocatalytic studies for the systems based on Ag and Cu NPs revealed that Ag NPs are more efficient in proton reduction, while Cu NPs are more efficient in methylene blue oxidation. Most likely, this observation is caused by the ability of Ag NPs to generate more energetic electrons, while Cu NPs seem to have holes that are more reactive.

In the course of this thesis, I was trying to reach accumulative charge separation with pure molecular systems and systems based on nanoparticles. *The hybrid systems* assembled by the combination of the advantageous properties of molecules, semiconductors, and metal nanoparticles turned to show the highest activity in the photochemical hydrogen production. Metal nanoparticles were effective light harvesters with the absorption cross-section five orders of magnitude higher than that for dyes. Moreover, metal NPs showed the ability to generate more than one electron per photon absorbed. The molecular linkers provided control and flexibility in tuning the connection between the light absorber and the electron relay. It was shown that by adjusting the electronic properties of the molecular linker, one may promote electron transfer. Semiconductor nanoparticles offered the desired charge separation properties via prolonging the lifetime sufficiently long to perform photocatalysis.

The detailed investigation and development of the hybrid systems is important for the progress in solar fuel production. For example, in order to improve the efficiency of the created hybrid system, it would be beneficial to utilize the photogenerated hot holes in oxidation of chemicals to high energetic value products. This would make the process potentially more versatile and economically more attractive.

8. Populärvetenskaplig Sammanfattning (Summary in Swedish)

En viktig motivation för forskning mot förnybara energikällor är världens ständigt växande energibehov. Dessutom kommer klimatförändringarna som orsakas av växthusgasutsläpp, vara en stor utmaning de kommande åren. Överflödet av solenergin som når jorden (120 000 TW per år) skulle kunna möta det globala behovet. Därtill erbjuder solenergin ett nytt koncept för att bilda ett hållbart samhälle där alla skulle bidra. I många länder tillämpas det redan teknologier som omvandlar solenergi till ström. För närvarande söker den förnybara energisektorn efter investeringar, medan subventioner leder till att branchen blir konkurrenskraftig. För en långsiktig lösning av energikrisen behövs flexibla teknologier som inte bara producerar energi utan också bränslen från icke-sinande, billiga resurser, t.ex. vatten. Kemiska bränslen innehåller en stor energitäthet för energilagring och dessutom möjligheten att producera högvärdiga produkter.

Fotokemisk energiomvandling i solbränslen kräver tre steg: upptagning av (sol)ljus, laddningsseparation och katalytisk omvandling av substratet till den högvärdiga produkten. Naturen har lärt oss effektiv generering och ackumulering av laddningar som är ett nyckelmoment i omvandlingen av soljuset. I kapitel 1.3 presenterar jag de huvudaspekter som skulle kunna leda till laddningsackumulering vilket förbättrar den övergripande omvandling från solljus till bränsle. Bland de diskuterade aspekterna finns förmågan att generera flera laddningar efter upptagning av en enda foton och att generera långlivade laddningar. Det sistnämnda erhålls genom att underlätta de önskade framåtreaktioner medan de oönskade sido- och bakåtreaktioner hämmas. Detta är framförallt viktigt då det behövs flera laddningar för att genomgå den katalytiska reaktionen.

I kapitel 4 undersökte jag ett naturligt färgämne (betanin, som förekommer bl.a. i rödbeta) som kan ge ifrån sig två elektroner efter att ha absorberat en foton. Därtill studerades hur desds elektroner kan extraheras och vidaretransporteras med hjälp av metylviologen. Jag kunde visa att rening av färgämnet förlängde dess livslängd i det exciterade tillståndet efter solljusupptagningen. Det var däremot inte möjligt att extrahera elektronerna.

I kapitel 5 ersattes den molekylära elektronacceptorn metylviologen mot en halvledare (ZnO). Betanin länkades till halvledarytan vilket möjliggjorde en elektronöverföring från betanin till halvledaren. Bakreaktionen skedde

ovanligt långsam (på μs till s tidskalan). På ytan länkades också en naturinspirerad järnkatalysator ämnat att producera vätgars. Den långa livslängden av elektronerna i halvledaren ledde till att systemet verkligen kunde reducera protoner till vätgas med hjälp av solljuset.

I andra delen av kapitlet ersattes färgämnet (betanin) och ZnO mot en annan färgad halvledare, Cs PbBr_3 vilket är en så kallad perovskit. Dessutom användes rutenium nanopartiklar på TiO_2 som katalysator istället för den naturinspirerade järnkatalysatorn innan. Detta system visade sig vara kapabel att producera vätgas med en solljus-till-vätgas effektivitet av 0.4 %. Jag testade också hur systemet påverkas av ett externt magnetfält. Det visade sig dock att detta leder till ökad fotoluminescens vilket i sin tur minskade/hindrade vätgasproduktionen. Därför behövs det andra strategier för att öka vätgasproduktionen i dessa system.

I kapitel 6 bestämdes att använda nanopartiklar gjorda av myntmetaller för att absorbera ljus. Dessa har till skillnad från halvledare förmågan att direkt generera flera laddningar per absorberad foton. Vi utvecklade och optimerade metoder för deras syntes med hjälp av en mikrofluidreaktor vilket gav oss möjligheten att kontrollera de fysikaliska och kemiska egenskaperna hos de producerade nanopartiklarna.

Silvern nanopartiklar som har en bra förmåga att absorbera ljus över stora delar av solspektrumet kan generera energirika elektroner och hål (positiva laddningar). De energirika elektronerna används för vätgasproduktion, medan de energirika hålen oxiderar metylblått. Vi studerade elektronöverföringsprocesserna från nanopartikeln via TiO_2 till den vätgasproducerande katalysatorn. Vi använde en molekylär länk mellan nanopartiklarna och TiO_2 vilket ökade effektiviteten av elektronöverföringen och slutligen resulterade i högre vätgasproduktion.

I andra delen av kapitel 6 har jag bytt ut silvern nanopartiklarna mot koppar nanopartiklar. Dessa genererar också energirika laddningar med skillnaden att hålen har mer överskottsenergi än elektronerna. Två olika molekylära länkar undersöktes, varav en var konjugerad. Den konjugerade länken visade den effektivare elektronöverföringen. Den icke-konjugerade och kortare länken ledde till att de energirika elektronerna kunde överföras till halvledaren innan de gav ifrån sig överskottsenergin. Det kunde även visas att nanopartiklarna producerades fler än en elektron per absorberad foton. Fotokatalytiska mätningar visade att systemet med den konjugerade länken visade både bättre vätgasproduktion som metylblåttdegradation.

Jämförelse av de fotokatalytiska studierna i kapitel 6 visade att silvern nanopartiklarna var effektivare på att producera vätgas medan koppar nanopartiklarna visade bättre oxidation av metylblått.

I denna avhandling försökte jag uppnå generering av multipla laddningar inom både molekylära system och system baserade på nanopartiklar. Det visade sig att hybrida system bestående av en gynnsam kombination av molekyler, halvledare och nanopartiklar var de fotokatalytiskt mest aktiva system.

Metallnanopartiklar är mycket bättre ljusfångare jämfört med molekyllära färgämnen och är dessutom kapabla att generera flera laddningar efter excitation med en foton. Molekyllära länkar mellan metallnanopartiklar och halvledaren som lagrar elektroner och därmed ökar livslängden av laddningar kan styra elektronöverföringsegenskaperna.

Detaljerade undersökningar och utveckling av hybrida system är en viktig för framstegen i produktionen av solbränslen.

9. Анотація (Summary in Ukrainian)

Глобальне потепління, зумовлене зростаючим споживанням горючих корисних копалин, є одним із основних викликів для сучасних поколінь. Поетапний перехід від класичних до альтернативних видів енергії є запорукою зменшення викидів парникових газів у атмосферу. Тому необхідність розробки джерел енергії, що мають нейтральний або негативний вуглецевий баланс, стимулює фундаментальні дослідження в галузі відновлюваної енергетики, зокрема перетворення енергії сонця. Сонячні батареї, або фотовольтаїка, що перетворюють сонячне світло у постійний електричний струм завдяки явищу фотоефекта у напівпровідниках, є одним із перспективних напрямків цієї галузі. Проте, через нерівномірне покриття земної поверхні сонячним випромінюванням, як у часі, так і в просторі, важливою задачею є розробка способів перетворення енергії сонця на енергію хімічних зв'язків у вигляді рідкого палива, яке можна було б зберігати та транспортувати. Одним із ключових моментів штучного фотосинтезу «сонячного» палива є процес поглинання світла фотосенсибілізатором, що відповідає за перетворення фотону на електричний заряд (дірку або електрон), доступний для подальших хімічних, зокрема каталітичних, перетворень.

В даній дисертаційній роботі розглянуті три принципово різні типи фотосенсибілізаторів та їх застосування у модельних каталітичних системах фотохімічного відновлення води до молекулярного водню. Дисертація складається із вступу, огляду літератури, експериментальної частини, трьох розділів присвячених результатам і їх обговоренню та висновків.

У розділі 4 представлені результати дослідження молекулярного фотосенсибілізатору бетаніну в реакції відновлення води. Короткий час життя збудженого стану бетаніну перешкоджає ефективному переносу заряду на каталізатор за допомогою диметилвіологену у стаціонарних умовах освітлення. Результати свідчать, що відновлення води при освітленні даної системи не спостерігалось. Тому нами було запропоновано використання наночастинок напівпровідника ZnO у якості електронного реле, яке могло б виступати більш ефективним посередником між фотосенсибілізатором на каталізатором. Було знайдено, що система, яка складається із бетаніну, наночастинок ZnO та молекулярного каталізатора $[\text{FeFe}(\text{mcbdt})(\text{CO})_6]$ ($\text{mcbdt} = 3-$

карбоксібензен-1,2-дітіолат) здатна ефективно відновлювати воду до водню при освітленні видимим світлом. Дослідження системи за допомогою надшвидкої лазерної спектроскопії показали переніс електрона з бетаніну на ZnO з наступним переносом на каталізатор.

У порівнянні із більшістю молекулярних органічних барвників, галогенідні перовскітні напівпровідники, розглянуті у наступному розділі, мають більший час життя у збудженому стані. Було встановлено, що каталітична система яка складається із фотосенсибілізатора CsPbBr₃, реле електронів TiO₂ та рутенієвого каталізатора, здатна генерувати молекулярний водень із води з ефективністю 0.4±0.1%. За допомогою лазерної спектроскопії показано, що при освітленні напівпровідник CsPbBr₃ породжує дірку і електрон, що переносяться на вичерпний донор електронів метиленовий синій та TiO₂ відповідно. Останній є своєрідним депо фотоелектронів, що використовуються Ru для відновлення води. Встановлено, що прикладання магнітного поля призводить до зниження ефективності даної системи внаслідок ефекта Рашби, наслідком якого є пришвидшення небажаної рекомбінації електронів і дірок в CsPbBr₃.

У якості третього типу фотосенсибілізаторів у дисертації розглянуто наночастинки металів, срібла та міді, що мають плазмонний резонанс у видимій області сонячного спектру. Вони були дослідженні у чотирьохкомпонентній системі, що також включала в себе молекулярний лінкер (*l*-амінобензойну кислоту або β -аланін), реле електронів TiO₂ та каталізатор Ru. Було встановлено ключову роль молекулярного лінкера, що опосередковував переніс електрону з наночастинок металів на TiO₂ та, як наслідок, збільшував ефективність системи виділення водню до 20%. За допомогою надшвидкої лазерної спектроскопії показано збільшення сигналу від електронів у зоні провідності TiO₂ при наявності молекулярного лінкера майже втричі. Також було встановлено ефект поверхнево-активної речовини, що використовувалась для синтезу наночастинок металів, на вихід молекулярного водню.

Запропонований в роботі підхід до дизайну систем фотокаталітичного розкладу води на основі наночастинок металів дозволяє неругувати ефективність системи, підбираючи її компоненти: метал для наночастинок, молекулярний лінкер, напівпровідникове реле електронів та каталізатор.

10. Acknowledgements

This thesis would be impossible without people who supported me on both scientific and personal level.

First and foremost, I would like to thank my main supervisor, **Jacinto Sa**, for your support and help during the last years. I am appreciative for your positive vision and energetic motivation in every common project we did. Thank you for your scientific advices and eagerness to answer and discuss questions. Moreover, thank you for the great team we have built up recently, I wish our group to get bigger in near future.

I would like to thank my co-supervisor, **Leif Hammarström**, for the desire to grow the autonomous open-minded scientists, for valuable help you gave, and for the ability to keep very friendly and supportive environment.

I am also grateful to **Stenbjörn Styring**, who seven years ago recruited me as an undergraduate student, and thus gave me chance to start my scientific career in the field of renewable energy.

I would like to thank the team of people who in pair with my supervisors helped to proofread this thesis, namely **Belinda Pettersson**, **Sergii Shylin**, **Edgar Mijangos**, **Yocef Hattori**, **Starla Glover**, and **Luca D’Amario**. Special thanks to **Jens Föhlinger**, for proofreading thesis and for the help with the summary in Swedish.

Thank you, **Anders Thapper**, for being my co-supervisor for the master thesis and for giving me freedom to develop our common projects. I am also appreciative to you and **Patrícia Raleiras** for the support you gave me. **Starla Glover**, thank you for inspiring me, motivating me to grow, and for bringing sport to my everyday life. I would like to thank **Haining Tian** for his trust and support.

I would like to thank the members of the “Mosquito Adventure”, namely **Liisa Antila**, for your hospitality, kind heart and all the pleasant conversations we had. **Edgar Mijangos**, thank you for making me smile from inside, and being happy. Thank you very much for the true support and help in the moments I really need it. Thank you enormously for all your conversations, advice and all the adventures. **Belinda Pettersson**, you are an honest person I love. You are an awesome organizer, and a person with strong positive charisma that attracts people like a magnet. I am very grateful you for how I feel in your company and deeply appreciate your readiness to help. **Luca D’Amario**, thank you for bringing always the cheerful, warm atmosphere, and our unforgettable trips. I am grateful to **Sami Määttä** and **Mohammad**

Mirmohades for your nice company. All of you people are very close for me and I really enjoy our common adventures.

I am very appreciative to people who create friendly and supportive environment in the lab. Thanks to you, I really love our department. Special thanks to **Mohamed Abdellah**, who's positive energetics has charged me billion of times. I am grateful for the enormous support you gave me and really appreciate how you have taught me to operate lasers. **Yocef Hattori**, I am grateful for the relaxed atmosphere you bring, and for readiness to always discuss and support. **Jens Föhliger**, thank you for all help I received from you in last years with lasers and for valuable discussions. **Sol Gutiérrez**, I am appreciative to you for sharing the warm happiness of your heart. **Annamaria Corti**, I admire your way of positive thinking, your sincerity, and really appreciate all the support you gave me. **Maximilian Joscho**, **Bruna Simbelis** and **Ulala Rybińska**, thank you for being very kind and helpful. I really miss you all as the office-mates. **Anna Arkhynchuk**, thank you for your creativeness and support in both personal and scientific spheres. **Yurii Svyaschenko**, thank you for the pleasant company and help you gave me many times. **Hemlata Agarwala** and **Ben Johnson** I am grateful for the harmony and peace that you share. **Juri Mai**, thank you for being supportive person.

I am grateful to my collaborators and co-authors, who has taught me many valuable scientific lessons: **Erick Leite Bastos**, **Daniel Fernandes**, **Janusz Lewinski**, **Ahmed El-Zohry**, **Fikret Mamedov**, **Gustav Bergreen**, **Alena Budinska** and **Sonja Pullen**. Thank you all for sharing your knowledge and skills.

Marina Freitag, thank you for creating easy, good-humored surrounding. I would like to thank **Tomas Edvinsson**, **Emad Mukhtar**, **Reiner Lomoth**, **Ana Morandeira**, **Burkhard Zietz**, **Felix Ho**, **Ping Huang**, **Ann Magnuson**, and **Jan Davidsson** for all the advice that you shared with me. **Christer Elvingson**, thank you for providing the teaching experience.

I am thankful to the physical chemistry group, who has supported me in the lab, sometimes with advice, sometimes with the help: **Astrid Nilsen-Moe**, **Kelly Materna**, **Shihuai Wang**, **Vincent Wang**, **Noémie Ouioui**, **Robin Tyburski**, **Mélina Gilbert Gatty**, **Martin Axelsson**, **Aijie Liu**, **Kyle Virgil**, **Lei Tian**, **Jonas Petersson**, **Julia Broszat**, **Sigrid Berglund**, and **Hannes Michaels**.

Sascha Ott, **Eszter Borbas**, **Henrik Ottosson** and newly created "Synthetic Molecular Chemistry" group, I am appreciative for all your collaborative support and personal positive energy. Special thanks to **Valentina Leandri**, **Keyhan Esfandiartard**, **Muhammad Anwar**, **Nicolas D'Imperio**, **Joshua Green**, **Brian McCarthy**, **Dániel Kovács**, **Holly Redman**, **Livia Mészáros** and **Manuel Boniolo**. **Giovanny Parada** thank you for being cheery, good-tempered person. **Brigi Németh**, I am very appreciative for all your warm hugs and nice words.

I would also like to thank Microbiol group, especially to **Karin Stensjö, Daniel Camsund, Claudia Durall, Feiyan Liang, Rui Miao, João Rodrigues, and Kate Kukil.**

I would like to thank administration team, who has provided great support for me, namely **Jessica Ståhlberg, Terese Magnusson, Lina Rosen, Susanne Söderberg, Anna Fahlén, Anna Cuturic, and Eva Larsson.** Jessica, I am in love with your creativity, and appreciative for the women's choir you have introduced to me. **Patrik Lindahl** and **Peter Lundström** thank you for being IT-professionals. Special thanks to **Sven Johansson** for his readiness to provide universal help whenever needed.

I would like to thank my sport coaches, namely **Dareen Field, Alexandra Coutinho, and Maxine Olausson** for sharing your endless drive with me.

It is an unimaginable gift to have family that love and support you in every step. I am enormously appreciative to my parents **Tetiana Pavliuk, Vasyl Pavliuk**, my grandmother **Anna Kovalchuk**, and of course my beloved sister **Olha Pavliuk.** You are always in my heart and thanks to you, I am happy. I know that my back is always covered.

Being far away from family is hard, but luckily, here in Sweden I met people, who became a family for me. I would like to thank **Dalia Rashed, Eyad Qenawy, Yahia Qenawy, and Dareen Qenawy** for being my standard of nice, supportive family, who bring me feeling of home, while I am in Uppsala. I am grateful to **Cristina Paun** and **Lucca Paun Sa** for your kind heart and wise support throughout all the last years. **Juliana Farah** thank you for making me feel home on my exchange studies in Brazil. **Sofia Föhlinger,** thank you for sincerity and benevolence. I am grateful to **Michele Bedin** and **Elena Di Martino** for your kindness and hospitality. **Xiao Huang, Cuiyan Li** and family, thank you for your support and all the tasty dinners we had. I am very appreciative you, Xiao, for introducing me to the best roommates: **Ping Yan** and **Jie Zheng.** I would like to thank you **Ping Yan** and **Jie Zheng** for all nice evenings, and amusing discussions we had.

Conclusively, I would like to thank my husband, **Sergii Shylin,** for his faith in me, for his encouragement and everyday support in hard moments. Thank you for your sense of humor, care, love and for making me happy.

References

1. Jones G. A.; Warner, K. J. *Energy Policy*, **2016**, *93*, 206–212.
2. Kamat, P.V. Meeting the clean energy demand: nanostructure architectures for solar energy conversion, *J. Phys. Chem. C* **2007**, *111*, 2834–2860.
3. Deffeyes, K. S. Hubbert's Peak: The Impending World Oil Shortage. *Princeton University Press: Princeton*, NJ, **2001**.
4. IPCC, Climate Change 2014: Synthesis Report, **2014**.
5. NASA and NOAA, "Analyses Reveal Record-Shattering Global Warm Temperatures in 2015," **2016**.
6. United Nations Framework Convention on Climate Change, Report of the Conference of the Parties on its twenty-first session, **2015**.
7. Hoffert, M. I.; Caldeira, K.; Jain, A. K.; Haites, E. F.; Danny Harveyk, L. D.; Potter, S. D.; Schlesinger, M. E.; Schneider, S. H.; Watts, R. G.; Wigley, T. M. L.; Wuebbles, D. J. Energy implications of future stabilization of atmospheric CO₂ content. *Nature* **1998**, *395*, 881–884.
8. Rifkin, J. The Third Industrial Revolution; How Lateral Power is Transforming Energy, the Economy, and the World. *New York Times* **2011**.
9. Masson, G.; Kaizuka, I.; Cambiè, C. Snapshot of Global Photovoltaic Market (1992-2017), IEA PVPS, Tech. Rep. **2018**.
10. Lindahl J.; Stoltz, C. National Survey Report of PV Power Applications in Sweden 2017 - IEA PVPS, Swedish Energy Agency, Tech. Rep. October, **2018**.
11. Styring, S. Artificial Photosynthesis for Solar Fuels. *Faraday Discuss.* **2012**, *155*, 357–376.
12. Lewis, N. S. Introduction: Solar energy conversion. *Chem. Rev.*, **2015**, *115*, 12631–12632.
13. Lee, T. D. Ebong, A. U. A review of thin film solar cell technologies and challenges. *Renew. Sust. Energ. Rev.* **2017**, *70*, 1286–1297.
14. Shockley, W.; Queisser, H. J. Detailed Balance Limit of Efficiency of p-n Junction Solar Cells. *J. Appl. Phys.* **1961**, *32*, 510–519.
15. O'Regan, B.; Grätzel, M. A low-cost, high-efficiency solar cell based on dye-sensitized colloidal TiO₂ films. *Nature* **1991**, *353*, 737–740.
16. Lu, L.; Zheng, T.; Wu, Q.; Schneider, A. M.; Zhao, D.; Yu, L. Recent advances in bulk heterojunction polymer solar cells. *Chem. Rev.* **2015**, *115*, 12666–12731.
17. Odobel, F.; Pellegrin, Y.; Gibson, E. A.; Hagfeldt, A.; Smeigh, A. L.; Hammarström, L. Recent Advances and Future Directions to Optimize the Performances of p-type Dye-Sensitized Solar Cells. *Coord. Chem. Rev.* **2012**, *256*, 2414 – 2423.
18. Nozik, A. J.; Beard, M. C.; Luther, J. M.; Law, M.; Ellingson, R. J.; Johnson, J. C. Semiconductor Quantum Dots and Quantum Dot Arrays and Applications of Multiple Exciton Generation to Third-Generation Photovoltaic Solar Cells. *Chem. Rev.* **2010**, *110*, 6873–6890.
19. Green, M. A.; Ho-Baillie, A.; Snaith, H. J. The emergence of perovskite solar cells. *Nature Photon.* **2014**, *8*, 506–514.

20. Erwin, W. R.; Zarick, H. F.; Talbert, E. M.; Bardhan, R. Light trapping in mesoporous solar cells with plasmonic nanostructures. *Energy Environ. Sci.* **2016**, *9*, 1577–1601.
21. Imalka Jayawardena, K. D. G.; Rozanski, L. J.; Mills, C. A.; Beliatas, M. J.; Aamina Nismy N.; R. P. Silva, S. ‘Inorganics-in-Organics’: recent developments and outlook for 4G polymer solar cells. *Nanoscale*, **2013**, *5*, 8411–8427
22. Chu, S.; Cui, Y.; Liu, N. The path towards sustainable energy. *Nature Mater.* **2017**, *16*, 16–22.
23. McEvoy, J. P.; Brudvig, G. W. Water-Splitting Chemistry of Photosystem II, *Chem. Rev.* **2006**, *106*, 4455–4483.
24. Dau, H.; Zaharieva, I. Principles, Efficiency, and Blueprint Character of Solar-Energy Conversion in Photosynthetic Water Oxidation. *Acc. Chem. Res.* **2009**, *42*, 12, 1861–1870.
25. Gust, D.; Moore, T. A. Mimicking Photosynthesis, *Science*, **1989**, *244*, 35–40.
26. Wasielewski, M. R. Photoinduced electron transfer in supramolecular systems for artificial photosynthesis. *Chem. Rev.*, **1992**, *92*, 435–461.
27. Hammarström, L. Accumulative Charge Separation for Solar Fuels Production: Coupling Light-Induced Single Electron Transfer to Multielectron Catalysis. *Acc. Chem. Res.* **2015**, *48*, 840–850.
28. Kim, Y.; Smith, J.G.; Jain, P.K. Harvesting multiple electron–hole pairs generated through plasmonic excitation of Au nanoparticles. *Nature Chem.* **2018**, *10*, 763–769.
29. Chandiran, A. K.; Abdi-Jalebi, M.; Nazeeruddin, M. K.; Grätzel, M. Analysis of Electron Transfer Properties of ZnO and TiO₂ Photoanodes for Dye-Sensitized Solar Cells. *ACS Nano* **2014**, *8*, 2261–2268.
30. Saavedra Becerril, V.; Sundin, E.; Abrahamsson, M. Evidence for Conduction Band-Mediated Two-Electron Reduction of a TiO₂-Bound Catalyst Triggered by Visible Light Excitation of Co-Adsorbed Organic Dyes. *J. Phys. Chem. C* **2018**, *122*, 45, 25822–25828.
31. Karlsson, S.; Boixel, J.; Pelegrin, Y.; Blart, E.; Becker, H.-C.; Odobel, F.; Hammarström, L. Accumulative Charge Separation Inspired by Photosynthesis. *J. Am. Chem. Soc.* **2010**, *132*, 17977–17979.
32. Karlsson, S.; Boixel, J.; Pelegrin, Y.; Blart, E.; Becker, H.-C.; Odobel, F.; Hammarström, L. Accumulative Electron Transfer: Multiple Charge Separation in Artificial Photosynthesis. *Faraday Disc.* **2012**, *155*, 233–252.
33. Sundin, E.; Abrahamsson, M. Long-lived charge separation in dye–semiconductor assemblies: a pathway to multi-electron transfer reactions. *Chem. Commun.* **2018**, *54*, 5289–5298.
34. Materna, K.L.; Crabtree, R.H.; Brudvig, G.W. Anchoring groups for photocatalytic water oxidation on metal oxide surfaces. *Chem. Soc. Rev.* **2017**, *46*, 6099–6110.
35. Wiberg, J.; Marinado, T.; Hagberg, D. P.; Sun, L.; Hagfeldt, A.; Albinsson, B. Effect of Anchoring Group on Electron Injection and Recombination Dynamics in Organic Dye-Sensitized Solar Cells. *J. Phys. Chem. C* **2009**, *113*, 9, 3881–3886.
36. Shylin, S.I.; Pavliuk, M.V.; D’Amario, L.; Mamedov, F.; Sá, J.; Berggren, G.; Fritsky, I.O. Efficient Visible Light-Driven Water Oxidation Catalyzed by an Iron (IV) Clathrochelate Complex. *Submitted*.
37. Pavliuk, M.V.; Mijangos, E.; Makhankova, V.G.; Kokozay, V.N.; Pullen, S.; Liu, J.; Zhu, J.; Styring, S.; Thapper, A. Homogeneous Cobalt/Vanadium Complexes as Precursors for Functionalized Mixed Oxides in Visible-Light-Driven Water Oxidation. *ChemSusChem*. **2016**, *9*, 2957–2966.

38. Pavliuk, M.V.; Makhankova, V.G.; Kokozay, V.N.; Omelchenko, I.V.; Jezi-
erska, J.; Thapper, A.; Styring, S. Structural, Magnetic, Thermal and Visible
Light-Driven Water Oxidation Studies of Heterometallic Mn/V Complexes. *Pol-
yhedron* **2015**, *88*, 81–89.
39. Eckenhoff, W. T.; Eisenberg, R. Molecular systems for light driven hydrogen
production. *Dalton Trans.*, **2012**, *41*, 13004–13021.
40. Berardi, S.; Drouet, S.; Francas, L.; Gimbert-Surinach, C.; Guttentag, M.; Rich-
mond, C.; Stolla, T.; Llobet, A. Molecular artificial photosynthesis. *Chem. Soc.
Rev.* **2014**, *43*, 7501–7519.
41. Lomoth, R.; Häupl, T.; Johansson, O.; Hammarström, L. Redox-Switchable Di-
rection of Photoinduced Electron Transfer in an Ru(bpy)₃²⁺ - Viologen Dyad.
Chem. Eur. J. **2002**, *8*, 102–110.
42. Sun, S.; Zhang, R.; Andersson, S.; Pan, J.; Åkermark, B.; Sun, L. The photoin-
duced long-lived charge-separated state of Ru(bpy)₃-methylviologen with cu-
curbit[8]uril in aqueous solution. *Chem. Commun.* **2006**, 4195–4197.
43. Fihri, A.; Artero, V.; Razavet, M.; Baffert, C.; Leibl W.; Fontecave, M. Cobalox-
ime-Based Photocatalytic Devices for Hydrogen Production. *Angew. Chem., Int.
Ed.* **2008**, *47*, 564–567.
44. Li, C.; Wang, M.; Pan, J.; Zhang, P.; Zhang R.; Sun, L. Photochemical hydrogen
production catalyzed by polypyridyl ruthenium–cobaloxime heterobinuclear
complexes with different bridges. *J. Organomet. Chem.* **2009**, *694*, 2814–2819.
45. Zhang, P.; Wang, M.; Li, C.; Li, X.; Dong J.; Sun, L. Photochemical H₂ produc-
tion with noble-metal-free molecular devices comprising a porphyrin photosen-
sitizer and a cobaloxime catalyst. *Chem. Commun.* **2010**, *46*, 8806–8808.
46. McCormick, T. M.; Han, Z.; Weinberg, D. J.; Brennessel, W. W.; Holland, P.
L.; Eisenberg, R. Impact of Ligand Exchange in Hydrogen Production from Co-
baloxime-Containing Photocatalytic Systems. *Inorg. Chem.* **2011**, *50*, 10660–
10666.
47. Veldkamp, B. S.; Han, W.-S.; Dyar, S. M.; Eaton, S. W.; Ratner, M. A.;
Wasielewski, M. R. Photoinitiated multi-step charge separation and ultrafast
charge transfer induced dissociation in a pyridyl-linked photosensitizer–co-
baloxime assembly. *Energy Environ. Sci.* **2013**, *6*, 1917–1928.
48. O'Neil, M. P.; Niemczyk, M. P.; Svec, W. A.; Gosztola, D.; Gaines, G. L.;
Wasielewski, M. R. Picosecond optical switching based on biphotonic excitation
of an electron donor-acceptor-donor molecule. *Science* **1992**, *257*, 63.
49. Konduri, R.; de Taconi, N.R.; Rajeshwar, K.; MacDonnell, F.M. Multielectron
Photoreduction of a Bridged Ruthenium Dimer,
[(phen)₂Ru(tatpp)Ru(phen)₂][PF₆]₄: Aqueous Reactivity and Chemical and
Spectroelectrochemical Identification of the Photoproducts. *J. Am. Chem. Soc.*
2004, *126*, 11621–11629.
50. Elliott, K. J.; Harriman, A.; Le Pleux, L.; Pellegrin, Y.; Blart, E.; Mayer, C. R.;
Odobel, F. A porphyrin–polyoxometallate bio-inspired mimic for artificial pho-
tosynthesis *Phys. Chem. Chem. Phys.* **2009**, *11*, 8767.
51. Huang, P.; Magnuson, A.; Lomoth, R.; Abrahamsson, M.; Tamm, M.; Sun, L.;
van Rotterdam, B.; Park, J.; Hammarström, L.; Åkermark, B.; Styring, S. Photo-
induced oxidation of a dinuclear Mn₂^{II,II} complex to the Mn₂^{III,IV} state by inter-
and intramolecular electron transfer to Ru^{III}tris-bipyridine. *J. Inorg. Biochem.*
2002, *91*, 159–172.
52. Wu, L.-Z.; Chen, B.; Li, Z.-J.; Tung, C.-H. Enhancement of the Efficiency of
Photocatalytic Reduction of Protons to Hydrogen via Molecular Assembly. *Acc.
Chem. Res.* **2014**, *47*, 2177–2185.

53. Borgström, M.; Shaikh, N.; Johansson, O.; Anderlund, M. F.; Styring, S.; Åkermark, B.; Magnuson, A.; Hammarström, L. Light Induced Manganese Oxidation and Long-Lived Charge Separation in a $\text{Mn}^{\text{II,III}}\text{-Ru}^{\text{II}}(\text{bpy})_3$ -Acceptor Triad. *J. Am. Chem. Soc.* **2005**, *127*, 17504–17515.
54. Borgström, M.; Ott, S.; Lomoth, R.; Bergquist, J.; Hammarström, L.; Johansson, O. Photoinduced Energy Transfer Coupled to Charge Separation in a $\text{Ru}(\text{II})\text{-Ru}(\text{II})\text{-Acceptor}$ Triad. *Inorg. Chem.* **2006**, *45*, 4820–4829.
55. Ismail, A. A.; Bahnemann, D. W. Photochemical splitting of water for hydrogen production by photocatalysis: A review. *Sol. Energ. Mat. Sol. C.* **2014**, *128*, 85–101.
56. Chen, X.; Yu, T.; Fan, X.; Zhang, H.; Li, Z.; Ye, J.; Zou, Z. Enhanced activity of mesoporous Nb_2O_5 for photocatalytic hydrogen production, *Appl. Surf. Sci.* **2007**, *253*, 8500–8506.
57. Saito, N.; Kadowaki, H.; Kobayashi, H.; Ikarashi, K.; Nishiyama, H.; Inoue, Y.; A new photocatalyst of RuO_2 -loaded PbWO_4 for overall splitting of water, *Chem. Lett.* **2004**, *33*, 1452–1453.
58. Fujishima, A.; Honda, K. Electrochemical photolysis of water at a semiconductor electrode. *Nature* **1972**, *238*, 37–38.
59. Abe, R. Recent progress on photocatalytic and photoelectrochemical water splitting under visible light irradiation, *J. Photochem. Photobiol. C* **2010**, *11*, 179–209.
60. Khan, M.A.; Yang, O.-B. Photocatalytic water splitting for hydrogen production under visible light on Ir and Co ionized titania nanotube. *Catal. Today* **2009**, *146*, 177–182.
61. Chen, X.; Burda, C. The Electronic Origin of the Visible-Light Absorption Properties of C-, N- and S-Doped TiO_2 Nanomaterials. *J. Am. Chem. Soc.*, **2008**, *130*, 5018–5019.
62. Asahi, R.; Morikawa, T.; Ohwaki, T.; Aoki, K.; Taga, Y. Visible-light photocatalysis in nitrogen-doped titanium oxides. *Science* **2001**, *293*, 269–271.
63. Tao, J.; Luttrell, T.; Batzill, M. A two-dimensional phase of TiO_2 with a reduced bandgap. *Nat. Chem.* **2011**, *3*, 296–300.
64. Chen, X.; Liu, L.; Peter, Y.Y.; Mao, S.S. Increasing solar absorption for photocatalysis with black hydrogenated titanium dioxide nanocrystals. *Science* **2011**, *331*, 746–750.
65. Ozgur, U.; Alivov, Y. I.; Liu, C.; Teke, A.; Reshchikov, M. A.; Dogan, S.; Avrutin, V.; Cho, S.-J.; Morkoc, H. A Comprehensive Review of ZnO Materials and Devices. *J. Appl. Phys.* **2005**, *98*, 41301.
66. Kiwi, J.; Borgarello, E.; Pelizzetti, E.; Visca, M.; Grätzel, M. Cyclic water cleavage by visible light: drastic improvement of yield of H_2 and O_2 with bifunctional redox catalysts, *Angew. Chem., Int. Ed.* **1980**, *19*, 646–648.
67. Boschloo, G.; Hagfeldt, A. Characteristics of the Iodide/Triiodide Redox Mediator in Dye-Sensitized Solar Cells. *Acc. Chem. Res.* **2009**, *42*, 1819–1826.
68. Reisner, E. Powell, D.J.; Cavazza, C.; Fontecilla-Camps, J.C.; Armstrong, F.A.; Visible light-driven H_2 production by hydrogenases attached to dye-sensitized TiO_2 nanoparticles, *J. Am. Chem. Soc.* **2009**, *131*, 18457–18466.
69. Freitag, M.; Teuscher, J.; Saygili, Y.; Zhang, X.; Giordano, F.; Liska, P.; Hua, J.; Zakeeruddin, S.M.; Moser, J.-E.; Grätzel, M.; Hagfeldt, A. Dye-sensitized solar cells for efficient power generation under ambient lighting. *Nat. Photonics* **2017**, *11*, 372–378.
70. Chen, H.-Y.; Ardo, S. Direct observation of sequential oxidations of a titania-bound molecular proxy catalyst generated through illumination of molecular sensitizers. *Nat. Chem.* **2018**, *10*, 17–23.

71. Zhang, Y.; He, S.; Guo, W.; Hu, Y.; Huang, J.; Mulcahy, J. R.; Wei, W. D. Surface-Plasmon-Driven Hot Electron Photochemistry. *Chem. Rev.* **2018**, *118*, 2927–2954.
72. Zheng, Z.; Tachikawa, T.; Majima, T. Single-Particle Study of Pt-Modified Au Nanorods for Plasmon-Enhanced Hydrogen Generation in Visible to Near-Infrared Region. *J. Am. Chem. Soc.* **2014**, *136*, 6870–6873.
73. Lou, Z.; Fujitsuka, M.; Majima, T. Pt–Au Triangular Nanoprisms with Strong Dipole Plasmon Resonance for Hydrogen Generation Studied by Single-Particle Spectroscopy. *ACS Nano* **2016**, *10*, 6299–6305.
74. Bauer, C.; Abid, J.; Girault, H. H. Hot Adsorbate-Induced Retardation of the Internal Thermalization of Nonequilibrium Electrons in Adsorbate-Covered Metal Nanoparticles. *J. Phys. Chem. B* **2006**, *110*, 4519–4523.
75. Yan, L.; Wang, F.; Meng, S. Quantum Mode Selectivity of Plasmon-Induced Water Splitting on Gold Nanoparticles. *ACS Nano* **2016**, *10*, 5452–5458.
76. Mubeen, S.; Lee, J.; Singh, N.; Kramer, S.; Stucky, G. D.; Moskovits, M. An Autonomous Photosynthetic Device in Which All Charge Carriers Derive from Surface Plasmons. *Nat. Nanotechnol.* **2013**, *8*, 247–251.
77. Zhu, M.; Cai, X.; Fujitsuka, M.; Zhang, J.; Majima, T. Au/La₂Ti₂O₇ Nanostructures Sensitized with Black Phosphorus for Plasmon-Enhanced Photocatalytic Hydrogen Production in Visible and Near-Infrared Light. *Angew. Chem., Int. Ed.* **2017**, *56*, 2064–2068.
78. Hong, J. W.; Wi, D. H.; Lee, S.; Han, S. W. Metal–Semiconductor Heteronano-crystals with Desired Configurations for Plasmonic Photocatalysis. *J. Am. Chem. Soc.* **2016**, *138*, 15766–15773.
79. Qian, K.; Sweeny, B. C.; Johnston-Peck, A. C.; Niu, W.; Graham, J. O.; DuChene, J. S.; Qiu, J.; Wang, Y.; Engelhard, M. H.; Su, D.; Stach, E. A.; Wei, W. D. Surface Plasmon-Driven Water Reduction: Gold Nanoparticle Size Matters. *J. Am. Chem. Soc.* **2014**, *136*, 9842–9845.
80. Ng, C.; Cadusch, J. J.; Dligatch, S.; Roberts, A.; Davis, T. J.; Mulvaney, P.; Gomez, D. E. Hot Carrier Extraction with Plasmonic Broadband Absorbers. *ACS Nano* **2016**, *10*, 4704–4711.
81. Bian, Z.; Tachikawa, T.; Zhang, P.; Fujitsuka, M.; Majima, T. Au/TiO₂ Superstructure-Based Plasmonic Photocatalysts Exhibiting Efficient Charge Separation and Unprecedented Activity. *J. Am. Chem. Soc.* **2014**, *136*, 458–465.
82. DuChene, J. S.; Sweeny, B. C.; Johnston-Peck, A. C.; Su, D.; Stach, E. A.; Wei, W. D. Prolonged Hot Electron Dynamics in Plasmonic-Metal/Semiconductor Heterostructures with Implications for Solar Photocatalysis. *Angew. Chem., Int. Ed.* **2014**, *53*, 7887–7891.
83. Seeger, K. Semiconductor Physics: An Introduction. Advanced Texts in Physics. ISBN 9783540219576.
84. Bohren, C. F.; Huffman, D. R. Absorption and Scattering of Light by Small Particles, **1983**, Wiley.
85. Gangishetty, M. K.; Scott, R. W. J.; Kelly, T. L. Panchromatic Enhancement of Light-Harvesting Efficiency in Dye-Sensitized Solar Cells Using Thermally Annealed Au@SiO₂ Triangular Nanoprisms. *Langmuir* **2014**, *30*, 14352–14359.
86. Hsu, H.-L.; Juang, T.-Y.; Chen, C.-P.; Hsieh, C.-M.; Yang, C.-C.; Huang, C.-L.; Jeng, R.-J. Enhanced efficiency of organic and perovskite photovoltaics from shape-dependent broadband plasmonic effects of silver nanoplates. *Sol. Energy Mater. Sol. Cells* **2015**, *140*, 224–231.
87. Zarick, H. F.; Hurd, O.; Webb, J. A.; Hungerford, C.; Erwin, W. R.; Bardhan, R. Enhanced Efficiency in Dye-Sensitized Solar Cells with Shape-Controlled Plasmonic Nanostructures. *ACS Photonics* **2014**, *1*, 806–811.

88. Zhang, H.; Govorov, A. O. Optical Generation of Hot Plasmonic Carriers in Metal Nanocrystals: The Effects of Shape and Field Enhancement. *J. Phys. Chem. C* **2014**, *118*, 7606–7614.
89. Brown, A. M.; Sundararaman, R.; Narang, P.; Goddard, W. A. Atwater, H. A. Ab Initio Phonon Coupling and Optical Response of Hot Electrons in Plasmonic Metals. *Phys. Rev. B: Condens. Matter Mater. Phys.* **2016**, *94*, 075120.
90. Knight, M. W.; Sobhani, H.; Nordlander P.; Halas, N. J. Photodetection with Active Optical Antennas. *Science* **2011**, *332*, 702–704.
91. Wu, K.; Chen, J.; McBride J. R.; Lian, T. Efficient hot-electron transfer by a plasmon-induced interfacial charge-transfer transition. *Science* **2015**, *349*, 3584–3588.
92. Boerigter, C.; Campana, R.; Morabito, M.; Linic, S. Evidence and Implications of Direct Charge Excitation as the Dominant Mechanism in Plasmon-Mediated Photocatalysis. *Nat. Commun.* **2016**, *7*, 10545.
93. Wu, K.; Chen, J.; McBride, J. R.; Lian, T. Efficient Hot-Electron Transfer by a Plasmon-Induced Interfacial Charge-Transfer Transition. *Science* **2015**, *349*, 632–635.
94. Furube, A.; Du, L.; Hara, K.; Katoh, R.; Tachiya, M. Ultrafast Plasmon-Induced Electron Transfer from Gold Nanodots into TiO₂ Nanoparticles. *J. Am. Chem. Soc.* **2007**, *129*, 14852–14853.
95. Manjavacas, A.; Liu, J. G.; Kulkarni V.; Nordlander, P. Plasmon-Induced Hot Carriers in Metallic Nanoparticles. *ACS Nano*, **2014**, 7630–7638.
96. Voisin, C.; Del Fatti, N.; Christofilos, D.; Vallée, F. Ultrafast Electron Dynamics and Optical Nonlinearities in Metal Nanoparticles. *J. Phys. Chem. B* **2001**, *105*, 2264–2280.
97. Furube, A.; Du, L.; Hara, K.; Katoh, R.; Tachiya, M. Ultrafast Plasmon-Induced Electron Transfer from Gold Nanodots into TiO₂ Nanoparticles. *J. Am. Chem. Soc.* **2007**, *129*, 14852–14853.
98. Lakowicz, J.R. *Principles of Fluorescence Spectroscopy*, 3rd ed.; Springer, **2006**.
99. Fernandes, D.L.A.; Pavliuk, M. V.; Sá, J. A 3D printed microliquid jet with an adjustable nozzle diameter. *Analyst* **2015**, *140*, 6234–6238.
100. Fernandes, D.L.A.; Budinská, A.; Pavliuk, M.V.; Sá, J. Novel Photo-Reactor for Fast Screening of Photo-Catalytic Systems. *J. Photoch. Photobio. A* **2017**, 36–39.
101. *The vacuum technology book*, Pfeiffer Vacuum GmbH, 2, **2013**.
102. Saraswat, S. K.; Rodene, D. D.; Gupta, R. B. Recent advancements in semiconductor materials for photoelectrochemical water splitting for hydrogen production using visible light. *Renew. Sust. Energ. Rev.* **2018**, *89*, 228–248.
103. Knorr, F. J.; McHale, J. L.; Clark, A. E.; Marchioro, A.; Moser, J.-E. Dynamics of Interfacial Electron Transfer from Betanin to Nanocrystalline TiO₂: The Pursuit of Two-Electron Injection. *J. Phys. Chem. C* **2015**, *119*, 19030–19041.
104. Zhang, D.; Lanier, S. M.; Downing, J. A.; Avent, J. L.; Lum, J.; McHale, J. L. Betalain pigments for dye-sensitized solar cells. *J. Photoch. Photobio. A* **2008**, *195*, 72–80.
105. Wybraniec, S.; Michazowski, T. New pathways of betanidin and betanin enzymatic oxidation. *J. Agric. Food Chem.* **2011**, *59*, 9612–9622.
106. Shalini, S.; Balasundara Prabhu, R.; Prasanna, S.; Mallick, T. K.; Senthilarasu, S. Review on natural dye sensitized solar cells: Operation, materials and methods. *Renew. Sust. Energ. Rev.* **2015**, *51*, 1306–1325.
107. Richhariya, G.; Kumara, A.; Tekasakul, P.; Gupta, B. Natural dyes for dye sensitized solar cell: A review. *Renew. Sust. Energ. Rev.* **2017**, *69*, 705–718.

108. Treat, N. A.; Knorr, F. J.; McHale, J. L., Templated Assembly of Betanin Chromophore on TiO₂: Aggregation-Enhanced Light-Harvesting and Efficient Electron Injection in a Natural Dye-Sensitized Solar Cell. *J. Phys. Chem. C* **2016**, *120* (17), 9122–9131.
109. Sandquist, C.; McHale, J. L., Improved efficiency of betanin-based dye-sensitized solar cells. *J. Photoch. Photobio. A* **2011**, *221* (1), 90–97.
110. Bock, C. R.; Meyer, T. J.; Whitten, D. G., Electron transfer quenching of the luminescent excited state of tris(2,2'-bipyridine)ruthenium(II). Flash photolysis relaxation technique for measuring the rates of very rapid electron transfer reactions. *J. Am. Chem. Soc.* **1974**, *96*, 4710–4712.
111. Pires Gonçalves, L.C.; de Souza Trassi, M. A.; Barbosa Lopes, N.; Dörr, F. A.; dos Santos, M. T.; Baader, W. J.; Oliveira Jr., V. X.; Bastos, E. L. A comparative study of the purification of betanin, *Food Chem.* **2012**, *131*, 231–238.
112. Wendel, M.; Kumorkiewicz, A.; Wybraniec, S.; Ziółek, M.; Burdziński, G., Impact of S₁→S₀ internal conversion in betalain-based dye sensitized solar cells. *Dyes Pigments* **2017**, *141*, 306–315.
113. Wybraniec, S.; Stalica, P.; Jerz, G.; Klose, B.; Gebers, N.; Winterhalter, P.; Spórna, A.; Szaleniec, M.; Mizrahi, Y. Separation of polar betalain pigments from cacti fruits of *Hylocereus polyrhizus* by ion-pair high-speed countercurrent chromatography. *J. Chromatogr. A* **2009**, *1216*(41), 6890–6899.
114. Sreeja, S.; Pesala, B. Co-sensitization aided efficiency enhancement in betanin-chlorophyll solar cell. *Mater. Renew. Sustain. Energ.* **2018**, *7*, 25.
115. Correa-Baena, J.P.; Abate, A.; Saliba, M.; Tress, W.; Jacobsson, T.J.; Gratzel, M.; Hagfeldt, A. The rapid evolution of highly efficient perovskite solar cells. *Energ. Environ. Science* **2017**, *10*, 710–727.
116. Huang, J.; Yuan, Y.; Shao, Y.; Yan, Y. Understanding the physical properties of hybrid perovskites for photovoltaic applications. *Nat. Rev. Mater.* **2017**, *2*, 17042.
117. de Quilletes, D. W.; Vorpahl, S. M.; Stranks, S. D.; Nagaoka, H.; Eperon, G. E.; Ziffer, M. E.; Snaith H. J.; Ginger, D. S. Impact of microstructure on local carrier lifetime in perovskite solar cells. *Science* **2015**, *348*, 683–686.
118. Dong, Q.; Fang, Y.; Shao, Y.; Mulligan, P.; Qiu, J.; Cao, L.; Huang, J. Electron-hole diffusion lengths > 175 μm in solution-grown CH₃NH₃PbI₃ single crystals. *Science* **2015**, *347*, 967–970.
119. Pullen, S.; Fei, H.; Orthaber, A.; Cohen S. M.; Ott, S. Enhanced Photochemical Hydrogen Production by a Molecular Diiron Catalyst Incorporated into a Metal-Organic Framework. *J. Am. Chem. Soc.* **2013**, *135*, 16997–17003.
120. Gloaguen, F.; Lawrence, J. D.; Rauchfuss, T.B. Biomimetic Hydrogen Evolution Catalyzed by an Iron Carbonyl Thiolate. *J. Am. Chem. Soc.* **2001**, *123*, 9476–9477.
121. Samuel, A. P. S.; Co, D. T.; Stern, C. L.; Wasielewski, M. R. Ultrafast Photo-driven Intramolecular Electron Transfer from a Zinc Porphyrin to a Readily Reduced Diiron Hydrogenase Model Complex. *J. Am. Chem. Soc.* **2010**, *132*, 8813–8815.
122. Wang, F.; Wang, W.-G.; Wang, X.-J.; Wang, H.-Y.; Tung, C.-H.; Wu, L.-Z. A Highly Efficient Photocatalytic System for Hydrogen Production by a Robust Hydrogenase Mimic in an Aqueous Solution. *Angew. Chem., Int. Ed.* **2011**, *50*, 3193–3197.
123. Jian, J.-X.; Ye, C.; Wang, X.-Z.; Wen, M.; Li, Z.-J.; Li, X.-B.; Chen, B.; Tung, C.-H.; Wu, L.-Z. Comparison of H₂ photogeneration by [FeFe]-hydrogenase mimics with CdSe QDs and Ru(bpy)₃Cl₂ in aqueous solution. *Energy Environ. Sci.* **2016**, *9*, 2083–2089.

124. Brown, A. M.; Antila, L. J.; Mirmohades, M.; Pullen, S.; Ott, S.; Hammarström L. Ultrafast Electron Transfer Between Dye and Catalyst on a Mesoporous NiO Surface. *J. Am. Chem. Soc.* **2016**, *138*, 8060–8063.
125. Gilbert Gatty, M.; Pullen, S.; Sheibani, E.; Tian, H.; Ott, S.; Hammarström, L. Direct Evidence of Catalyst Reduction on Dye and Catalyst Co-Sensitized NiO Photocathodes by Midinfrared Transient Absorption Spectroscopy. *Chem. Sci.* **2018**, *9*, 4983–4991.
126. Huang, M.-C.; Wang, T.; Wu, B.-J.; Lin, J.-C.; Wu, C.-C. Anodized ZnO nanostructures for photoelectrochemical water splitting. *Appl. Surf. Sci.* **2016**, *360*, 442–450.
127. Yang, X.; Wolcott, A.; Wang, G.; Sobo, A.; Fitzmorris, R.C.; Qian, F.; Zhang, J.Z.; Li, Y. Nitrogen-doped ZnO nanowire arrays for photoelectrochemical water splitting. *Nano Lett.* **2009**, *9*, 2331–2336.
128. Olson, D. C.; Lee, Y. J.; White, M. S.; Kopidakis, N.; Shaheen, S. E.; Ginley, D. S.; Voigt J. A.; Hsu, J. W. P. Effect of Polymer Processing on the Performance of Poly(3-hexylthiophene)/ZnO Nanorod Photovoltaic Devices. *J. Phys. Chem. C* **2007**, *111*, 16640–16645.
129. Keis, K.; Bauer, C.; Boschloo, G.; Hagfeldt, A.; Westermarck, K.; Rensmo H.; Siegbahn, H. Nanostructured ZnO electrodes for dye-sensitized solar cell applications. *J. Photochem. Photobiol., A* **2002**, *148*, 57–64.
130. Keis, K.; Magnusson, E.; Lindstrom, H.; Lindquist, S. E.; Hagfeldt, A. A 5% efficient photoelectrochemical solar cell based on nanostructured ZnO electrodes. *Sol. Energy Mater. Sol. Cells* **2002**, *73*, 51–58.
131. Vayssieres, L.; Keis, K.; Hagfeldt, A.; Lindquist, S. E. Three-Dimensional Array of Highly Oriented Crystalline ZnO Microtubes. *Chem. Mater.* **2001**, *13*, 4395–4398.
132. Schindler, T.; Schmiele, M.; Schmutzler, T.; Kassar, T.; Segets, D.; Peukert, W.; Radulescu, A.; Kriele, A.; Gilles, R.; Unruh, T. A Combined SAXS/SANS Study for the in Situ Characterization of Ligand Shells on Small Nanoparticles: The Case of ZnO. *Langmuir* **2015**, *31*, 10130–10136.
133. Redmond, G.; Fitzmaurice, D.; Grätzel, M. Visible Light Sensitization by *cis*-Bis(thiocyanato)bis(2,2'-bipyridyl-4,4'-dicarboxylato)ruthenium(II) of a Transparent Nanocrystalline ZnO Film Prepared by Sol-Gel Techniques. *Chem. Mater.* **1994**, *6*, 686–691.
134. Xiao, J.; Hou, X.; Zhao, L.; Li, Y. A conductive ZnO: Ga/ZnO core-shell nanorod photoanode for photoelectrochemical water splitting. *Int. J. Hydrog. Energ.* **2016**, *41*, 14596–14604.
135. Grala, A.; Wolska-Pietkiewicz, M.; Danowski, W.; Wrobel, Z.; Grzonka J.; Lewinski, J. 'Clickable' ZnO nanocrystals: the superiority of a novel organometallic approach over the inorganic sol-gel procedure *Chem. Commun.* **2016**, *52*, 7340–7343.
136. Paczesny, J.; Wolska-Pietkiewicz, M.; Binkiewicz, I.; Wrobel, Z.; Wadowska, M.; Matuła, K.; Dziecielewska, I.; Pocięcha, D.; Smalc-Koziorowska, J.; Lewinski J.; Hołyst, R. Towards Organized Hybrid Nanomaterials at the Air/Water Interface Based on Liquid-Crystal/ZnO Nanocrystals. *Chem. – Eur. J.* **2015**, *21*, 16941–16947.
137. Braten, M.N.; Gamelin, D.R.; Mayer, J.M. Reaction Dynamics of Proton-Coupled Electron Transfer from Reduced ZnO Nanocrystals. *ACS Nano* **2015**, *9*, 10258–10267.
138. Schrauben, J.N.; Hayoun, R.; Valdez, C.N.; Braten, M.; Fridley, L.; Mayer, J.M. Titanium and Zinc Oxide Nanoparticles are Proton-Coupled Electron Transfer Agents. *Science* **2012**, *336*, 1298–1301.

139. Jacobsson, T.J.; Viarbitskaya, S.; Mukhtar, E.; Edvinsson, T. A size dependent discontinuous decay rate for the exciton emission in ZnO quantum dots. *Phys. Chem. Chem. Phys.* **2014**, *16*, 13849–13857.
140. Reynolds, G.A.; Drexhage, K.H. New Coumarin Dyes with Rigidized Structure for Flashlamp-Pumped Dye Lasers. *Opt. Commun.* **1975**, *13*, 222–225.
141. Jacobsson, T.J.; Viarbitskaya, S.; Mukhtar, E.; Edvinsson, T. A Size Dependent Discontinuous Decay Rate for the Exciton Emission in ZnO Quantum Dots. *Phys. Chem. Chem. Phys.* **2014**, *16*, 13849–13857.
142. Berberan-Santos, M.; Bodunov, E.; Valeur, B. Mathematical Functions for the Analysis of Luminescence Decays with Underlying Distributions I. Kohlrausch Decay Function (Stretched Exponential). *Chem. Phys.* **2005**, *315*, 171–182.
143. Willis, R. L.; Olson, C.; O'Regan, B.; Lutz, T.; Nelson, J.; Durrant, J. R. Electron Dynamics in Nanocrystalline ZnO and TiO₂ Films Probed by Potential Step Chronoamperometry and Transient Absorption Spectroscopy. *J. Phys. Chem. B* **2002**, *106*, 7605–7613.
144. Koida, T.; Uedono, A.; Tsukazaki, A.; Sota, T.; Kawasaki, M.; Chichibu, S. F. Direct comparison of photoluminescence lifetime and defect densities in ZnO epilayers studied by time-resolved photoluminescence and slow positron annihilation techniques. *Phys. Status Solidi A* **2004**, *201*, 2841–2845.
145. Zhong, Y.; Djurišić, A.B.; Hsu, Y.F.; Wong, K.S.; Brauer, G.; Ling, C.C.; Chan, W.K. Exceptionally Long Exciton Photoluminescence Lifetime in ZnO Tetrapods. *J. Phys. Chem. C* **2008**, *112*, 16286–16295.
146. Pozina, G.; Yang, L. L.; Zhao, Q. X.; Hultman, L.; Lagoudakis P. G. Size dependent carrier recombination in ZnO nanocrystals. *Appl. Phys. Lett.* **2010**, *97*, 131909.
147. Mirmohades, M.; Pullen, S.; Stein, M.; Maji, S.; Ott, S.; Hammarström, L.; Lomoth R. Direct Observation of Key Catalytic Intermediates in a Photoinduced Proton Reduction Cycle with a Diiron Carbonyl Complex. *J. Am. Chem. Soc.* **2014**, *136*, 17366–17369.
148. Wang, S.; Aster, A.; Mirmohades, M.; Lomoth, R.; Hammarström, L. Structural and Kinetic Studies of Intermediates of a Biomimetic Diiron Proton-Reduction Catalyst. *Inorg. Chem.* **2018**, *57*, 768–776.
149. Streich, D.; Astuti, Y.; Orlandi, M.; Schwartz, L.; Lomoth, R.; Hammarström, L.; Ott, S. High-Turnover Photochemical Hydrogen Production Catalyzed by a Model Complex of the [FeFe]-Hydrogenase Active Site. *Chem. Eur. J.* **2010**, *16*, 60–63.
150. Yang, S.; Fu, W.; Zhang, Z.; Chen, H.; Li, C.-Z. Recent advances in perovskite solar cells: efficiency, stability and lead-free perovskite. *J. Mater. Chem. A* **2017**, *5*, 11462.
151. Saliba, M.; Matsui, T.; Domanski, K.; Seo, J.-Y.; Ummadisingu, A.; Zakeeruddin, S. M.; Correa-Baena, J.-P.; Tress, W. R.; Abate, A.; Hagfeldt, A.; Grätzel, M. Incorporation of rubidium cations into perovskite solar cells improves photovoltaic performance. *Science* **2016**, *354*, 206–209.
152. Park, B. W.; Philippe, B.; Zhang, X. L.; Rensmo, H.; Boschloo, G.; Johansson, E. M. J. Bismuth Based Hybrid Perovskites A₃BiI₉ (A: Methylammonium or Cesium) for Solar Cell Application. *Adv. Mater.* **2015**, *27*, 6806–6813.
153. Kovalenko, M. V.; Protesescu, L.; Bodnarchuk, M. I. Properties and potential optoelectronic applications of lead halide perovskite nanocrystals. *Science* **2017**, *358*, 745–750.
154. Protesescu, L.; Yakunin, S.; Bodnarchuk, M. I.; Krieg, F.; Caputo, R.; Hendon, C. H.; Yang, R. X.; Walsh, A.; Kovalenko, M. V. Nanocrystals of Cesium Lead Halide Perovskites (CsPbX₃, X = Cl, Br, and I): Novel Optoelectronic Materials

- Showing Bright Emission with Wide Color Gamut. *Nano Lett.* **2015**, *15*, 3692–3696.
155. Aristidou, N.; Eames, C.; Sanchez-Molina, I.; Bu, X.; Kosco, J.; Islam, M. S.; Haque, S. A. Fast oxygen diffusion and iodide defects mediate oxygen-induced degradation of perovskite solar cells. *Nat. Commun.* **2017**, *8*, 15218.
 156. Li, Z.; Kong, L.; Huang, S.; Li, L. Highly Luminescent and Ultrastable CsPbBr₃ Perovskite Quantum Dots Incorporated into a Silica/Alumina Monolith. *Angew. Chem. Int. Ed.* **2017**, *56*, 8134–8138.
 157. Zhang, C.; Sun, D.; Sheng, C.-X.; Zhai, Y. X.; Mielczarek, K.; Zakhidov, A.; Vardeny, Z. V. Magnetic field effects in hybrid perovskite devices. *Nat. Phys.* **2015**, *11*, 427–434.
 158. Hsiao, Y.-C.; Wu, T.; Li, M.; Hu, B. Magneto-Optical Studies on Spin-Dependent Charge Recombination and Dissociation in Perovskite Solar Cells. *Adv. Mater.* **2015**, *27*, 2899–2906.
 159. Protesescu, L.; Yakunin, S.; Bodnarchuk, M. I.; Krieg, F.; Caputo, R.; Hendon, C. H.; Yang, R. X.; Kovalenko, M. V. Nanocrystals of Cesium Lead Halide Perovskites (CsPbX₃, X = Cl, Br, and I): Novel Optoelectronic Materials Showing Bright Emission with Wide Color Gamut. *Nano Lett.* **2015**, *15*, 3692.
 160. Isarov, M.; Tan, L. Z.; Bodnarchuk, M. I.; Kovalenko, M. V.; Rappe, A. M.; Lifshitz, E. Rashba Effect in a Single Colloidal CsPbBr₃ Perovskite Nanocrystal Detected by Magneto-Optical Measurements. *Nano Lett.* **2017**, *17*, 5020–5026.
 161. Galkowski, K.; Mitioglu, A.; Miyata, A.; Plochocka, P.; Portugall, O.; Eperon, G. E.; Wang, J. T. W.; Stergiopoulos, T.; Stranks, S. D.; Snaith, H. J.; Nicholas, R. Determination of the exciton binding energy and effective masses for methylammonium and formamidinium lead tri-halide perovskite semiconductors. *J. Energy Environ. Sci.* **2016**, *9*, 962–970.
 162. Kim, S.; Kim, J.-M.; Park, J.-E.; Nam, J.-M. Nonnoble-Metal-Based Plasmonic Nanomaterials: Recent Advances and Future Perspectives. *Adv. Mater.* **2018**, *30*, 1704528.
 163. Jain, P. K.; Lee, K. S.; El-Sayed, I. H.; El-Sayed, M. A. Calculated Absorption and Scattering Properties of Gold Nanoparticles of Different Size, Shape, and Composition: Applications in Biological Imaging and Biomedicine. *J. Phys. Chem. B* **2006**, *110*, 7238–7248.
 164. Christopher, P.; Xin, H.; Linic, S. Visible-light-enhanced catalytic oxidation reactions on plasmonic silver nanostructures. *Nature Chem.* **2011**, *3*, 467–472.
 165. Rycenga, M.; Cobley, C. M.; Zeng, J.; Li, W.; Moran, C. H.; Zhang, Q.; Qin, D.; Xia, Y. Controlling the Synthesis and Assembly of Silver Nanostructures for Plasmonic Applications. *Chem. Rev.* **2011**, *111*, 3669–3712.
 166. Wang, H.; Tam, F.; Grady, N. K.; Halas, N. J. Cu Nanoshells: Effects of Interband Transitions on the Nanoparticle Plasmon Resonance. *J. Phys. Chem. B* **2005**, *109*, 18218–18222.
 167. Sundararaman, R.; Narang, P.; Jermyn, A. S.; Goddard III, W. A.; Atwater, H. A. Theoretical Predictions for Hot-Carrier Generation from Surface Plasmon Decay. *Nat. Commun.* **2014**, *5*, 5788.
 168. Bernardi, M.; Mustafa, J.; Neaton, J. B.; Louie, S. G. Theory and Computation of Hot Carriers Generated by Surface Plasmon Polaritons in Noble Metals. *Nat. Commun.* **2015**, *6*, 7044.
 169. Fernandes, D. L. A.; Paun, C.; Pavliuk, M. V.; Fernandes, A. B.; Bastos, E. L.; Sa, J. Green Microfluidic Synthesis of Monodisperse Silver Nanoparticles via Genetic Algorithm Optimization. *RSC Adv.* **2016**, *6*, 95693–95697.

170. Takami, Y.; Furube, A.; Murai, M.; Hara, K.; Katoh, R.; Tachiya, M. Dynamics of efficient electron–hole separation in TiO₂ nanoparticles revealed by femto-second transient absorption spectroscopy under the weak-excitation condition. *Phys. Chem. Chem. Phys.* **2007**, *9*, 1453–1460.
171. Hattori, Y.; Abdellah, M.; Rocha, I.; Pavliuk, M.V.; Fernandes, D.L.A.; Sá, J. Light-Induced Ultrafast Proton-Coupled Electron Transfer Responsible for H₂ Evolution on Silver Plasmonics. *Mater. Today* **2018**, *21*, 590–593.
172. Kawai, J.; Nihei, Y. Charge Transfer Effects on the Chemical Shift and the Line Width of the CuK α X-Ray Fluorescence Spectra of Copper Oxides. *Solid State Commun.* **1989**, *70*, 567–571.
173. Hodak, J. H.; Martini, I.; Hartland, G.V. Spectroscopy and Dynamics of Nanometer-Sized Noble Metal Particles. *J. Phys. Chem. B* **1998**, *102*, 6958–6967.
174. Link, S.; El-Sayed, M. A. Spectral Properties and Relaxation Dynamics of Surface Plasmon Electronic Oscillations in Gold and Silver Nanodots and Nanorods. *J. Phys. Chem. B* **1999**, *103*, 8410–8426.
175. Hartland, G. V. Optical studies of dynamics in noble metal nanostructures. *Chem. Rev.* **2011**, *111*, 3858–3887.
176. Liu, J. G.; Zhang, H.; Link, S.; Nordlander, P. Relaxation of Plasmon-Induced Hot Carriers. *ACS Photonics* **2018**, *5*, 2584–2595.
177. Roberti, T. W.; Smith, B. A.; Zhang J. Z. Ultrafast electron dynamics at the liquid–metal interface: Femtosecond studies using surface plasmons in aqueous silver colloid. *J. Chem. Phys.* **1995**, *102*, 3860–3866.

Acta Universitatis Upsaliensis

*Digital Comprehensive Summaries of Uppsala Dissertations
from the Faculty of Science and Technology 1759*

Editor: The Dean of the Faculty of Science and Technology

A doctoral dissertation from the Faculty of Science and Technology, Uppsala University, is usually a summary of a number of papers. A few copies of the complete dissertation are kept at major Swedish research libraries, while the summary alone is distributed internationally through the series Digital Comprehensive Summaries of Uppsala Dissertations from the Faculty of Science and Technology. (Prior to January, 2005, the series was published under the title "Comprehensive Summaries of Uppsala Dissertations from the Faculty of Science and Technology".)



ACTA
UNIVERSITATIS
UPSALIENSIS
UPPSALA
2019

Distribution: publications.uu.se
urn:nbn:se:uu:diva-369930